Origins of the H, HeI, and $CaII$ Line Emission in Classical T Tauri Stars

John Kwan,[1] and William Fischer[2]

[1] *Dept. of Astronomy, University of Massachusetts, Amherst, MA 01003,*
kwan@nova.astro.umass.edu
[2] *Dept. of Physics and Astronomy, University of Toledo, Toledo, OH 43606,*
wfische@utnet.utoledo.edu

`kwan@nova.astro.umass.edu`

ABSTRACT

We perform local excitation calculations to obtain line opacities and emissivity ratios and compare them with observed properties of H, HeI, OI, $CaII$, and NaI lines to determine the requisite conditions of density, temperature, and photon ionization rate. We find that UV photoionization is the most probable excitation mechanism for generating the $HeI\lambda10830$ opacities that produce all the associated absorption features. We also calculate the specific line flux at an observed velocity of $v_{obs} = \pm150\ km\ s^{-1}$ for both radial wind and infall models. All the model results, together with observed correlations between absorption and emission features and between narrow and broad emission components, are used to deduce the origins of the strong H, HeI, and $CaII$ broad line emission. We conclude that the first two arise primarily in a radial outflow that is highly clumpy. The bulk of the wind volume is filled by gas at a density $\sim 10^9\ cm^{-3}$ and optically thick to $HeI\lambda10830$ and $H\alpha$, but optically thin to $HeI\lambda5876$, $Pa\gamma$, and the $CaII$ infrared triplet. The optically thick $HeI\lambda5876$ emission occur mostly in regions of density $\geq 10^{11}\ cm^{-3}$ and temperature $\geq 1.5 \times 10^4\ K$, while the optically thick $H\alpha$ and $Pa\gamma$ emission occur mostly in regions of density around $10^{11}\ cm^{-3}$ and temperature between 8750 and $1.25 \times 10^4\ K$. In producing the observed line fluxes at a given v_{obs} the covering factor of these emission clumps is sufficiently small to not incur significant absorption of the stellar and veiling continua in either HeI or H lines. The strong $CaII$ broad line emission likely arise in both the magnetospheric accretion flow and the disk boundary layer where the gases dissipate part of their rotational energies before infalling along

magnetic field lines. The needed density and temperature are $\sim 10^{12} \ cm^{-3}$ and $\leq 7500 \ K$ respectively.

Subject headings: line: formation — stars: formation — stars: pre-main-sequence

1. Introduction

Spectroscopic observations and analyses have been and will be an essential tool in discovering the intricate details in the formation of a classical T Tauri star, as the spectral lines carry information on the kinematics and physical conditions of the gases close to the star. Thus, red absorptions extending to velocities in excess of $100 \ km \ s^{-1}$ in Balmer lines and the NaI doublet (Appenzeller & Wolf 1977, Edwards et al. 1994) indicate active accretion. Blue absorptions are rare in optical lines, but are seen in Balmer lines, so there is also hint of outflows. In addition, the profiles of forbidden lines like $[OI]\lambda6300$ and $[SII]\lambda6731$ reveal the often presence of jet-like flows (Kwan & Tademaru 1988, Hirth, Mundt, & Solf 1994). Even though the forbidden line emission originate at densities much lower than expected values in the vicinity of the star, the high speed of the jet signals that the outflow likely starts from a deep potential well as either a stellar wind or an inner disk wind that is subsequently collimated. In that case ejection of matter is as inherent a characteristic as accretion of matter in the star formation process.

Ultimately the unravelling of the contributions to the line intensities and profiles from different kinematic flows and the derivation of quantitative measures like mass flow rates require modelling and analysis of the strong emission lines. Natta et al. (1988) first examined the excitation and ionization of hydrogen in a stellar wind and found that the hydrogen line fluxes calculated for the same mass loss rate can span a wide range owing to differences in the gas temperature and in the stellar Balmer continuum. Hartmann et al. (1990) modelled both line fluxes and profiles in a stellar wind which, driven by Alfven waves, is characterised by large turbulent velocities in the accelerating portion of the flow. While the calculated fluxes cover the observed range, the Balmer line profiles are clearly unlike observed ones in being highly asymmetric with the red side much stronger than the blue side. The weakness of the blue side occurs because while the bulk of the hydrogen emission arise from the inner, denser and highly turbulent region, the outer, less strongly excited expanding envelope blocks the blue emission to an observer. Mitskevich, Natta, & Grinin (1993) also modelled the $H\alpha$ profile by postulating a flow that accelerates to a peak velocity and then decelerates towards zero. This double-valued velocity structure will produce an anomaly between the red and blue emission of an optically thick line at intermediate velocities, as the blue(red) emission will then arise from the outer(inner) part of the surface of constant observed velocity (v_{obs}),

where the excitation temperature is lower(higher). Then, to account for the observed ranges in shape and depth of the apparent blue absorption, Mitskevich et al. (1993) advocated a clumpy flow for the flexibility in varying the degree of shielding between the outer and inner parts of the constant v_{obs} surface. They, however, adopted a parametric function for the dependence of the line excitation temperature on position, and it is not clear if the observed fluxes and profiles of several Balmer lines can be reproduced self-consistently.

The higher Balmer lines, as well as $Pa\beta$ and $Br\gamma$ occasionally show red absorptions (Edwards et al. 1994, Folha & Emerson 2001). The clear indication of an infalling flow by the broad red absorption, and the realization that the optical/UV continuum excess can arise from the impact footpoints on the star (Calvet & Gullbring 1998) likely contribute to motivating the studies of hydrogen emission in an accretion flow from the disk along a dipolar trajectory (Muzerolle, Calvet, & Hartmann 1998a, 2001, Kurosawa, Romanova, & Harries 2008). The model hydrogen line fluxes generally agree with observed values and the model line profiles are centrally peaked with small blue centroids. The much better comparison of these calculated profiles with observed ones, in conjunction with findings of strong magnetic field strengths (Johns-Krull 2007) and theoretical investigations that probe the initiation of the accretion flow and the associated angular momentum exchange between disk and star (König & Pudritz 2000, Mohanty & Shu 2008, Romanova et al. 2007) spurs the burst of activities on the current paradigm of magnetospheric accretion.

While magnetospheric accretion clearly occurs, the origin of the hydrogen emission in the accretion flow is not without question. On observational grounds the main issue is the narrow width of the model line profile (Folha & Emerson 2001, Kurosawa et al. 2008). Other issues concern the observed high blue wing velocities, stronger blue emission at the line wings, and the sometimes large blue centroids. These characteristics are used as arguments against the $HeI\lambda5876$ emission originating in the accretion flow (Beristain, Edwards, & Kwan 2001, hereafter BEK01), but are also present in observed hydrogen profiles (Folha & Emerson 2001). With the advance of infrared spectroscopy, it is natural to follow up the $HeI\lambda5876$ study by observing the $HeI\lambda10830$ line which, being the transition immediately below $HeI\lambda5876$, will have a higher opacity and be more effective in absorbing the stellar and veiling continua. The ensuing $1\mu m$ spectroscopic survey of 38 CTTSs (Edwards et al. 2006, hereafter EFHK06) indeed produces additional information not conveyed by previously observed lines. It reveals that $HeI\lambda10830$ has the strongest propensity of showing absorption features, including broad blue absorptions indicative of radial outflows, sharp, narrow, blue absorptions indicative of disk winds (Kwan, Edwards, & Fischer 2007), red absorptions some of which are so broad and deep that challenge conventional assumptions of accretion flow structure (Fischer et al. 2008), and central absorptions.

The new $1\mu m$ observational results bring forth several new insights into the problem of helium and hydrogen line formation in CTTSs. First, the significant $HeI\lambda10830$ optical depth (~ 1 or higher) in several different kinematic flows, together with the high excitation energy (~ 20 eV) of its lower state, suggests that excitation via UV photoionization needs to be considered. Second, with the establishment of frequent presence of radial outflows, the issue regarding the comparatively rare occurrence of broad blue absorptions in Balmer lines now concerns the structures and physical conditions of those winds. Third, $HeI\lambda10830$ emission is common and comparable in strength to $Pa\gamma$ emission among the CTTSs with the strongest hydrogen lines (EFHK06). Origin of the helium emission in an accretion flow faces high hurdles because of the arguments put forth earlier with respect to the $HeI\lambda5876$ emission, and because the physical conditions needed for strong HeI emission (e.g., $T > 10^4$ K) may be taxing for a flow in which the gas is primarily in free fall. If the HeI emission originate in a radial wind, hydrogen emission from the wind may also be significant, as it is more easily produced, and needs to be re-examined.

We will attempt to address the above issues in this paper. Unlike earlier investigations which adopt a particular flow structure and evaluate how the model line fluxes and/or profiles fare with observations, we take a simpler but hopefully more general approach. We first calculate the atomic/ionic excitation at a local point and determine how the line opacites depend on the local physical conditions. We will use the observed relative opacities among the lines to shed light on the requisite physical conditions. The local excitation calculations also produce line emissivity ratios that can be compared with observed line flux ratios to further delimit the physical conditions. These local excitation results should be fairly independent of the flow structure. Then, to contrast between the outflow and infall velocity fields, we note that a major difference lies in the emission area contributing to the observed flux at a high $|v_{obs}|$ and calculate the specific fluxes of the more important lines at $|v_{obs}| = 150$ km s^{-1} for both a radial wind and an accretion flow.

Crucial to our endeavor is an observational data set that covers simultaneously both optical and $1\mu m$ spectral regions. $HeI\lambda10830$ is a key line because of its propensity in showing absorption features, thereby indicating presences of particular kinematic structures. Deriving strong constraints on the physical conditions giving rise to $HeI\lambda10830$ formation, however, needs another helium line, and $HeI\lambda5876$ is ideal both for its being a fairly strong line and its position as antecedent of $HeI\lambda10830$ in a radiative cascade. Such a data set of CTTSs, observed at optical and $1\mu m$ wavelengths simultaneously or nearly simultaneously has been procured by Edwards et al. (2010). Only a few of the objects are selected for use here to provide line ratios that are key to unravelling the origins of the line emission.

The outline of this paper is as follows. We describe the rationale and methodology of our

model calculations in the next section and give details of the atomic/ionic models employed in §3. We present in §4 the relevant observational information. In §§5, 6, 7 we present model results and compare them with observational data on line opacities, flux ratios, and specific fluxes respectively to delimit the requisite physical conditions. We summarize the findings thus deduced in those three sections and utilize them, together with other observational information, to decide on the locations of the H, HeI, and $CaII$ broad emission in §8. We discuss the implications of our proposed origins of the line emission in §9, and review the major conclusions in §10.

2. Line Excitation Model

The line emission from a gas depends on the local physical conditions and the radiative transfer. For three of the four kinematic structures revealed by the $HeI\lambda10830$ absorptions the high speed of each flow and the consequent large velocity gradients present isolate the radiative interaction to a region small in comparison with the overall size of the kinematic structure. Then if the physical conditions within that region are taken to be uniform, both the excitation of the gas and the consequent line emission depend only on local physical quantities, namely, density, kinetic temperature, and velocity gradient. The spontaneous emission, stimulated absorption and emission of photons in a line together produce an effective emission rate given by $A\beta$, with A being the spontaneous emission rate and β the escape probability given by $(1 - e^{-\tau})/\tau$, where the line optical depth

$$\tau = \frac{g_u}{g_l}\frac{A\lambda^3}{8\pi}(N_l - N_u\frac{g_l}{g_u})\frac{dl}{dv} \tag{1}$$

depends on the local population $N_l(N_u)$ of the lower(upper) level and the velocity gradient dv/dl (Sobolev 1960). The local emissivity of the line (erg s^{-1} cm^{-3}) is then $N_uA\beta h\nu$.

We take advantage of the above reduction of a global radiative transfer problem to a local one in generating model results for comparison with observational data. We will be primarily interested in the stellar wind and the accretion flow in our attempt to ascertain the origin of the broad line emission. We consider a point roughly in the middle of the flow, specifically at a distance r from the star where the flow speed $|v|$ reaches 150 km s^{-1}. The calculated line opacity at this position is taken to be representative, and the ordering in magnitude of the opacities of different lines will be compared with the observational ordering of the lines in propensity of showing an absorption to delimit the requisite physical conditions. The local ratio of emissivities of two lines will also be compared with the observed line flux ratio. This appears to be, at first sight, a gross approximation, since each line flux is an integration of the emissivity over the entire kinematic structure and clearly the density at

other parts of the flow, at least, is likely several times larger or smaller than the value at $|v| = 150 \ km \ s^{-1}$. However, the same local excitation calculation applies to all positions, only for different physical parameters, so when the value of an emissivity ratio is presented as a function of density and temperature, one can judge from the dependences how the results will be affected when averaged over a range of density and/or temperature. The local model calculation has the advantage of enabling us to explore a much broader parameter space, e.g. over four orders of magnitude in density span, as well as to include many more lines, both from a given atom by incorporating more energy levels and from different atoms. It will be seen later that a comparison of different emissivity ratios with observed line flux ratios does indicate clearly enough the necessary physical conditions for us to infer the source of the line emission, and that this deduction is not affected by the mentioned approximation.

For the stellar wind we assume radial streamlines from the star. The velocity gradient transverse to the radial direction is v/r. We expect the velocity gradient in the radial direction to be larger, for an acceleration of the gas sufficiently strong to enable the gas to escape. When the velocity gradient is not isotropic the escape probability is dependent on direction. We will not be concerned with this nuance, and simply assume an effective isotropic velocity gradient of $2v/r$. The error in this estimate is not significant since the velocity gradient enters only as a factor in the line opacity and is always multiplied with the density, which varies over a much broader range. We take $r = 4R_*$ to illustrate the stellar wind model.

We also assume radial streamlines toward the star for the accretion flow. At $|v| \geq 150 \ km \ s^{-1}$ the infall trajectory, even in the dipolar geometry, is approaching radial. The investigation of $HeI\lambda 10830$ red absorptions also finds that some red absorptions are so broad and strong that they are accounted for best by radial infall (Fischer et al. 2008). The same radial geometry also facilitates comparison of the model results between the two flows. A gas particle infalling onto a star of $0.5M_\odot$ and $2R_\odot$ will attain a speed of $150 \ km \ s^{-1}$ at 2.77 and $2.06R_*$ if it starts from 8 and $4R_*$ respectively, so we take r to be $2.5R_*$ for the accretion flow, and assume an effective isotropic velocity gradient of $2v/r$. The latter assumption can be quite wrong because, unlike the stellar wind, the accretion flow at high speeds fills only a very small solid angle, and the above work on red absorptions also finds that the infall streamlines may not uniformly fill the solid angle. In this case the velocity gradient is better given by $\delta v/\delta l$, where δv is the thermal/turbulence line width and δl the transverse size of an infall bundle. We have no grasp on δl and only note that $\delta v/\delta l$ may be closer to $2v/r$ even if δl is very different from r. As mentioned before, the velocity gradient enters into the opacity with the density, which is varied over a wide range, and emissivity ratios will be presented also as a function of line opacity, so the effect of a very different velocity gradient can still be gleaned from the results.

The difference between the assumed velocity gradients for the two flows is not large. It will also be seen that the model results depend much more strongly on density than the velocity gradient, so a change in the latter can be compensated by a much smaller change in the former. Thus the calculated dependences of the local line opacities and emissivity ratios on physical conditions are applicable to all flow structures with a comparable velocity gradient to within an order of magnitude.

The specific flux of a line, on the other hand, depends on the volume of emission, so it is sensitive to r, the actual flow geometry, and the velocity at which it is calculated. In particular, because the correlation of velocity with position is vastly different between the stellar wind and accretion flow, we expect their line fluxes to be quite different, even if line emissivity ratios are similar. It is with this consideration in mind that $|v| = 150\ km\ s^{-1}$ is specifically chosen. We think the line flux near this velocity or higher is a truer test of the accretion flow model than that near zero velocity, as it is much more constrained. Independent of the accretion flow geometry, the emission at high speeds must arise from distances quite close to the star. Then the focussing of the streamlines toward the star confines the solid angle of the accretion flow at high speeds, which is also constrained by the small area covering factor, typically ≤ 0.03 (Calvet & Gullbring 1998), of the shocks marking the accretion footpoints. Thus the emission volume of the gas at a high speed is well constrained, thereby making the corresponding line flux a more revealing diagnostic.

The observed line emission at $v_{obs} = v$ arise from locations at distances other than r because emission from positions with higher speeds than v also contribute when their projected velocities along the line of sight equal v_{obs}. To calculate it for the stellar wind we assume that from r to $1.5r$ the flow speed increases linearly from v to $2v$. When the line is optically thick the observed flux at v_{obs} depends on the excitation temperature and the projected area with an observed velocity of v_{obs}. In Figure 1 the right dashed curve shows, in the $x - z$ plane, the contour of $v_{obs} = -150\ km\ s^{-1}$ for a spherical wind. It can be seen that the projected area equals $\pi(1.5r\sin60^o)^2$ or $27(r/4R_*)^2\pi R_*^2$. When the line is optically thick the observed specific flux is then, in the simple case of a constant excitation temperature,

$$F_{v_{obs}} = \frac{2h\nu^4}{c^3}\frac{1}{e^{h\nu/kT_{ex}} - 1}\frac{27\pi R_*^2}{d^2}\ , \tag{2}$$

where T_{ex} is the excitation temperature between the upper and lower levels, and d is the distance to the star. When the line is optically thin, the observed flux is obtained from integrating the line emissivity over volume. If the latter varies with distance p from the star as p^{-a}, the observed specific flux is

$$F_{v_{obs}} = \frac{N_u A\beta h\nu}{4\pi d^2}\int_r^{1.5r} \left(\frac{r}{p}\right)^a \frac{4\pi p^2}{2v(\frac{2p}{r} - 1)}dp$$

$$= \frac{N_u A(1 - e^{-\tau}) h\nu r^3}{2d^2 \tau v} \int_1^{1.5} \frac{x^{2-a}}{2x - 1} dx \ . \tag{3}$$

Both N_u and τ are determined at r. For a between 0 and 4 the integral ranges from 0.53 to 0.25. Substituting the expression for τ given earlier in the denominator, the factor in front of the integral can be rewritten as

$$(1 - e^{-\tau})\frac{2h\nu^4}{c^3} \frac{1}{e^{h\nu/kT_{ex}} - 1} \frac{4\pi r^2}{d^2} \ . \tag{4}$$

In order that, when a line transits from optically thin to optically thick, the observed specific flux increases smoothly to the earlier limit for an optically thick line, we choose the integral to be 0.422 or an a of 1. The error in deriving the flux of an optically thin line is then about $\pm 40\%$. It turns out that, with the exception of $OI\lambda 8446$, the other lines studied are all optically thick under the physical conditions responsible for the observed line emission. The error in the specific flux of an optically thick line arises mostly from the assumption of a constant excitation temperature, but one can gauge from the presented results how a distribution of density or temperature affects $F_{v_{obs}}$.

For a spherical radial infall the calculation of the specific flux when a line is optically thin is analogous to the spherical wind case. It involves integration from R_* to r with an infall velocity distribution, and is also made to ensure a smooth transition between the optically thin and thick regimes. In the latter regime the specific flux depends on the projected area, and the contour of $v_{obs} = -150 \ km \ s^{-1}$ is shown by the left dashed curve in Figure 1. The corresponding projected area is $1.286\pi R_*^2$. This much smaller projected area at $|v_{obs}| = 150 \ km \ s^{-1}$ is a fundamental characteristic of any accretion flow model. The contrast against the stellar wind value is even larger when the small solid angle of the accretion flow near the star is taken into account. When the wind/infall is not spherical, the projected area depends on viewing angle, but we will not consider this nuance and simply obtain the observed line flux by multiplying the result for the spherical case by the filling factor of the flow in solid angle, F_Ω. For the stellar wind and accretion flow we adopt $F_\Omega = 0.5$ and 0.2 respectively, keeping in mind that the $HeI\lambda 10830$ line sometimes shows strong emission but only a highly displaced shallow blue absorption (Kwan et al. 2007), and that $F_\Omega = 0.2$ is needed to model the few very strong red absorptions (Fischer et al. 2008). Occultation of the line emission by the star and the disk is not taken into account. If it were, it can be seen from Figure 1 that in the infall case the line flux at $v_{obs} \leq -150 \ km \ s^{-1}$ would be severely curtailed.

Three physical parameters are important for the local excitation calculations. They are density, temperature, and ionization flux. The range of kinetic temperature, T, investigated is 0.5×10^4 to $3 \times 10^4 \ K$. We use the hydrogen nucleon number density, N_H, to indicate

the number density, and assume a solar composition of the gas. With the number density of $H : He : O : Ca : Na$ being in the ratio $1 : 0.0793 : 4.9 \times 10^{-4} : 2.2 \times 10^{-6} : 2 \times 10^{-6}$ (Lodders 2003), the total nucleon number density is then $1.08 N_H$ and the mass density is $\rho = 1.325 N_H m_H$, with m_H being the mass of the hydrogen atom. The range of N_H explored is 10^8 to 2×10^{12} cm^{-3}. For a laminar flow the mass flux is then given by $4\pi r^2 \rho v F_\Omega$ or $10^{-9}(N_H/10^9 \ cm^{-3})(r/4R_*)^2(v/150 \ km \ s^{-1})(F_\Omega/0.5) M_\odot \ yr^{-1}$.

We include photoionization as a means of excitation. As mentioned in §1 the high opacities of $HeI\lambda10830$ in the accretion flow, stellar wind, and disk wind suggest that photoionization of helium from its ground state is likely. As a rough estimate of this rate, we note that a luminosity of $10^{-4}L_\odot$ in photon energies above $24.6 \ eV$, situated at the star, will produce at $4R_*$ a HeI photoionization rate of

$$\gamma_{HeI} = 2 \times 10^{-2} (\frac{\alpha - 1}{\alpha + 2})(\frac{4R_*}{r})^2 \ \frac{L}{10^{-4}L_\odot} \ s^{-1} \ , \tag{5}$$

where $\alpha > 1$ is the power law index of the luminosity energy distribution. The greatest uncertainty in this rate, however, is the attenuation between the UV luminosity source and the local point considered, since the mean free path for an optical depth of unity at the ionization threshold is small, $\sim 1.3 \times 10^9$ cm for a HeI density of 10^8 cm^{-3}. To circumvent this problem we take γ_{HeI} as a parameter. The UV source will also ionize hydrogen from its ground state. The ratio γ_{HI}/γ_{HeI} ranges from 1.6 to 4 for α between 1.5 and 3 if the luminosity source is not attenuated. The attenuations at the two thresholds can differ a lot and it is not clear which one is stronger. In most of the calculations we simply adopt $\gamma_{HI} = 2\gamma_{HeI}$, but will comment on the effects of differential attenuation. The condition of $\tau_{HeI\lambda10830} \geq 1$ and $\tau_{Pa\gamma} \leq 1$, posed by the much more frequent occurrence of absorption features in $HeI\lambda10830$ than $Pa\gamma$, will require a minimum γ_{HeI} at temperatures low enough that collisional excitation of HeI is ineffective. It turns out that this limit is $\sim 10^{-5}$ s^{-1}, so we will present results for $\gamma_{HeI} = 10^{-4}$ and 10^{-5} s^{-1}. The latter are much smaller than the unattenuated value given in the above equation for the hypothetical 10^{-4} $L_\odot$ UV source.

The stellar and veiling continua, which peak at optical wavelengths, are effective in ionizing the excited states of hydrogen and helium, as well as the ground state and excited states of $CaII$ and NaI. We assume a CTTS of temperature $T_* = 4000$ K and radius $R_* = 2R_\odot$, and a veiling continuum given by a blackbody of temperature 8000 K covering 3% of the stellar surface area. At 5000Å the veiling continuum is then about as strong as the stellar continuum.

To summarize, the physical parameters in our local excitation model are primarily T, N_H, γ_{HeI}, and $2v/r$. The first three parameters are explored over broad enough ranges to cover all expected possibilities, such as line optical depths from 10^{-2} to 10^3, and emissivity

ratios from values smaller to values larger than corresponding observed line flux ratios. From these local excitation calculations line opacities and emissivity ratios are compared with observational data to delimit the requisite physical conditions. These results are fairly general and not strongly dependent on the kinematic structure. The line flux, on the other hand, is sensitive to the actual flow geometry. To illustrate the contrast between the stellar wind and the accretion flow, the line fluxes at $|v_{obs}| = 150 \ km \ s^{-1}$ are calculated for a stellar wind and an accretion flow reaching a speed of $v = |v_{obs}|$ at $r = 4R_*$ and $2.5R_*$ respectively. All these results aid in deciphering the observed line emission for their origin.

3. Atomic Models

CTTSs show many emission lines. The forbidden lines, such as $[OI]\lambda6300$, $[SII]\lambda6731$, are likely formed at more than ten stellar radii away and not germane to probing the accretion flow and inner structures of disk and stellar winds. Among the permitted lines, their profiles can be narrow ($FWHM \sim 20 \ km \ s^{-1}$), broad ($FWHM \sim 200 \ km \ s^{-1}$), or composite with a narrow component atop a broad component (BEK01). The narrow lines/components are most likely formed at the sites where accreting streamlines impact the star, so their fluxes convey information on the summed area of such regions and the cooling history of the shocked gas. Here we are concerned with the broad lines/components, as their widths indicate that they are likely formed as the gas accelerates either away from the star in a wind or towards the star in an accretion flow. In the optical and infrared domains these broad lines/components are, ordered roughly in decreasing emission strength, Balmer lines, $CaII \ H$, K, and infrared triplet, ($HeI\lambda10830$, Paschen and Brackett lines, $FeII$ lines), and ($HeI\lambda5876$, $NaI \ D$, $OI\lambda8446$, $HeI\lambda6678$, $OI\lambda7773$, FeI lines).

Several intrigues posed by the observed strengths of the above-mentioned lines indicate that an understanding of the CTTS spectra must involve examining the HI, HeI, and $CaII$ line excitations altogether. One puzzle is the relative strength between the $HeI\lambda10830$ and $Pa\gamma$ emission. The observed $HeI\lambda10830$ spectra(EFHK06), with prominent absorption features, clearly demonstrate the high $\lambda10830$ opacity, a consequence of the metastability of its lower state, $2s \ ^3S$. With $\tau_{HeI\lambda10830}$ at least as large as $\tau_{H\alpha}$, as inferred from their relative propensity in showing an absorption, a $HeI \ 2s \ ^3S$ level population comparable to or larger than the $HI \ n = 2$ level population is implied, and while $Pa\gamma$ competes against $Pf\alpha$, $Br\beta$, and $H\delta$ for the de-excitation of $n = 6$ $HeI\lambda10830$ is the sole permitted radiative decay channel for its upper level, $2p \ ^3P$. Then the $HeI \ 2s \ ^3S \rightarrow 2p \ ^3P$ collisional excitation rate is larger than the hydrogen $n = 2 \rightarrow 6$ collisional excitation rate. Thus collisional excitation should highly favor $HeI\lambda10830$ over $Pa\gamma$ emission, yet the two observed fluxes in emission

are almost the same.

The second puzzle is the very strong $CaII$ infrared triplet emission in those CTTSs with strong $HeI\lambda10830$ and $\lambda5876$ emission. The summed flux of the $CaII$ triplet rivals that of $H\alpha$. Collisional excitation of the triplet has the advantage that their upper state is only 3.1 eV above the ground state, so the triplet can be strong, relative to $H\alpha$, at low temperatures, despite the low Ca abundance. However $CaII$ has an ionization potential of 11.9 eV, much less than the HeI ionization potential of 24.6 eV. Furthermore, the lower state of the $CaII$ infrared triplet is metastable and only 1.7 eV above the ground state, so it is well populated.Ionization from this level takes 10.2 eV, very slightly less than the energy of the $Ly\alpha$ photon. A strong buildup of the $Ly\alpha$ intensity, through radiative trapping, is required to sustain population in levels $n \geq 2$ of hydrogen for strong Balmer, Paschen, and Brackett line emission. It will at the same time ionize $CaII$ from its metastable state and reduce the $CaII$ fraction. Thus the strong $CaII$ triplet emission appear incongruous with not only the $HeI\lambda10830$ and $\lambda5876$ emission but also the hydrogen Paschen and Brackett line emission. In addition, the infrared triplet are very optically thick, as their fluxes are nearly equal despite a factor of 10 difference among their oscillator strengths. Yet they rarely show any absorption feature, even in CTTSs where their peak fluxes are only comparable to the continuum flux.

In addition to calculating the HI, HeI, and $CaII$ line excitations, we will also include those of OI and NaI. The $OI\lambda11287$ and $\lambda8446$ lines are produced primarily through the $Ly\beta$ fluorescence process (Bowen 1947), in which the OI $3d\ ^3D$ state is excited upon absorption of a $Ly\beta$ photon by the ground state, and decays via emission of a $\lambda11287$, a $\lambda8446$, and a $\lambda1303$ photon in succession. Thus the $OI\lambda8446$ flux is expected to correlate with the $Pa\gamma$ flux. The $OI\lambda7773$ triplet, on the other hand, are formed via recombination and cascade and collisional excitation, in a fashion similar to the $CaII$ infrared triplet. So inclusion of the above OI lines will further check on the HI and $CaII$ excitation conditions. The NaI atom, with an ionization potential of 5.14 eV, is easily photoionized by the stellar and veiling continua, and requires a much lower temperature for collisional ionization than helium. The often appearance of absorption in the NaI doublet, in conjunction with absorption in $HeI\lambda10830$, then sheds light on the pertinent physical conditions.

We will not examine the $FeII$ and FeI lines here. There are many of them, from infrared to UV wavelengths. Their summed emission strength may even exceed that of the hydrogen lines, so they are an important heat sink, and must be counted in deriving the total energy generation rate. With ionization potentials of 7.9 and 16.2 eV for FeI and $FeII$ respectively, the FeI to $FeII$ flux ratio will also provide a constraint on the ionization condition. A proper study of the FeI and $FeII$ line excitations, however, needs

good observational data on the fluxes of the many UV multiplets, which are not presently available. The large number of lines and multiplets also makes it more suitable to study them in a separate paper. We will also not consider the lines of highly ionized metals, such as $CIV\lambda1549$ and $OVI\lambda1034$, partly because of the lack of simultaneous UV spectra and partly because understanding the excitations of these lines will likely benefit from understanding the HI, HeI and $CaII$ excitations first, rather than vice versa.

In the following subsections we describe our model atom/ion for HI, HeI, OI, $CaII$, and NaI, but leave the references for the atomic parameters to an appendix.

3.1. HI

In modelling the hydrogen atom we assume that the level population among degenerate energy states are thermally distributed, and use 15 distinct energy levels, labelled $n = 1-15$. Limiting the hydrogen atom to a fixed number of levels can be questionable. This is because the $n \rightarrow n + 1$ collisional rate coefficient, $C_{n,n+1}$, increases while the spontaneous emission rate of level n, A_n, decreases as n increases, so once the electron density N_e exceeds the value $A_n/C_{n,n+1}$, $\sim 5 \times 10^7~cm^{-3}$ for $n = 15$, or an even lesser value if some of the radiative transitions are optically thick, successive collisional excitations to higher levels, effectively leading to ionization, provide the quickest route of depopulating level n. Ignoring this population transfer to higher levels produces error in the population of not only level n, but also lower levels, since there is less population return to the lower levels from collisional and radiative de-excitations of upper levels. The proper number of levels to use is clearly dependent on N_e, which in turn is dependent on N_H, T, and γ_{HI}. To ensure that 15 levels are adequate over our explored density range, we have performed the following test. The net rate of population transfer from level 15 to 16 via collisions is given by $R_{15\rightarrow16} = (N_{15}N_eC_{15,16} - N_{16}N_eC_{16,15})$, where N_{15} and N_{16} are the population in level 15 and 16 respectively. The local excitation calculations with 15 levels show that the $n = 13 \rightarrow 14$ and $n = 14 \rightarrow 15$ excitation temperatures are higher than $6000~K$ for T between 7500 and $1.5 \times 10^4~K$, so, if the $n = 15 \rightarrow 16$ excitation temperature is $\geq 6000~K$, $R_{15\rightarrow16}$ has a top value of $\sim 0.01~N_{15}N_eC_{15,16}$, which is about one-half the direct collisional ionization rate, $N_eC_{15,\infty}$, from level 15. To estimate the effect of including this additional route of population transfer for level 15, we have artificially doubled $C_{15,\infty}$ and repeated the calculations. The differences in the hydrogen level population and line fluxes are less than a few percent between the two sets of calculations, and we are confident that the use of 15 levels is adequate to obtain reliable Paschen line fluxes up to the transition from $n = 13$ to 3.

3.2. HeI

Our HeI model atom consists of the 19 lowest energy states. The spin of the two electrons in each state can add up to 1 or 0, so the 19 states can be separated, according to the degeneracies of the total spin, into a ladder of triplets and one of singlets, since radiative transitions across the ladders are forbidden by the electric-dipole selection rules. For the same energy quantum number n the angular momentum states $l = 1 - n$, unlike those in the case of HI, are separated in energy by many thermal Doppler widths, so we treat them as distinct energy levels. Thus, our 19 level atom consists of 10 singlets with energy quantum number $n = 1 - 4$, and 9 triplets with energy quantum number $n = 2 - 4$. Figure 2 shows a schematic of the 11 $n = 1 - 3$ levels, and indicates several important transitions.

The lower level of the $\lambda 10830$ transition is highly metastable. Its radiative decay rate is only 1.7×10^{-4} s^{-1}. For our explored density and temperature ranges, collisions with electrons provide the speediest way of returning population to the ground state. A more important route than direct collisional de-excitation is collisional excitation to the singlet $2s\,^1S$, followed by another collisional excitation to $2p\,^1P$ and then emission of a $\lambda 584$ photon, which can either escape or photoionize hydrogen. The latter means of depleting $\lambda 584$ photons is particularly important once $\tau_{HeI\lambda 584}$ becomes large. To determine its rate of depopulating $2p\,^1P$, we note that the mean free path for hydrogen ionization is $l_{Hiz} = 1/(N_{HI}\sigma_{584A})$, where σ_{584A} is the photoionization cross-section at 584Å, while the absorption mean free path, averaged over a thermally broadened profile, is

$$l_{abs} \approx \frac{8\pi\Delta v_D[ln(\tau_{HeI\lambda 584} + 2.72)]^{0.5}}{B_{lu}hcN_{HeI}} \ , \tag{6}$$

where $\Delta v_D = (2kT/m_{He})^{0.5}$ is the helium thermal Doppler velocity width, and B_{lu} is the Einstein stimulated absorption coefficient. The rate (s^{-1}) of depopulating $2p\,^1P$ due to $\lambda 584$ ionizing hydrogen is then given by the product of the spontaneous emission rate, $A_{HeI\lambda 584}$, and the ratio l_{abs}/l_{Hiz}. As an illustration, in the case when hydrogen and helium are mainly neutral, this rate is about $2 \times 10^{-3} A_{HeI\lambda 584}$, but almost $2A_{HeI\lambda 20581}$. This process is important in determining not only the population in excited singlets, but also, through the reduced population flow from singlets to triplets via collisions, the triplet population.

The ionization of hydrogen by $\lambda 584$ photons also affects the hydrogen ionization structure, but only slightly. If helium excitation is produced primarily by UV continuum photoionization, the production rate $(s^{-1}\ cm^{-3})$ of $\lambda 584$ photons must be less than the rate of continuum photoionization or $N_{HeI}\gamma_{HeI}$. The rate of hydrogen ionization by $\lambda 584$ photons is then less than $N_{HeI}\gamma_{HeI} = 0.079N_H\gamma_{HeI}$, which is less than the rate of continuum photoionization of hydrogen, $N_{HI}\gamma_{HI}$. If thermal motion is the energy source for helium excitation, then collisional excitation and ionization are much more efficient for hydrogen than

for helium. Therefore, we have not implemented this coupling between the two ionization structures, which would require an iterative procedure.

In analogy to $\lambda 584$ photons ionizing hydrogen, $Ly\alpha$ photons can ionize helium from its two metastable states, $2s\ ^3S$ and $2s\ ^1S$, which will have the bulk of the excited state population. This ionization rate (s^{-1}) is readily deduced from the earlier derivation. It equals $N_2 A_{Ly\alpha} l_{abs} \sigma_{1216A}$, where N_2 is the hydrogen population in $n = 2$, l_{abs} the analogous $Ly\alpha$ absorption mean free path, and σ_{1216A} the $2s\ ^3S$ or $2s\ ^1S$ photoionization cross-section at 1216Å. We have included this process in addition to the usual photoionizations by the stellar and veiling continua. The corollary effect of depopulating the hydrogen $n = 2$ level is insignificant, as we have verified from the results of the calculations.

3.3.   OI

Figure 3 shows a schematic of the energy levels of OI pertinent to our calculations and the important radiative transitions. The ground state $2p^4\ ^3P$ has three fine-structure levels, with energy separations such that the forbidden transitions $^3P_1 \to^3 P_2$ and $^3P_0 \to^3 P_1$ have wavelengths of 63 μm and 146 μm respectively. The upper state $3d\ ^3D$ likewise has three fine-structure levels, but with much smaller energy separations. The $2p^4\ ^3P_2$ transitions to $3d\ ^3D_1$, $^3D_2$, and $^3D_3$ have wavelengths almost the same as $Ly\beta$, to within a hydrogen thermal Doppler width. With charge exchanges maintaining OI/OII close to HI/HII, absorption of $Ly\beta$ photons is a fortuitous enhancement of $3d\ ^3D$ excitation, thereby leading to strong $\lambda 11287$ and $\lambda 8446$ emission.

The $\lambda 11287$ photon emissivity $(cm^{-3}\ s^{-1})$ resulting from this $Ly\beta$ fluorescence process (Bowen 1947) depends on the $Ly\beta$ intensity and the probability that $3d\ ^3D$ decays via emission of a $\lambda 11287$ photon. Because $Ly\beta$ is expected to be very optically thick, we assume its specific intensity to be given by the blackbody value at the hydrogen $n = 1 \to 3$ excitation temperature, i. e., $I_{Ly\beta} = (2h\nu_{Ly\beta}^3/c^2)(9N_1/N_3 - 1)^{-1}$, where N_3 and N_1 are the hydrogen $n = 3$ and 1 level population respectively. For the probability of $\lambda 11287$ emission, we consider first the upper level $3d\ ^3D_1$. It can decay to all three fine-structure levels of the ground state as well as to $3p\ ^3P$, so the probability of $\lambda 11287$ emission upon absorption of a $Ly\beta$ photon through the $2p^4\ ^3P_2 \to 3d\ ^3D_1$ transition is

$$P = \frac{A_{\lambda 11287}\beta_{\lambda 11287}}{A_{\lambda 11287}\beta_{\lambda 11287} + A_{^3D_1 \to ^3P_0}\beta_{^3D_1 \to ^3P_0} + A_{^3D_1 \to ^3P_1}\beta_{^3D_1 \to ^3P_1} + A_{^3D_1 \to ^3P_2}} \ , \qquad (7)$$

where A signifies the spontaneous emission rate and β the escape probability. The $^3D_1 \to^3 P_2$ escape probability equals 1, even though the transition is most likely very optically thick,

because the $Ly\beta$ opacity is even larger, so the emitted $\lambda1025.77$ photon will not be absorbed by OI. The probabilities of $\lambda11287$ emission via $Ly\beta$ absorptions through the ${}^3P_2 \to^3 D_2$ and ${}^3P_2 \to^3 D_3$ transitions can be written out analogously. The most common situation is that $\lambda11287$ is optically thin and all the $2p^4 \,{}^3P \to 3d \,{}^3D$ transitions are sufficiently optically thick that $3d \,{}^3D$ decays to the ground state via emission of $\lambda1026$ photons that are absorbed by hydrogen. In this case the above expression reduces to $P = A_{\lambda11287}/(A_{\lambda11287} + A_{{}^3D_1\to^3P_2})$, and the $\lambda11287$ photon emissivity ($s^{-1}\ cm^{-3}$) via $Ly\beta$ pumping is simply

$$
\begin{aligned}
R_{Ly\beta} &= \frac{5}{9}N_{OI}\frac{N_3}{9N_1 - N_3}2.077A_{\lambda11287} \\
&= 1.41 \times 10^6\ N_{OI}\frac{N_3}{N_1}\ ,
\end{aligned}
\tag{8}
$$

with the approximation that $5/9$ of the OI population is in the $2p^4 \,{}^3P_2$ level. Even if N_3/N_1 is as low as 10^{-9}, $R_{Ly\beta}$ is still larger than what can be brought about through UV continuum photoionization or direct collisional excitation at $T \leq 10^4\ K$.

The absorption of $Ly\beta$ photons by OI has the corollary effect of depopulating the $HI\ n = 3$ population. We have included this process in the hydrogen excitation calculations, but only with the simple expression enumerated above for the most common situation in order to avoid an iterative procedure involving HI and OI calculations. With $N_{OI}/N_1 = 4.9\times10^{-4}$ it is readily seen from the above expression for $R_{Ly\beta}$ that the corresponding $n = 3$ de-excitation rate is $690\ s^{-1}$. While it can rival $Ly\beta$ escape, it is much weaker than $H\alpha$ escape at low densities and collisional de-excitation at high densities, so the actual effect on the hydrogen level population is insignificant.

The $Ly\beta$ fluorescence process enhances not only $\lambda11287$ emission but, through the subsequent radiative cascade back to the ground state, also $\lambda8446$ and $\lambda1303$ emission. The resulting $\lambda11287/\lambda8446$ flux ratio is then just the ratio of the photon energies or 0.75. However, collisional excitation favors $\lambda8446$ over $\lambda11287$ emission, so a smaller observed flux ratio is a measure of the relative contribution between the two processes. Absorption in $\lambda8446$ is occasionally seen. It is facilitated by the population built up in $3s \,{}^3S$ through $Ly\beta$ fluorescence and sustained via radiative trapping of $\lambda1303$ photons.

The $\lambda\lambda7772, 7774, 7775$ triplet emission is produced from recombination and cascade, and collisional excitation. The metastable nature of the lower level $3s \,{}^5S$, whose spontaneous emission rate is only $5 \times 10^3\ s^{-1}$, sustains a comparatively large population in that level and enhances the collisional pathway of triplet emission. It likewise helps to bring about absorption of the stellar and veiling continua through the larger line opacity.

In performing the OI excitation calculations we assume that the fine-structure states are populated in proportion to their degeneracies, and use a single level to represent them.

This simplification is appropriate when the transitions between those fine-structure states and another level are separated in energy by about one thermal Doppler width or less. When this is not the case, as for the $3s\ ^3S \rightarrow 2p^4\ ^3P$ or $3p\ ^5P \rightarrow 3s\ ^5S$ transitions, the simplified procedure works fine when the transitions are optically thin but, when they are optically thick, does not take into account the availability of several radiative channels for de-excitation. Also, when collisional de-excitation dominates over radiative de-excitation, it underestimates the total emitted flux by a factor equal to the number of distinct (Doppler-width separated) lines. To remedy this situation, we re-define the line optical depth as the usual definition divided by the above factor. It represents a sort of average of the optical depths of the separate lines. For example, in our procedure this optical depth between $2p^4\ ^3P$ and $3s\ ^3S$, $\tau_{\lambda1303}$, equals 0.6, 1.0, and 3.0 of $\tau_{\lambda1302.2}$, $\tau_{\lambda1304.9}$, and $\tau_{\lambda1306}$ respectively. This modification also produces the correct total emitted flux when the distinct lines are all optically thin and when they all have optical depths greater than ~ 2. There may be a small error in the level population when some of the line optical depths lie between 0.5 and 2, but this regime occupies a very narrow strip of our explored density range, and we are not overly concerned.

3.4.   CaII, NaI

$CaII$, with an ionization potential of 11.87 eV, can be ionized quite readily by even the veiling continuum if the latter has an energy distribution that extends towards the far UV like a blackbody. For example, with our adopted veiling continuum of temperature 8000 K and area covering factor of 0.03, the photoionization rate of the $4s\ ^2S$ ground state at $4R_*$ is $3.3 \times 10^{-4}\ s^{-1}$, higher than our assumed UV continuum photoionization rate, which is $\gamma_{CaII} \sim (0.5/6.3)\gamma_{HI}$. Moreover, the excited state $3d\ ^2D$, the lower state of the $\lambda\lambda8498, 8542, 8662$ triplet, is metastable, with an Einstein A rate of only 1 s^{-1}, so it is most likely populated in thermal equilibrium with the ground state. Its lower ionization potential and larger photoionization cross-section produce an even stronger ionization rate, $3.4 \times 10^{-2}\ s^{-1}$ with our adopted veiling continuum. As an example, if the $4s\ ^2S \rightarrow 3d\ ^2D$ excitation temperature is 7000 K, ionization of $CaII$ from $3d\ ^2D$ is 30 times that from $4s\ ^2S$. Also, as noted in the beginning of §3, the $3d\ ^2D$ ionization potential is very slightly less than the $Ly\alpha$ photon energy. This ionization rate by $Ly\alpha$ photons (s^{-1}) is (cf. §3.2)

$$\begin{aligned}
\gamma_{Ly\alpha} &= N_2 A_{Ly\alpha} l_{abs} \sigma_{3d\ ^2D} \\
&= 5.54 \times 10^4\ \frac{N_2}{N_1}(\frac{T}{10^4\ K})^{0.5}[ln(\tau_{Ly\alpha} + 2.72)]^{0.5}\ ,
\end{aligned} \tag{9}$$

where $\sigma_{3d\ ^2D} = 6.15 \times 10^{-18}\ cm^2$ is the $3d\ ^2D$ photoionization cross-section at threshold. In the excitation calculations the hydrogen $n = 2$ to 1 population ratio, N_2/N_1, has a value often larger than 2×10^{-7}, that needed for $\gamma_{Ly\alpha}$ to equal $3.4 \times 10^{-2}\ s^{-1}$, the $3d\ ^2D$ photoionization rate by the veiling continuum. Thus, $Ly\alpha$ photons constitute an even more potent source of $CaII$ ionization.

Our model $CaII$ atom consists of just the three levels $4s\ ^2S$, $3d\ ^2D$, and $4p\ ^2P$. Both $3d\ ^2D$ and $4p\ ^2P$ have two fine-structure states. The two $4p\ ^2P \to 4s\ ^2S$ transitions are the well known H and K lines at $\lambda\lambda 3968$ and 3934 respectively, while the three $4p\ ^2P \to 3d\ ^2D$ transitions constitute the infrared triplet. Like OI, we assume the fine-structure states to be populated in proportion to their degeneracies and re-define the line optical depth to reflect the number of distinct lines. The observed line fluxes indicate that all five lines are very optically thick, so our simplified procedure of lumping into one single level the population in all associated fine-structure states is fine.

Our model NaI atom consists of just the ground level $3s\ ^2S$ and an excited level comprising the two fine-structure states of $3p\ ^2P$, whose radiative decays give rise to the well known $\lambda\lambda 5896, 5890$ doublet. The lower state of the doublet being the ground state helps to bring about strong absorption and/or emission in the doublet. On the other hand NaI, with an ionization potential of only $5.14\ eV$, is easily photoionized or collisionally ionized from the ground level, and even more so from the excited level, so the sodium ionization structure is key.

4.   Observational Information

The local excitation calculations can produce line opacities and emissivities over an extensive parameter space of physical conditions, but need information from observational data to demarcate the pertinent regions. Here we summarize the observational input on line ratios, line specific fluxes, and line opacities that will be utilized to compare with model results.

For the information on hydrogen line ratios we make use directly of Bary et al.'s(2008) collection of $Pa\ n_u/Pa\beta$ and $Br\gamma/Pa\ n_u$ ratios, where n_u, from 5 to 14, is the energy quantum number of the upper level of the Paschen transition. For line ratios involving the $CaII$ infrared triplet and $OI\lambda\lambda 8446, 7773$ we utilize the data available in Muzerolle, Hartmann, & Calvet (1998b). Three objects (DL, DG, & BP Tau) are selected because they are the only ones whose $OI\lambda 7773$ is not dominated by a strong red absorption. Because the lines considered have quite close wavelengths, we simply use the listed equivalent widths to

obtain ratios among them. For the HeI lines we obtain the $HeI\lambda10830$ information from EFHK06 and the $HeI\lambda5876$ information from BEK01. To avoid the issue of estimating the true emission when an absorption feature is present in $HeI\lambda10830$, only those objects among the reference sample (cf. Fig. 4 of EFHK06) with emission much stronger than absorption are used. They (CW, DL, DG, HN, BP, GG, & DG Tau, and RW Aur), totalling 8, are then looked up in the reference sample of BEK01 for the $HeI\lambda5876$ data. The $HeI\lambda5876/\lambda10830$ ratio is equal to $(1 + r_R)EW_{\lambda5876}F_{\lambda5876}/[(1 + r_Y)EW_{\lambda10830}F_{\lambda10830}]$, where r_λ denotes the veiling, EW_λ the equivalent width and F_λ the photospheric specific flux, assumed to be given by that of a 4000 K blackbody. For $HeI\lambda5876$ the EW of the broad component is being used. In the same Echelle order of $HeI\lambda10830$ $Pa\gamma$ is observed, so the data set of EFHK06 conveniently provides the $Pa\gamma/HeI\lambda10830$ ratios for the same 8 objects. Unfortunately the $HeI\lambda\lambda10830, 5876$ data sets are procured at very different times, so the $HeI\lambda5876/\lambda10830$ ratios derived from them may have uncertainties associated with time variation of the line emission. Partly to remedy this situation, we will also utilize the preliminary information on three objects (DL, DG, & HN Tau) in the data set of Edwards et al. (2010). The $HeI\lambda5876/\lambda10830$ and $CaII\lambda8498/Pa\gamma$ ratios of those three objects are particularly helpful because the optical and $1\mu m$ spectra are procured at the same time.

For the observed specific fluxes of lines we make use of the $HeI\lambda10830$ and $Pa\gamma$ profiles in EFHK06, the $HeI\lambda5876$ profiles in BEK01, the $Pa\beta$ and $Br\gamma$ profiles in Folha & Emerson (2001), and the $CaII\lambda8542$ profiles in Muzerolle et al. (1998b). In the model calculations the specific flux of a line at $|v_{obs}| = 150~km~s^{-1}$ is measured relative to the continuum level that is given by a 4000 K photosphere of radius $2R_\odot$ veiled by a 8000 K blackbody over 3% of its surface. This is done to facilitate comparison with observed spectra which are usually plotted with velocity as abscissa and strength relative to the continuum as ordinate. Normally the veiling and photospheric temperature of the star are determined, so it is straightforward to take account of the differences in veiling and photospheric temperature between model and observed star. The remaining uncertainty lies in the unknown surface area of the stellar photosphere, which depends on both the stellar radius and, because of the presence of an opaque disk, the viewing angle.

The ratio of two emission lines conveys information on the line opacities in addition to the physical conditions of density and temperature, but usually detailed excitation calculations are needed to disentangle the effects of opacity, density, and temperature. An absorption feature, on the other hand, directly reveals that the line optical depth is ~ 1 or more, while an absence of a similar feature in another line indicates its optical depth is much smaller, except when its emission is sufficiently strong to fill in the absorption. Thus we can use the relative propensity among the observed lines in showing an absorption to constrain the physical conditions of the absorbing gas.

Clearly $HeI\lambda10830$ is most proficient in showing absorption features. EFHK06 find that 47% of 38 CTTSs observed show red absorptions at $HeI\lambda10830$ compared with 24% at $Pa\gamma$, and 71% show blue absorptions at $HeI\lambda10830$ compared with 0% at $Pa\gamma$. If the blue absorptions are separated into broad and narrow ones that are likely formed in a stellar wind and disk wind respectively (Kwan et al. 2007), then the two kinds are present in 39% and 29%, respectively, of the 38 objects. Among the 15 CTTSs observed by Edwards et al. (1994) red absorptions are seen in Na D and $H\delta$ in 9 and 8 objects respectively. The rarity of $H\alpha$ red absorptions (2/15) is due to the strong $H\alpha$ emission. Blue absorptions are present in $H\alpha$ and Na D for about 50% of the stars, but except for one star(As 353A), are narrow and sharp, indicative of a disk wind origin. Among the 8 $OI\lambda\lambda7773, 8446$ profiles shown in Muzerolle et al. (1998b) 2 have red absorptions in both lines, and another 4 have red absorptions in $OI\lambda7773$ only, while none has a blue absorption. Among the 11 $CaII\lambda8542$ profiles shown 1(DS Tau) has a red absorption, and 1 (RW Aur) has a narrow blue absorption. BEK01 shows 31 $HeI\lambda5876$ profiles, of which 3 have red absorptions and none has a blue absorption.

From the above observational input on absorption features we gather that a broad blue absorption indicative of a stellar wind is present quite often in $HeI\lambda10830$, only rarely in $H\alpha$ and Na D and thus far, not seen in the Paschen lines, $OI\lambda\lambda7773, 8446$, $HeI\lambda5876$, or the $CaII$ infrared triplet. In decreasing probability of showing a red absorption, the order of lines is roughly $HeI\lambda10830$, Balmer lines, Na D, $OI\lambda7773$, Paschen lines, $OI\lambda8446$, $HeI\lambda5876$, and $CaII$ infrared triplet. The rarity of red absorptions in the $CaII$ infrared triplet, however, does not indicate the lines are optically thin. They are known to be optically thick from their nearly equal emission strengths despite a factor of 5 between $\tau_{CaII\lambda8662}$ and $\tau_{CaII\lambda8498}$. Often their emission is very strong, as measured in relation to the continuum level, so it is likely the emission will fill in the red absorption produced from scattering the stellar and veiling continua. It also happens that Pa 13, Pa 15, and Pa 16 lie on the red side (at ~ 120 km s^{-1}) of $CaII\lambda\lambda8662, 8542$, and 8498 respectively, and their contribution will further obliterate a red absorption.

5. Line Opacities and Importance of UV Photoionization

5.1. Model Results

Figure 4 shows the optical depth contours of four important lines in the (N_H, T) plane for $r = 4R_*$, and $\gamma_{HeI} = 10^{-4}$(top panel) and 10^{-5} s^{-1}(bottom panel). They are $\tau_{H\alpha} = 1$ and 3.16, $\tau_{HeI\lambda10830} = 1$ and 3.16, $\tau_{Pa\gamma} = 0.1$ and 0.316, and $\tau_{HeI\lambda5876} = 0.1$ and 0.316, with the right contour of each pair having the higher value. The different contour levels

between ($H\alpha$, $HeI\lambda10830$) on the one hand and ($Pa\gamma$, $HeI\lambda5876$) on the other reflect their relative tendencies to show an absorption. They help to locate the appropriate region in (N_H, T) space causing absorption in one line but not in another. For example, to produce a discernible blue absorption in $HeI\lambda10830$ but not in $Pa\gamma$, the bulk of the gas need to have an N_H between the $\tau_{HeI\lambda10830} = 1$ and $\tau_{Pa\gamma} = 0.1$ contours. For $\gamma_{HeI} = 10^{-4}\ s^{-1}$ the leeway in N_H is a factor of between 10 and 50, depending on T.

The HeI and HI optical depth contours demonstrate the role of photoionization in HeI and HI excitation. Figure 4 shows that at T above $2.25 \times 10^4\ K(10^4\ K)$ the $HeI(HI)$ contours are almost identical between the two cases of γ_{HeI} (γ_{HI}). This occurs because for $\gamma_{HeI} = 10^{-4}\ s^{-1}$ ($\gamma_{HI} = 2 \times 10^{-4}\ s^{-1}$) and an N_e of $10^9\ cm^{-3}$ the rate of collisional excitations to the $HeI\lambda10830(H\alpha)$ lower level will equal the rate of population via photoionization at $T = 2.25 \times 10^4\ K(10^4\ K)$. Thus, above this temperature $HeI(HI)$ photoionization at the assumed strength is less effective than collisional excitation. The fairly large separation between the $\tau_{HeI\lambda10830} = 1$ and $\tau_{Pa\gamma} = 0.1$ contours in N_H space at $T > 2.25 \times 10^4\ K$ indicates that the condition of $\tau_{HeI\lambda10830} \gg \tau_{Pa\gamma}$ can be readily produced by collisional excitations alone. As the effectiveness of HeI collisional excitation declines with T decreasing towards $10^4\ K$, photoionization becomes increasingly more important and the locations of the $\tau_{HeI\lambda10830}$ contours depend on γ_{HeI}. Clearly a lower γ_{HeI} requires a higher N_H to produce the same line optical depth and, as seen in Figure 4, the $\tau_{HeI\lambda10830}$ contours for $\gamma_{HeI} = 10^{-5}\ s^{-1}$ shift to the right from those for $\gamma_{HeI} = 10^{-4}\ s^{-1}$. A comparison between the $\tau_{HeI\lambda10830} = 1$ and $\tau_{Pa\gamma} = 0.1$ contours will then delimit the (γ_{HeI}, N_H) parameter space available to meet the observational constraints. For example, at $9000\ K \le T \le 1.5 \times 10^4\ K$ a minimum γ_{HeI} of $\sim 10^{-4}\ s^{-1}$ is needed. At $T < 10^4\ K$ photoionization of HI becomes important and the $\tau_{H\alpha}$ and, more noticeably, $\tau_{Pa\gamma}$ contours also depend on γ_{HI}. It is interesting that in this temperature range comparing between the $\tau_{HeI\lambda10830} = 1$ and $\tau_{Pa\gamma} = 0.1$ contours in the $\gamma_{HeI} = 10^{-5}\ s^{-1}$ case shows that a larger (γ_{HeI}, N_H) parameter space is again available to meet the $\tau_{HeI\lambda10830} \gg \tau_{Pa\gamma}$ condition. Thus, at $T < 8750\ K$ a γ_{HeI} of $10^{-5}\ s^{-1}$ is more than sufficient.

The above rather surprising result is caused by the $HeI\lambda10830$ lower level being extremely metastable, making spontaneous decay ineffective in comparison with depopulation via collisions with electrons for $N_e > 10^4\ cm^{-3}$. As mentioned in §3.2, collisional excitation to the singlet $2s\ ^1S$ is more important than direct collisional deexcitation to the ground state. The rate of this depopulation route is then $\propto N_e e^{-9240\ K/T}$ and the $HeI\lambda10830$ optical depth, in the limit when photoionization dominates over collisional excitation, can be expressed as

$$\tau_{HeI\lambda10830} \propto \frac{N_{HeI}}{N_{He}} \frac{N_H}{N_e} \gamma_{HeI}\ e^{9240\ K/T}\ . \tag{10}$$

As T decreases, both N_{HeI}/N_{He} and $e^{9240\ K/T}$ increase while N_e/N_H decreases, and they work in concert to make $\tau_{HeI\lambda10830}$ larger, thereby enabling a given optical depth to be obtained at a lower N_H, hence the reversal of the $\tau_{HeI\lambda10830} = 1$ contour direction seen distinctly in the bottom panel of Figure 4.

An illustration of how the electron fraction N_e/N_H depends on the physical parameters will help understand the behaviors of the optical depth contours as well as results presented later. This fraction is contributed primarily by hydrogen ionization, but its dependences on T and N_H are not straightforward. In Figure 5 we plot N_e/N_H versus $log(N_H)$ for seven temperatures and $\gamma_{HI} = 2\gamma_{HeI} = 2 \times 10^{-4}$ (top panel) and $2 \times 10^{-5}\ s^{-1}$ (bottom panel). With the expectation that N_e/N_H is lower when γ_{HI} is lower, the dependences of N_e/N_H on N_H and T in the two panels are qualitatively the same. At $8750\ K \leq T \leq 10^4\ K$, N_e/N_H initially falls with N_H increasing from $10^8\ cm^{-3}$ as hydrogen ionization through UV photoionization dominates. It levels off and rises slowly when photoionization from $n = 2$, bolstered by N_2/N_1 increasing with increasing N_H and $Ly\alpha$ trapping, grows stronger, and rises faster once sufficient population is built up into the high n levels for collisional ionization to take over. At $T \leq 7500\ K$ the contributions from excited state ionizations only slow down the rate at which N_e/N_H decreases with increasing N_H.

The quantitative values of N_e/N_H make it easy to see the behavior of the $\tau_{HeI\lambda10830}$ contours. At $\gamma_{HeI} = 10^{-5}\ s^{-1}$ the $\tau_{HeI\lambda10830} = 1$ contour near $10^4\ K$ lies at $N_H \sim 10^{10}\ cm^{-3}$. From Figure 5(bottom panel) it is seen that there N_e/N_H decreases rapidly with T decreasing from 10^4 to $7500\ K$. This sharp decrease is largely responsible for the switchback of the $\tau_{HeI\lambda10830} = 1$ contour toward a lower N_H. The same figure also helps to explain the large separation between the $\tau_{HeI\lambda10830} = 1$ and 3.16 contours seen at $\gamma_{HeI} = 10^{-5}\ s^{-1}$ and $8750\ K \leq T \leq 10^4\ K$. This arises because in that temperature range increasing N_H above $\sim 10^{10}\ cm^{-3}$ leads to N_e/N_H increasing also, which counteracts the effect of N_{HeI}/N_{He} increasing in the expression for $\tau_{HeI\lambda10830}$. As a result $\tau_{HeI\lambda10830}$ barely changes for $3 \times 10^9\ cm^{-3} \leq N_H \leq 10^{12}\ cm^{-3}$. This large separation between the $\tau_{HeI\lambda10830} = 1$ and 3.16 contours is not seen in the $\gamma_{HeI} = 10^{-4}\ s^{-1}$ case because in the same temperature range the $\tau_{HeI\lambda10830} = 3.16$ contour there lies at $N_H < 10^9\ cm^{-3}$.

At $T \leq 7500\ K$ the $\tau_{HeI\lambda10830}$ contours for the two γ_{HeI}s are not far apart. This insensitivity of $\tau_{HeI\lambda10830}$ to decreasing γ_{HeI} at low temperatures may explain why $HeI\lambda10830$ shows such a penchant for absorption. Seen in $HeI\lambda10830$ are not only the broad blue and red absorptions that arise from kinematic regions close to the star, but also the narrow, sharp blue absorption indicative of a disk wind, and the central absorption that has been suggested as arising from a disk corona even farther away from the star (Kwan 1997). Presumably the ionization sources are located close to the star and, even if intervening attenuation is

ignored, γ_{HeI} will decrease with distance. It turns out that the density required to produce a $\tau_{HeI\lambda10830}$ of unity is not prohibitive. To see this, we find that if N_e is supplied through UV photoionization of hydrogen, as likely at $T < 7500\ K$, then $N_e \propto (N_H\gamma_{HI})^{0.5}$ and

$$\tau_{HeI\lambda10830} \propto (N_H\gamma_{HeI})^{0.5}(\frac{\gamma_{HeI}}{\gamma_{HI}})^{0.5}\ e^{9240\ K/T}\ . \tag{11}$$

Thus $\tau_{HeI\lambda10830}$ is more sensitive to T for $T \leq 7500\ K$ than to γ_{HeI}. Also γ_{HeI}/γ_{HI} can be quite large if the UV continuum near the hydrogen ionization threshold is attenuated more severely by intervening hydrogen. In the limit that both helium and hydrogen are ionized by photons with energies $\geq 24.6\ eV$ γ_{HeI}/γ_{HI} is ~ 6, which is a factor of 12 larger than the earlier assumed value of 0.5. This means that γ_{HeI} can be smaller than $10^{-5}\ s^{-1}$ by a factor of 12 and still produce at $T = 5000\ K$ a $\tau_{HeI\lambda10830}$ of one with $N_H = 5 \times 10^8\ cm^{-3}$. Even lower values of γ_{HeI} are possible if T is lower. The temperature at which direct collisional de-excitation of $2s\ ^3S$ occurs as rapidly as the postulated de-population route is $2700\ K$, so γ_{HeI} can be smaller by another factor of ~ 20 when direct collisional de-excitation dominates.

In Figure 4 the pair of contours for each line purports to illustrate its sensitivity to varying N_H. It is seen that the $H\alpha$, $Pa\gamma$, and $HeI\lambda5876$ optical depths increase faster than linearly with increasing N_H. This is because the population in each of their lower level is sustained via radiative trapping, so for $H\alpha$, for example, $\tau_{H\alpha} \propto N_2 \propto N_1(\gamma_{HI} + N_eC_{12})\tau_{Ly\alpha}/A_{Ly\alpha} \propto N_1^2(\gamma_{HI} + N_eC_{12})$. The $HeI\lambda10830$ optical depth, by comparison, is less responsive to increasing N_H, particularly at T between 8750 and $10^4\ K$ when $\gamma_{HeI} = 10^{-5}\ s^{-1}$, as discussed earlier.

The $H\alpha$ contours are dependent on γ_{HI} over its explored range only at $T < 10^4\ K$, as mentioned before, and then only weakly so. The $Pa\gamma$ contours are more sensitive because the $n = 3$ population relies on the $n = 2$ population being built up first. Above $10^4\ K$ the hydrogen contours move towards lower densities with increasing temperature, owing to the stronger collisional excitations from the ground level, but then reverse direction at $T \sim 1.5 \times 10^4\ K$. This reversal is caused by the increase in collisional ionizations which rapidly reduces the hydrogen neutral fraction.

Figure 6 shows the contours $\tau_{NaI\lambda5892} = 1$, $\tau_{CaII\lambda3945} = 1$, $\tau^*_{CaII\lambda8498} = 1$, $\tau_{OI\lambda8446} = 0.1$, and $\tau_{OI\lambda7773} = 0.1$. The $\tau_{Pa\gamma} = 0.1$ contour is also re-plotted for comparison. For the line optical depth that represents a multiplet with well separated components (in Doppler widths), it needs be mentioned that, with our single level stand-in, the plotted optical depth is a rough average of the individual component optical depths. To be specific,

$$(\tau_{NaI\lambda5890}, \tau_{NaI\lambda5896})/\tau_{NaI\lambda5892} = (1.33,\ 0.67)$$
$$(\tau_{CaII\lambda3934}, \tau_{CaII\lambda3968})/\tau_{CaII\lambda3945} = (1.33,\ 0.67)$$

$$\left(\tau_{CaII\lambda8498}, \tau_{CaII\lambda8542}, \tau_{CaII\lambda8662}\right)/\tau^*_{CaII\lambda8498} = (0.2, \ 1.8, \ 1.0)$$

$$\left(\tau_{OI\lambda7772}, \tau_{OI\lambda7774}, \tau_{OI\lambda7775}\right)/\tau_{OI\lambda7773} = (1.4, \ 1.0, \ 0.6) \ . \tag{12}$$

The wavelength used to denote the $CaII$ infrared triplet as a group is the same as that of one member because that particular member is used to produce observed line ratios for comparison with model results. A similar denotation is not adopted for the $OI\lambda7773$ triplet because its three members are separated by only $\sim 200 \ km \ s^{-1}$ and all are seen within one line profile, so their total flux is used.

It is seen that the $CaII$ and NaI optical depth contours exhibit little difference between the two UV ionization fluxes, as the $CaII$ and NaI fractions depend only indirectly on the postulated UV continuum through the resulting N_e that affects the recombination rate and, in the case of $CaII$, also through the hydrogen N_2/N_1 ratio that affects the $Ly\alpha$ photoionization rate. The $CaII$ and NaI contours also respond similarly to T increasing from 5000 K, owing to their common susceptibility to collisional ionization. The OI ionization structure is tied to hydrogen's via charge exchange, so the OI optical depth contours at $T \leq 10^4 \ K$ respond to varying γ_{HI} in much the same way as the hydrogen optical depth contours. Above $T = 10^4 \ K$ the $\tau_{OI\lambda7773}$ contour stays at nearly the same N_H while the $\tau_{OI\lambda8446}$ contour moves towards much higher densities. This is due to the lower state of $OI\lambda7773$ being metastable while that of $OI\lambda8446$ decaying rapidly with $\tau_{OI\lambda1303}$ decreasing with increasing temperature.

Both Figures 4 and 6 refer to local excitation calculations at $r = 4R_*$, a location appropriate for either a stellar wind or the farther portion of an accretion flow. Figure 7 shows similar optical depth contours for $\gamma_{HeI} = 10^{-4} \ s^{-1}$, and $r = 2.5R_*$ to evaluate the dependence on position. Comparing it with Figures 4 and 6(top panels) indicates that the differences are quite small. For fixed values of N_H and T, the HI, HeI, and OI optical depths are somewhat smaller at $r = 2.5R_*$ because of the factor r/v in the opacity expression, hence their contours are displaced towards higher densities, with the amounts dependent on the responses of the line optical depths to increasing N_H. For the NaI and $CaII$ optical depths, there is the additional effect of a stronger stellar and veiling continuum flux at $r = 2.5R_*$, which increases the photoionization rate and leads also to a displacement of their contours towards higher densities. From Figures 4, 6 and 7 we can infer that the line optical depths and, by analogy, line emissivity ratios, which will be discussed in the next section, are much more dependent on N_H, T, and γ_{HeI} than on r.

5.2. Comparison with Observations

With in mind the observed propensities of the various lines in showing an absorption, we are in a position to draw the following conclusions from the model results presented in this section.

1. UV photoionization is necessary to produce the broad red and blue absorptions seen in $HeI\lambda10830$ because both gases have a temperature $\sim 10^4$ K or less. The most direct argument comes from the observed red absorptions. They are seen in $HeI\lambda10830$ and $NaI\lambda5892$ frequently, and $Pa\gamma$ occasionally. For NaI absorption to be more prevalent than $Pa\gamma$ absorption the temperature needs to be less than 10^4 K, as a comparison between the $Pa\gamma$ and NaI optical depth contours indicates. Then for $HeI\lambda10830$ absorption to be as prevalent as NaI absorption at $T < 10^4$ K, UV continuum photoionization is paramount. In the next two sections one result drawn from the analyses will be that the gas producing the broad blue absorption has a temperature not higher than $\sim 10^4$ K, which is also the condition needed for a broad blue absorption to be present in $NaI\lambda5892$ but not $Pa\gamma$.

2. In the temperature range of $T < 10^4$ K we can compare the observed order of lines in their propensity of showing a red absorption to the order gleaned from the model results by judging the available volume in (N_H, T, γ_{HeI}) space where the line optical depth exceeds 0.1 as reflecting the propensity. The latter decreases roughly in the order of $HeI\lambda10830$, Balmer lines, $CaII\lambda3945$, $NaI\lambda5892$, Paschen lines, $CaII\lambda8498$, $OI\lambda8446$, $OI\lambda7773$, and $HeI\lambda5876$. It needs to be noted that the range in γ_{HeI} is specifically chosen to place $HeI\lambda10830$ close to the top of the order, so a $\gamma_{HeI} \sim 10^{-5}$ s^{-1} or higher is needed. With in mind the explanation given in §4 regarding the lack of red absorptions in $CaII\lambda8498$, this order is close to that observed except for the position of $OI\lambda7773$. This line, however, is a triplet and, with its members separated by only ~ 200 km s^{-1}, is more effective than a single line in producing an absorption because of its greater velocity coverage, and this interesting property of $OI\lambda7773$ more than compensates for its smaller optical depth in relation to $OI\lambda8446$. The occasional presence of red absorptions in $OI\lambda8446$ and $HeI\lambda5876$ also indicates a density $N_H \sim 10^{11}$ cm^{-3} or higher for the red absorption gas.

3. The density of the gas producing the broad blue absorption is much lower than that of the accretion flow. This is obvious if the two flows have similar temperatures over most of their volumes, since $Pa\beta$, $Pa\gamma$, and $OI\lambda\lambda8446, 7773$ show red absorptions but almost never blue absorptions. But even if that were not the case, the absence of $Pa\beta$ and $Pa\gamma$ blue absorptions would by themselves require, at $T > 10^4$ K, $N_H < 3 \times 10^9$ cm^{-3}. A rough estimate, based on Figures 4, 6, and 7, of the typical gas density occupying the bulk of the stellar wind and accretion flow is 10^9 and 10^{11} cm^{-3} respectively. The corresponding mass flux, however, can be quite similar, as the product of the factors r^2 and F_Ω is likely 30 to

100 times larger for the stellar wind.

4. When $\tau_{HeI\lambda10830}$ is ~ 1 the $H\alpha$ optical depth is close to or higher than 1 for $T \leq 2 \times 10^4$ K and $\gamma_{HeI} \sim 10^{-4}$ s^{-1} or less (cf. Fig. 4). Thus we expect $H\alpha$ to be as effective as $HeI\lambda10830$ in absorbing the stellar and veiling continua. The rarer occurrence of broad blue or red absorption in $H\alpha$ is attributed to the strength of the $H\alpha$ emission, which is considerably greater than the continuum level.

6.   Line Ratios and Different Sets of Physical Conditions

Line ratios are very good diagnostics of physical conditions because while the observed flux of a line depends on the local line emissivity and the volume of emission, the flux ratio of two lines bypasses to a large extent the effect of emission volume and probes directly the local physical conditions. Here we examine several pairs of line ratios that are particularly illuminating in this regard.

The first pair is $HeI\lambda5876/\lambda10830$ and $Pa\gamma/HeI\lambda10830$. The nature of $HeI\lambda10830$ being the only allowed radiative transition following the $\lambda5876$ transition means that emission of a $\lambda5876$ photon is usually followed by emission of a $\lambda10830$ photon, but not vice versa, while collisional excitation from $2s\ ^3S$ strongly favors $\lambda10830$ emission because of both the lower excitation energy and the larger collisional cross-section. The $HeI\lambda5876/\lambda10830$ ratio is then expected to be small at low densities. It will rise only when the $\lambda10830$ transition becomes sufficiently optically thick that at the same time collisional de-excitation becomes competitive with $\lambda10830$ escape, population is built up into $2p\ ^3P$ from where collisional excitation of $\lambda5876$ is more effective. It is therefore very sensitive to density and, with $\lambda\lambda10830, 5876$ being the strongest observed helium lines, clearly the most important diagnostic of physical conditions giving rise to helium emission. To find out how the hydrogen emission fare in the same conditions, we want to contrast $HeI\lambda5876/\lambda10830$ against a ratio involving a hydrogen line and a helium line. The $Pa\gamma/HeI\lambda10830$ ratio is the most logical choice since, as mentioned in §3, its observed value of close to unity appears incongruous with their perceived opacities. It also has the advantage of being quite easily and accurately measured because both lines occur in the same Echelle order.

It is possible and highly probable that hydrogen emission arise from more than one kinematic region, because the physical conditions conducive to strong hydrogen emission are likely to be more wide-ranging than those conducive to either strong helium or $CaII$ emission. Ratios involving only hydrogen lines are therefore useful to ascertain the relevant region in the $(N_H,\ T,\ \gamma_{HI})$ parameter space. We will examine first $Pa\gamma/Pa\beta$ and $Pa\gamma/H\alpha$

in tandem to see, for a given γ_{HI}, how they depend on N_H and T, and correlate with each other. The $Pa\gamma/Pa\beta$ ratio is interesting because there is a substantial amount of recent data pointing to a fairly uniform but somewhat surprising value (Bary et al. 2008), while $Pa\gamma/H\alpha$ involves both the strongest optical line observed and the line selected earlier to compare with $HeI\lambda10830$. These two ratios involve hydrogen levels up to $n = 6$. We will also compare $Pa\ n_u/Pa\beta$ with observed ratios for n_u up to 12 so the observed hydrogen emission from high n levels are also brought into play.

The next two pairs of ratios focus on the $CaII$ infrared triplet emission in relation to hydrogen and oxygen emission. We examine first $CaII\lambda8498/Pa\gamma$ and $OI\lambda8446/Pa\gamma$, and then $CaII\lambda8498/OI\lambda8446$ and $OI\lambda7773/\lambda8446$. The latter pair has the added bonus that the three wavelengths involved are in close proximity, so the observed ratios have less uncertainties.

In the following three subsections we study in order the above mentioned line ratios. In each subsection we present first the results of the model calculations and then compare them with observations to demarcate the prevailing physical conditions.

6.1. $HeI\lambda5876/\lambda10830$ and $Pa\gamma/HeI\lambda10830$

6.1.1. Model Results

Figure 8 shows how $HeI\lambda5876/\lambda10830$ and $Pa\gamma/HeI\lambda10830$ depend on N_H (top panel) or line optical depth (bottom panel) for $r = 4R_*$, $\gamma_{HeI} = 10^{-4}\ s^{-1}$, and various temperatures. In this and subsequent figures we use different line types to denote different temperatures. Each of six line types signifies the same temperature in all the relevant figures, but a seventh line type, dot-long dash, can signify a different temperature in a different figure in order to allow for more flexibility in the selection of appropriate temperatures to illustrate. Table 1 lists the designations between line types and temperatures, and serves as a reference. When a model track in a figure has space nearby its temperature (in unit of $10^4\ K$) is marked for ready identification.

The most important physical process influencing the $HeI\lambda5876/\lambda10830$ ratio is collisions with electrons. The summed rate of $2s\ ^3S \to 3d\ ^3D$ and $2s\ ^3S \to 4f\ ^3F$ collisions, which lead to $HeI\lambda5876$ emission, is much weaker than the summed rate of collisions from $2s\ ^3S$ that lead to $HeI\lambda10830$ emission. In the regime when level de-excitation is dominated by radiative decay, the $HeI\lambda5876/\lambda10830$ ratio resulting from collisional excitations ranges from 1.3×10^{-3} at $T = 5000\ K$ to 4×10^{-2} at $T = 2 \times 10^4\ K$. The ratio resulting from recombination and cascade is higher. When the cascade ends at $2s\ ^3S$ roughly two $\lambda10830$

photons are produced for each $\lambda5876$ photon. However, $2s\,^3S$ de-excites to the ground level primarily through collisions, and the ratio of $2s\,^3S \rightarrow triplets$ to $2s\,^3S \rightarrow singlets$ collisional rate gives the number of additional $\lambda10830$ photons emitted before each de-excitation of $2s\,^3S$. This number is 2.4, 7.1, and 12.2 at $T = 5000$, 10^4, and 2×10^4 K respectively. Thus, even if helium excitation were all caused by UV photoionization of the ground state, the $HeI\lambda5876/\lambda10830$ ratio would only be 0.27, 0.1, and 0.07 at $T = 5000$, 10^4, and 2×10^4 K respectively. A larger ratio can only be obtained in the regime when the $HeI\lambda10830$ optical depth is sufficiently high that collisional de-excitation begins to rival $\lambda10830$ escape and effectively retards the growth of the $HeI\lambda10830$ flux.

The detailed calculations bear out the above analysis. In Figure 8 results for $T \leq 2 \times 10^4$ K are shown because those for $T = 3 \times 10^4$ and 2×10^4 K are almost the same. At low densities $HeI\lambda5876/\lambda10830$ is very small because of the prominent contribution to the $HeI\lambda10830$ emissivity from stimulated absorption of the stellar and veiling continua. With increasing N_H $HeI\lambda5876/\lambda10830$ roughly levels off at a value determined by the relative contribution between collisional excitation and recombination and cascade to the line emissivity. Then, depending on T, $HeI\lambda5876/\lambda10830$ begins to rise sharply when $\tau_{HeI\lambda5876}$ exceeds between 1 and 10 while $\tau_{HeI\lambda10830}$ is between 30 and 350. The actual criterion for collisional quenching of $HeI\lambda10830$ emission is $N_e C_{2p\,^3P \rightarrow 2s\,^3S} \sim A_{HeI\lambda10830}\beta_{HeI\lambda10830}$, and it is seen from Figure 8 that the density N_H needed to meet this criterion drops from $\sim 10^{12}$ cm^{-3} at $T = 5000$ K to $\sim 3 \times 10^{10}$ cm^{-3} at $T = 2 \times 10^4$ K.

Turning to $Pa\gamma/HeI\lambda10830$, it is seen that its dependences on N_H and T are drastically different. At a given temperature $Pa\gamma/HeI\lambda10830$ peaks at a lower N_H than that marking the sharp rise of $HeI\lambda5876/\lambda10830$. Over the range of N_H explored, $Pa\gamma/HeI\lambda10830$ is strongest at T between 8750 and 10^4 K and weakest at $T \geq 2 \times 10^4$ K, while it is the exact opposite for $HeI\lambda5876/\lambda10830$. Thus these two ratios anti-correlate. This relationship is readily understood when examined with the temperature range separated into two regimes.

At $T \geq 10^4$ K the $HeI\lambda10830$ emissivity is clearly very sensitive to temperature since the $1s\,^1S \rightarrow 2s\,^3S$ collisional excitation rate, which supplements UV photoionization in populating $2s\,^3S$, and collisional excitation of $HeI\lambda10830$ from $2s\,^3S$ are both strongly dependent on temperature. The $HeI\lambda5876$ emissivity is even more responsive to increasing temperature because of both a higher excitation energy from $2s\,^3S$ and its reliance also on the build up of the $2s\,^3S$ population. Consequently the $HeI\lambda5876/\lambda10830$ ratio increases with increasing T from 10^4 to 2×10^4 K. It does not change much with T between 2×10^4 and 3×10^4 K because the reduction of N_{HeI}/N_{He} due to ionization begins to take effect. The $Pa\gamma$ emissivity also benefits from the higher collisional excitation rate when T increases from 10^4 K, but the concurrent decreases in N_{HI}/N_H (due to ionization) and $Ly\alpha$ opacity

retard the build up of population into the excited levels. A confirmation of this very different behavior of the excited state population between HI and HeI can be seen from Figure 4, since the $\tau_{HeI\lambda5876}$ and $\tau_{Pa\gamma}$ contours are essentially contours of the population in $HeI\ 2p\ ^3P$ (lower state of the $HeI\lambda5876$ transition), $N_{2p\ ^3P}$, and $HI\ n\ =\ 3$, N_3, respectively. As T increases above $10^4\ K$, the $N_{2p\ ^3P}$ contour shifts towards decreasing N_H, indicating an increasing $N_{2p\ ^3P}/N_H$ ratio at a fixed N_H, and then hardly shifts between $T = 2.25 \times 10^4$ and $3 \times 10^4\ K$, while the N_3 contour shifts very little between $T = 10^4$ and $1.5 \times 10^4\ K$, but then shifts towards increasing N_H with further increase in T. This contrasting behavior accounts for $Pa\gamma/HeI\lambda10830$ decreasing while $HeI\lambda5876/\lambda10830$ increases with T increasing above $10^4\ K$.

As T decreases from $10^4\ K$ the ionization of hydrogen begins to rely more on UV photoionization and the electron fraction N_e/N_H decreases with decreasing T (cf. Fig. 5). Both decreases in N_e/N_H and T reduce the $HeI\ 2s\ ^3S$ de-excitation rate, as alluded to earlier in §5.1, and the consequent higher $2s\ ^3S$ population counteract the decrease in the $2s\ ^3S \rightarrow 2p\ ^3P$ collisional excitation rate. As a result the $HeI\lambda10830$ emissivity does not decrease as rapidly with decreasing temperature as the $Pa\gamma$ emissivity, and $Pa\gamma/HeI\lambda10830$ drops.

At a given temperature $Pa\gamma/HeI\lambda10830$ rises rapidly as N_H increases from $10^9\ cm^{-3}$, peaks at an N_H between 10^{10} and $10^{11}\ cm^{-3}$, and then falls. The rapid rise is related to the high sensitivity to N_H of the hydrogen population build up into upper levels, relying on radiative trapping of successive $\Delta n = 1$ transitions. The rise to the peak corresponds to $\tau_{Pa\gamma}$ increasing from less than 1 to a value between 2 and 20. Further increase in $\tau_{Pa\gamma}$ reduces the photon escape probability and slows the growth of $Pa\gamma$ emissivity, leading to a falling $Pa\gamma/HeI\lambda10830$ ratio. Curbing of $Pa\gamma$ emissivity occurs before that of $HeI\lambda10830$ emissivity because $C_{6\rightarrow5} \sim 35 C_{HeI\ 2p\ ^3P\rightarrow2s\ ^3S}$.

The earlier discussion in §5.1 on how γ_{HeI} affects the HeI and HI optical depth contours also hints at the corresponding responses of the $HeI\lambda5876/\lambda10830$ and $Pa\gamma/HeI\lambda10830$ ratios, which are shown in Figure 9 for $\gamma_{HeI} = 10^{-5}\ s^{-1}$. As expected, $HeI\lambda5876/\lambda10830$ is affected little and then only at $T < 10^4\ K$, since both line emissivities, like the line optical depths, respond similarly to varying γ_{HeI}, while $Pa\gamma/HeI\lambda10830$ clearly peaks higher at $8750\ K \leq T \leq 1.25 \times 10^4\ K$, the temperature range over which the $HeI\ 2s\ ^3S$ population is most susceptible to γ_{HeI}. The basic contrast between the two ratios in their dependences on N_H and T, however, remains the same.

6.1.2. Comparison with Observations

The anti-correlation between $HeI\lambda5876/\lambda10830$ and $Pa\gamma/HeI\lambda10830$ is more conspicuous when the two ratios are plotted against each other, as shown in Figure 10. The logarithmic scale is used for greater clarity of the model tracks which will be bunched towards the x or y axis in a linear plot. $HeI\lambda5876/\lambda10830$ is clearly high when $Pa\gamma/HeI\lambda10830$ is low, and vice versa. Many of the observed values that are marked lie at positions very much off the tracks that model results produce as N_H increases at a fixed T. The track closest to them is generated at $T = 5000~K$, and it is more easily seen from Figure 8 that $HeI\lambda5876/\lambda10830$ is slightly higher than 0.2 over the range $5\times10^{10}~cm^{-3} \leq N_H \leq 10^{12}~cm^{-3}$ when $Pa\gamma/HeI\lambda10830$ drops from ~ 1.0 to 0.4. Several arguments, however, point to a temperature of the emitting gas much higher than $5000~K$. They are based on ratios of hydrogen lines and on line fluxes, and will be propounded when the pertinent results are presented. The remaining way to explain the observed ratios is for $HeI\lambda5876$ and $Pa\gamma$ emission to arise from two different locales, e. g., a region of $T = 2\times10^4~K$ for the former and one of $T = 10^4~K$ for the latter. The $HeI\lambda5876/\lambda10830$ and $Pa\gamma/HeI\lambda10830$ ratios in their respective locales are then actually higher than the observed ratios since both locales will produce $HeI\lambda10830$ emission efficiently. For example, Figure 8 shows that at $T = 2 \times 10^4~K$ $Pa\gamma/HeI\lambda10830$ is less than 0.125 for $N_H > 3 \times 10^{10}~cm^{-3}$, while at $T = 10^4~K$ $HeI\lambda5876/\lambda10830$ is less than 0.06 for $N_H < 3 \times 10^{11}~cm^{-3}$. Then, if the observed $HeI\lambda10830$ emission is contributed equally by each locale, to produce observed $HeI\lambda5876/\lambda10830$ and $Pa\gamma/\lambda10830$ ratios of 0.23 and 0.6 respectively, the $2 \times 10^4~K$ ($10^4~K$) locale will need to produce a $HeI\lambda5876/\lambda10830$ ($Pa\gamma/HeI\lambda10830$) ratio of 0.4 (1.08).

In a way the model results confirm the perceived enigma mentioned in §3 concerning $HeI\lambda10830$ and $Pa\gamma$. They demonstrate that a common set of physical conditions, a natural and reasonable premise implicit in formulating the enigma, cannot produce at the same time the $HeI\lambda10830$ and $Pa\gamma$ emission strengths and their relative opacities as suggested by their propensities in showing an absorption.

We draw the following conclusions concerning the observed strong $HeI\lambda\lambda5876, 10830$ and $Pa\gamma$ emission.

1. $HeI\lambda5876$ and $Pa\gamma$ emission do not arise from the same locale. In particular, the gas emitting $HeI\lambda5876$ has a temperature close to $2 \times 10^4~K$ while that emitting $Pa\gamma$ has a temperature close to $10^4~K$.

2. The gas producing the $HeI\lambda\lambda5876, 10830$ emission is very optically thick in those lines. Thus $\tau_{HeI\lambda5876}$ needs to exceed 30 for $HeI\lambda5876/\lambda10830$ to exceed 0.3 (cf. Figs. 8 & 9 left bottom panel). The gas producing the $HeI\lambda10830$ blue absorption, which needs to be

optically thin in $HeI\lambda5876$ to avoid a $HeI\lambda5876$ blue absorption, is then distinct from the gas producing the HeI emission. This does not exclude the emission to arise from a stellar wind. It only stipulates that the emitting regions fill a sufficiently small volume of the wind that their summed surface area with a particular projected v_{obs} subtends a small solid angle.

3. The gas producing the red absorption is not producing the $HeI\lambda5876$ emission. Even though $HeI\lambda5876$ shows a red absorption in a few CTTSs, indicating in those objects an optical thickness that fulfills one requirement for strong emission, the deduced temperature of less than 10^4 K for that gas (cf. §5.2) does not meet the temperature requirement.

6.2. $Pa\gamma/Pa\beta$, $Pa\gamma/H\alpha$, $Pa\ n_u/Pa\beta$, and $Br\gamma/Pa\ n_u$

6.2.1. Model Results

The hydrogen line ratios are expected to correlate with one another, owing to the ladder-like energy level structure and very similar de-excitation pathways for each excited level. Figure 11 shows how $Pa\gamma/Pa\beta$ and $Pa\gamma/H\alpha$ relate to N_H and T for $r = 4R_*$ and $\gamma_{HI} = 2\gamma_{HeI} = 2 \times 10^{-4}$ s^{-1}. We use the case of $T = 10^4$ K to illustrate the $Pa\gamma/H\alpha$ dependence on N_H. As N_H increases from 10^8 cm^{-3}, $Pa\gamma/H\alpha$ falls because of the strong contribution to the $H\alpha$ emissivity from stimulated absorption of the stellar and veiling continua. This contribution diminishes when $\tau_{H\alpha}$ begins to exceed unity beyond $N_H \sim 6 \times 10^8$ cm^{-3}, whereupon $Pa\gamma/H\alpha$ increases with increasing N_H. The initial rise from $N_H = 6.3 \times 10^8$ to 3×10^9 cm^{-3} is due to the continual contribution of $Pa\gamma$ stimulated absorption. At $N_H \sim 3 \times 10^9$ cm^{-3} collisional excitation of $H\alpha$ also becomes important, and population is rapidly built up into $n > 2$ levels. The steeper response of the $n = 6$ population to N_H increasing from 6.3×10^9 to 2.5×10^{10} cm^{-3} produces the rise of $Pa\gamma/H\alpha$ from ~ 0.025 to 0.06. The further rise of $Pa\gamma/H\alpha$ as N_H exceeds $\sim 6.3 \times 10^{10}$ cm^{-3} is caused by collisional de-excitation rivalling $H\alpha$ escape, effectively stunting $H\alpha$ emissivity growth. As seen from the accompanying plot with $\tau_{Pa\gamma}$ as the abscissa the important rise of $Pa\gamma/H\alpha$ from 0.025 begins at $\tau_{Pa\gamma} \sim 1$. The $Pa\gamma/Pa\beta$ ratio also increases from ~ 0.45 at about the same $\tau_{Pa\gamma}$. Once the lines involved are optically thick their emissivity ratios are solely functions of the excitation temperatures. Thus, at $N_H = 1.6 \times 10^{10}$, 10^{11}, 6.3×10^{11} cm^{-3}, when $\tau_{Pa\gamma} = 5.6$, 33.4, 210, the ($H\alpha$, $Pa\beta$, $Pa\gamma$) excitation temperatures are $(4710, 2570, 2350)$, $(5930, 3240, 3020)$, and $(6290, 3920, 3940)$ respectively, giving rise to $Pa\gamma/H\alpha$ and $Pa\gamma/Pa\beta$ ratios of $(0.05, 0.54)$, $(0.065, 0.77)$, and $(0.15, 1.14)$. Just like the case of $HeI\lambda5876/\lambda10830$, both $Pa\gamma/H\alpha$ and $Pa\gamma/Pa\beta$ can, by means of collisional excitation, rise significantly above values produced from recombination and cascade only when the upper transition ($Pa\gamma$ here) is optically thick, and higher ratios require higher opacities and consequently higher excitation

temperatures.

At a given N_H $Pa\gamma/Pa\beta$ is almost the same for $8750\ K \leq T \leq 3 \times 10^4\ K$, but much smaller for $T \leq 7500\ K$. As a function of $\tau_{Pa\gamma}$ the behavior of $Pa\gamma/Pa\beta$ at $T \leq 7500\ K$ is actually more similar to those at higher temperatures, only that the highest $\tau_{Pa\gamma}$ reached is much smaller. This stronger similarity is because, at the same $\tau_{Pa\gamma}$, the comparison between the rates of photon escape, $A_{Pa\gamma}/\tau_{Pa\gamma}$, and collisional de-excitation is almost independent of temperature.

The dependences of $Pa\gamma/Pa\beta$ and $Pa\gamma/H\alpha$ on N_H are only weakly sensitive to γ_{HI}. At $T \geq 10^4\ K$ there is no discernible difference between the cases of $\gamma_{HI} = 2 \times 10^{-5}$ and $2 \times 10^{-4}\ s^{-1}$. At $T = (7500, 5000)K$, $Pa\gamma/Pa\beta$ is lower by $(0 - 10, 0 - 25)\%$ and $Pa\gamma/H\alpha$ lower by $(0 - 30, 20 - 40)\%$ over the density range $3 \times 10^{10}\ cm^{-3} \leq N_H \leq 10^{12}\ cm^{-3}$ for $\gamma_{HI} = 2 \times 10^{-5}\ s^{-1}$.

6.2.2. Comparison with Observations

In Figure 12 $Pa\gamma/Pa\beta$ is plotted against $Pa\gamma/H\alpha$ for $\gamma_{HI} = 2 \times 10^{-4}\ s^{-1}$. As expected, $Pa\gamma/Pa\beta$ correlates with $Pa\gamma/H\alpha$. The figure shows that $Pa\gamma/Pa\beta$ and $Pa\gamma/H\alpha$ do not delineate temperature well since the model tracks for different temperatures between 5000 and $3 \times 10^4\ K$ run similarly. They, however, are sensitive to density. From Figure 11 it is seen that the dependence of $Pa\gamma/Pa\beta$ on N_H is strong and quite similar for $8750 \leq T \leq 3 \times 10^4\ K$, but changes rapidly as T decreases from $8750\ K$. For example, to obtain $Pa\gamma/Pa\beta > 0.7$ the density needed at $T \leq 7500\ K$ is higher than that needed at $T \geq 8750\ K$ by a factor ≥ 4.

The data sample of Bary et al. (2008), including observations of the same object at multiple epochs, has 73 values of $Pa\gamma/Pa\beta$ that cluster closely about 0.86 with an estimated variance of ± 0.11. Among case B models the best fit to $Pa\gamma/Pa\beta$ as well as $Pa\ n_u/Pa\beta$ for n_u up to 14 has $T = 1000\ K$ and $N_e = 10^{10}\ cm^{-3}$. While this best fit to 8 data points has a reduced χ^2 surpassing 99.9% confidence, there is a glaring discrepancy at $Pa\gamma/Pa\beta$ where the fit value is only 0.73, and none of the other models explored has a higher value.

To see how the other $Pa\ n_u/Pa\beta$ values from our calculations fare with the data, we show them in Figure 13 for five densities at each of four temperatures. In general, as N_H increases above $2.5 \times 10^{10}\ cm^{-3}$, $Pa\ n_u/Pa\beta$ ($6 \leq n_u \leq 12$) increases, with the higher n_u increasing more. Although there is no single N_H that produces an excellent match to data, the range in N_H generating $Pa\ n_u/Pa\beta$ ratios that bracket the data is quite small, of order less than a factor of 10. This range is almost the same for $T \geq 8750\ K$, being $5 \times 10^{10}\ cm^{-3} \leq$

$N_H \leq 2 \times 10^{11}$ cm^{-3}, while that for $T = 7500$ K is 2×10^{11} $cm^{-3} \leq N_H \leq 10^{12}$ cm^{-3}. Figure 14 shows an analogous plot for $Br\gamma/Pa$ n_u, and the comparison between model results and data is similar.

Bary et al. (2008) has also compared their data with line ratios calculated with a constant excitation temperature (LTE), but find that in neither the optically thick nor thin case is there an acceptable fit. Our calculations are more similar to this set of models, only with the level excitations and line optical depths calculated self-consistently for a given N_H and T. Thus the Pa n_u excitation temperatures are not the same and the lines are not all completely optically thick. For example, at $T = 10^4$ K and $N_H = 10^{11}$ cm^{-3}, the excitation temperatures and line optical depths of ($Pa\beta$, $Pa\gamma$, Pa 10, Pa 12) are (3240, 3020, 2910, 2940)K and (104, 33.4, 3.44, 1.78) respectively. The fair agreement between model results and observed values makes understanding the hydrogen emission as resulting from collisional excitation an attractive alternative to the proposal by Bary et al.(2008) of a recombining gas at $T = 1000$ K.

We draw the following conclusions from the comparison between model and observational results on the hydrogen line ratios.

1. $Pa\gamma$ is optically thick in the hydrogen emission region. Thus $\tau_{Pa\gamma}$ needs to exceed 20 for $Pa\gamma/Pa\beta$ to exceed 0.7 at $T \leq 10^4$ K (Fig. 11 left bottom panel). Even many of the higher order Paschen lines have optical depths exceeding unity.

2. The temperature in the hydrogen emission region is higher than 5000 K. At 5000 K $Pa\gamma/Pa\beta$ reaches a value of only 0.81 even at the highest N_H explored, 2.5×10^{12} cm^{-3}. The more limited and extreme range on N_H needed to produce $Pa\gamma/Pa\beta \geq 0.86$ at $T \leq 5000$ K is one argument. Another is the difficulty in matching the observed $Pa\gamma/HeI\lambda10830$ ratio. As seen from Figure 8, $Pa\gamma/HeI\lambda10830$ is only 0.38 at 1.6×10^{12} cm^{-3} and falls with increasing N_H. This match-up is better in the case of $\gamma_{HeI} = 10^{-5}$ s^{-1} (cf. Fig. 9), but then $Pa\gamma/Pa\beta$ is only 0.6 at $N_H = 1.6 \times 10^{12}$ cm^{-3}.

3. The density in the hydrogen emission region is centered around $N_H \sim 10^{11}$ cm^{-3} if 8750 $K \leq T \leq 3 \times 10^4$ K, and around $N_H \geq 5 \times 10^{11}$ cm^{-3} if $T \leq 7500$ K, in order to produce the observed Pa $n_u/Pa\beta$, $n_u \geq 6$, ratios.

6.3. $CaII\lambda8498/Pa\gamma$, $OI\lambda8446/Pa\gamma$, $CaII\lambda8498/OI\lambda8446$, and $OI\lambda7773/\lambda8446$

6.3.1. Model Results

We compare the $CaII$ infrared triplet to $Pa\gamma$ for its being a fairly strong hydrogen line not too far away in wavelength, and to $OI\lambda8446$ for its tie to the hydrogen excitation through $Ly\beta$ fluorescence and its close proximity in wavelength. Figure 15 shows the dependences of $CaII\lambda8498/Pa\gamma$ and $OI\lambda8446/Pa\gamma$ on N_H and $\tau_{Pa\gamma}$ for $r = 4R_*$, $\gamma_{HI} = 2 \times 10^{-4}$ s^{-1} and seven temperatures. Figure 16 is analogous, but with $CaII\lambda8498/OI\lambda8446$ versus N_H and $\tau^*_{CaII\lambda8498}$, and $OI\lambda7773/\lambda8446$ versus N_H and $\tau_{OI\lambda7773}$. Because of our single level representation of multiple fine-structure levels, we divide the emissivity from our model $CaII$ ion by three, thereby implicitly assuming that all three components of the triplet are optically thick, a reasonable assertion as all three components have nearly identical fluxes and profiles. Our model $\tau^*_{CaII\lambda8498}$ is five times the optical depth of the component with the weakest oscillator strength (cf. §5.1), so the $CaII$ infrared emission requires $\tau^*_{CaII\lambda8498}$ to exceed ten. Our $OI\lambda7773$ line also represents a triplet, but the whole emissivity is employed here since the observed flux also comprises contributions from all three components.

Figure 15 shows that $OI\lambda8446/Pa\gamma$ rises continually to beyond unity as N_H increases. This is largely because the much lower $OI\lambda8446$ optical depth (cf. Fig. 6) keeps $\lambda8446$ escape more effective than collisional de-excitation. The dependence of $OI\lambda8446/Pa\gamma$ on temperature depends slightly on N_H. At 2×10^{10} $cm^{-3} \leq N_H \leq 2\times10^{11}$ cm^{-3} $OI\lambda8446/Pa\gamma$ increases as T increases from 5000 K, peaks at $T \sim 8750$ K and then drops with further increase in T. This behavior can be seen from the dependences of the $OI\lambda8446$ emissivity, $\propto N_{OI}N_3/N_1$, and the $Pa\gamma$ emissivity, $\propto N_6 A_{Pa\gamma}\beta_{Pa\gamma} \propto N_6/N_3$, on the hydrogen level population. Thus $OI\lambda8446/Pa\gamma$ is $\propto (N_{OI}/N_1)(N_3^2/N_6)$. As T increases from 5000 K at a fixed N_H, N_3/N_6 always decreases, while N_3 first increases but then decreases when hydrogen becomes more ionized. The countering effects of N_3/N_6 and N_3 on $OI\lambda8446/Pa\gamma$ in the beginning of the temperature rise, and their concerted effects subsequently produce the mentioned behavior. At $N_H > 2 \times 10^{11}$ cm^{-3} the same behavior holds except that $OI\lambda8446/Pa\gamma$ increases again as T increases beyond 1.5×10^4 K. This occurs because, with the rapid decrease of the hydrogen neutral fraction, radiative recombination of OII becomes important and N_{OI}/N_1 increases from the constant value of $1.1N_O/N_H$ maintained by charge-exchange reactions.

The two ratios $CaII\lambda8498/Pa\gamma$ and $CaII\lambda8498/OI\lambda8446$ have very similar dependences on N_H and T, as to be expected. The requirement of $\tau^*_{CaII\lambda8498} > 10$ confines the pertinent densities to $N_H \geq 10^{11}$ cm^{-3} for $T \leq 8750$ K and even higher limits for $T > 8750$ K. Thus the large $CaII\lambda8498/Pa\gamma$ and $CaII\lambda8498/OI\lambda8446$ model values at

$N_H < 10^{10}$ cm^{-3} are not relevant. They actually involve very small fluxes, but are shown for uniformity in the density range covered. As N_H increases from $\sim 10^{11}$ cm^{-3} at a fixed temperature, both $CaII\lambda8498/Pa\gamma$ and $CaII\lambda8498/OI\lambda8446$ rise rapidly. Two factors contribute to this. First, while N_{HI}/N_H is fairly constant in that density range (cf. Fig. 5), the fraction of calcium in $CaII$ increases with N_H. Second, the onset of collisional de-excitation of the $CaII$ population occurs, by comparison with hydrogen, at a higher N_H. When the latter is reached, the consequent collisional quenching of the $CaII$ triplet emissivity causes the decline of the ratio from its peak.

Both $CaII\lambda8498/Pa\gamma$ and $CaII\lambda8498/OI\lambda8446$ reach their highest value at $T = 7500$ K. This can be understood as follows. The hydrogen line emissivities are fairly insensitive to temperature for 8750 $K \leq T \leq 3 \times 10^4$ K (cf. §6.2). The $CaII\lambda8498$ emissivity, on the other hand, decreases with increasing T above 8750 K, owing to the rapidly decreasing $CaII$ fraction. Thus the two ratios fall beyond $T = 8750$ K. At 5000 $K \leq T \leq 8750$ K collisional excitations of both $CaII$ and HI are sensitive functions of temperature because of the strong dependence of N_e/N_H on T (cf. Fig.5), and the higher ratio of excitation potential to thermal energy. Above $N_H = 10^{11}$ cm^{-3}, however, collisional de-excitation comes into play for hydrogen, and the $Pa\gamma$ emissivity increases only modestly with increasing temperature in comparison with the $CaII$ triplet emissivity which, until $N_H \geq 6 \times 10^{11}$ cm^{-3}, is still proportional to $(N_{CaII}/N_{Ca})(N_e/N_H)$, and the steeper rise of Ne/N_H with increasing T from 5000 K more than overcomes the counter effect of a lower N_{CaII}/N_{Ca} ratio. As a result, $CaII\lambda8498/Pa\gamma$ increases as T increases from 5000 K and, in conjunction with its fall at $T > 8750$ K, peaks at an intermediate temperature.

Regarding the $OI\lambda7773/\lambda8446$ ratio, both recombination and cascade and collisional excitation strongly favor $OI\lambda7773$ over $OI\lambda8446$ emission. This ratio is less than unity only because of the $Ly\beta$ fluorescence process which, as seen from Figure 16, is most effective at N_H between 10^{10} and 3×10^{10} cm^{-3}. At $N_H < 10^{10}$ cm^{-3}, even though $Ly\beta$ fluorescence remains more effective than the other two processes, $OI\lambda7773/\lambda8446$ increases as N_H decreases. This is because stimulated absorption of the stellar and veiling continua contributes prominently to the $OI\lambda7773$ emissivity. But the line fluxes involved are very small. $OI\lambda7773/\lambda8446$ also increases as N_H increases above $\sim 3 \times 10^{10}$ cm^{-3}. This is because collisional de-excitation begins to affect the hydrogen level population, causing N_3/N_1, the important factor in the $Ly\beta$ fluorescence rate, to be nearly constant, while collisional excitation of $OI\lambda7773$ continues to grow roughly as N_H^2. Thus, in this regime $OI\lambda7773/\lambda8446$ responds to increasing density in a fashion similar to $CaII\lambda8498/OI\lambda8446$, but it has not reached a peak even at $N_H = 1.6 \times 10^{12}$ cm^{-3} because collisional de-excitation of $OI\lambda7773$ remains weaker than $\lambda7773$ escape.

The dependences of the four emissivity ratios on γ_{HI} between 2×10^{-4} and 2×10^{-5} s^{-1} are not strong, with $CaII\lambda8498/Pa\gamma$ and $CaII\lambda8498/OI\lambda8446$ reaching somewhat higher values for $5000 \ K \leq T \leq 7500 \ K$ when $\gamma_{HI} = 2 \times 10^{-5}$ s^{-1}. There is also a weak dependence on r. Among the four cases of γ_{HI} and r, the ($\gamma_{HI} = 2 \times 10^{-4}$ s^{-1}, $r = 4R_*$) and ($\gamma_{HI} = 2 \times 10^{-5}$ s^{-1}, $r = 2.5R_*$) cases show the largest difference.

6.3.2. Comparison with Observations

Figure 17 shows the relations between $CaII\lambda8498/Pa\gamma$ and $OI\lambda8446/Pa\gamma$ and between $CaII\lambda8498/OI\lambda8446$ and $OI\lambda7773/\lambda8446$ for the case ($\gamma_{HI} = 2 \times 10^{-4}$ s^{-1}, $r = 4R_*$), and Figure 18 shows those for the case ($\gamma_{HI} = 2 \times 10^{-5}$ s^{-1}, $r = 2.5R_*$). In addition to the data points marked, we mention that $CaII\lambda8498/OI\lambda8446$ can be determined for the remaining 5 objects in the data set of Muzerolle et al.(1998b). It is 4.5, 12.7, 9.8, 0.81, and 1.31 for DR, CW, RW, DS, and UY Tau respectively. Thus it appears that the observed values of $CaII\lambda8498/OI\lambda8446$ separate into two groups. The full data set of Edwards et al.(2010) also indicates this dichotomy, namely, one group with $CaII\lambda8498/Pa\gamma$ or $CaII\lambda8498/OI\lambda8446$ close to or less than 1, the other with $CaII\lambda8498/Pa\gamma$ or $CaII\lambda8498/OI\lambda8446$ greater than ~ 5. The physical conditions that will produce the first group of values are N_H around 10^{11} cm^{-3} and T between 5000 and 1.25×10^4 K (cf. Figs. 15 & 16), but the temperature is narrowed to $8750 \ K \leq T \leq 1.25 \times 10^4 \ K$ when the constraints imposed by the observed $Pa \ n_u/Pa\beta$ ratios are also implemented (cf. §6.2.2). To produce the second group of values a considerably higher N_H, $\sim 10^{12}$ cm^{-3}, is required, while T is restricted to $\leq 7500 \ K$.

The CTTSs with $CaII\lambda8498$ emission much stronger than $Pa\gamma$ or $OI\lambda8446$ emission also tend to be the ones with the most prominent $HeI\lambda5876$ emission. The physical conditions needed to produce the $CaII\lambda8498/Pa\gamma$ ratio cannot produce the $HeI\lambda5876/\lambda10830$ ratio, so a separate region producing the bulk of the $HeI\lambda5876$ emission is additionally required, as already inferred in §6.1. The $CaII$ emission region itself appears to be capable of generating the observed ratios among the hydrogen lines (cf. Figs 13 & 14 $T = 7500 \ K$ panel).

The CTTSs with $CaII\lambda8498$ emission comparable to or less than $Pa\gamma$ emission have a broad spread in helium emission, from $HeI\lambda5876/\lambda10830$ ratios close to those of the previous group to little $HeI\lambda5876$ emission and $HeI\lambda10830$ primarily in absorption (Edwards et al. 2010). When $HeI\lambda5876$ emission is weak, the physical conditions needed to produce the hydrogen line ratios(cf. §6.2) can also generate the requisite $CaII$ emission. When $HeI\lambda5876$ emission is strong, a separate region producing it is again called upon.

Based on the above understanding of the ratios involving HeI, H, and $CaII$ lines, we draw the following deduction.

1. Three sets of physical conditions are identified. The first, characterized by a comparatively high temperature (T close to 2×10^4 K) is necessary to produce strong $HeI\lambda5876$ emission. The second, characterized by a comparatively high density ($N_H \sim 10^{12}$ cm^{-3}) and low temperature ($T \leq 7500$ K), is necessary to produce strong $CaII$ infrared triplet emission. The third, with less stringent constraints (8750 $K \leq T \leq 1.25 \times 10^4$ K, N_H around 10^{11} cm^{-3}), produce primarily hydrogen emission. When the second set is present, the first set is often present concurrently. The third set is present either by itself or concurrently with the first set. It is also likely to be present when both the first and second sets are.

7. Line Fluxes and Sizes of Emission Regions

As mentioned in §2, the specific flux $F_{v_{obs}}$ of an optically thick line depends on the line excitation temperature and the emission area with a projected velocity of v_{obs}, $A_{v_{obs}}$. The excitation temperature, in turn, depends on the local physical conditions (N_H, T, etc.) and the emission area depends on the specific kinematic model. In particular, for $|v_{obs}| = 150$ km s^{-1} a spherical wind model with $r = 4R_*$ has $A_{v_{obs}} = 27(r/4R_*)^2$ πR_*^2 and some leeway in its adjustment by varying r, while a spherical infall model with $r = 2.5R_*$ has $A_{v_{obs}} = 1.286\pi R_*^2$ and little room for maneuver. In a CTTS either wind or accretion flow likely fills only a fraction, f_Ω, of the 4π solid angle. This dilution affects the actual observed area in a way that depends on viewing angle, whose variation is not included here to keep the paper manageable. We simply assume an effective observed area given by $f_\Omega A_{v_{obs}}$. Thus, for the same excitation temperature the line flux in the infall model will be $(0.2/0.5)(1.286/27)$ or $1/52.5$ of that in the wind model. We think this is a conservative estimate in that the true ratio is likely smaller.

For ease in comparison with an observed line, we scale the model $F_{v_{obs}}$ to the continuum flux F_c, and present the ratio $y_{v_{obs}} = F_{v_{obs}}/F_c$ as a function of density or line optical depth. Our model continuum is represented by a 4000 K blackbody veiled by a 8000 K blackbody over 3% of its surface. Thus our model continuum has a veiling contribution at $HeI\lambda5876$ of $r_V = 0.67$ and one at $HeI\lambda10830$ or $Pa\gamma$ of $r_Y = 0.19$. When a CTTS has a different T_*, r_V, or r_Y the model $y_{v_{obs}}$ can be easily rescaled to compare directly with the observed line profile.

We shall make use of the information deduced from line ratios to identify the appropriate physical conditions. Since we are calculating the specific flux at $|v_{obs}| = 150$ km s^{-1} it is

the ratio of $F_{v_{obs}}$s that is pertinent here. If the two lines have similar profiles, this ratio is close to the ratio of their integrated fluxes, which was used in §6 to identify the physical conditions responsible for the bulk of the emission. This appears to be the case among $HeI\lambda\lambda10830, 5876$, and $Pa\gamma$. However, $CaII\lambda8498$ is distinctly narrower than $Pa\gamma$. The contrast is obvious in DR Tau , noticeable in DG Tau, and measurable in DL Tau (Edwards et. al 2010). When we come to discussing the $CaII\lambda8498$ specific flux we will take note of the distinction.

7.1. $H\alpha$, $Pa\gamma$, $Pa\beta$, $Br\gamma$

In this subsection we select among the hydrogen lines for presentation $H\alpha$, the strongest optical member, and $Pa\gamma$, $Pa\beta$, and $Br\gamma$ for the availability of large data sets (EFHK06, Folha & Emerson 2001).

Figures 19 and 20 show, for the wind and infall model respectively, how the $H\alpha$ and $Pa\gamma$ specific fluxes depend on N_H and line optical depth. The y-axis limits in Figure 20 are 1/52.48 (-1.72 in log) of those in Figure 19, so chosen that, if the specific flux in the infall model is 1/52.48 of that in the wind model, the two figures will be visually identical. They do look very much alike. When one figure is overlaid on the other, the largest difference in the density dependence plots occurs for $y_{v_{obs}}(H\alpha)$ at $N_H \sim 10^9$ cm^{-3}, where the line emissivity is contributed primarily by stimulated absorption of the incident continuum flux which is a factor of 2.56 larger at $r = 2.5R_*$. The optical depth dependence plots, when overlaid together, show larger differences. This is because at the same τ ($\propto N_l$ r/v) the density in the $r = 2.5R_*$ case is higher and the line specific flux is more sensitive to density than to the velocity gradient, as will be propounded next.

Figures 19 and 20 show not only that the primary distinction in the specific flux produced between the wind and infall models arises from the emission area, but also that variation in the velocity gradient (a factor of 1.6 larger in the $r = 2.5R_*$ model) generates only a small change. As a specific example, we consider the case of $N_H = 10^{11}$ cm^{-3} and $T = 10^4$ K, conditions suitable to bringing about the observed $Pa\gamma/Pa\beta$ ratio. The value of $y_{v_{obs}}(Pa\gamma)$ in the wind model is 3.81, while that in the infall model is $0.7242 = 3.802/52.5$. Their nearly identical emissivity, $y_{v_{obs}}/(f_\Omega A_{v_{obs}})$, is not surprising since $Pa\gamma$ is very optically thick ($\tau_{Pa\gamma} = 33.44$ and 20.46 in the wind and infall model respectively, cf. Figs. 19 & 20 right bottom panel). Even when $Pa\gamma$ is optically thin, the difference in emissivity is small. For example, at $N_H = 10^{10}$ cm^{-3}, $T = 10^4$ K, $y_{v_{obs}} = 0.356$ and $\tau_{Pa\gamma} = 1.63$ in the wind model, while $y_{v_{obs}} = 4.78 \times 10^{-3} = 0.251/52.5$ and $\tau_{Pa\gamma} = 0.355$ in the infall model. The $Pa\gamma$ emissivity is a factor of 1.41 smaller with the larger velocity gradient. However, at the next

density step of 1.585×10^{10} cm^{-3}, $y_{v_{obs}} = 0.0154$ in the infall model or a factor of 3.22 larger than the earlier value. From the slope of the $\log y_{v_{obs}}$ dependence on $\log N_H$ at 10^{10} cm^{-3} it can be estimated that the larger velocity gradient by a factor of 1.6 can be compensated by an increase in N_H by a factor of only 1.147 to produce the same line emissivity. For this reason, even though we emphasize the location where $|v| = 150$ km s^{-1}, the local excitation calculations of line emissivities and ratios are applicable elsewhere because a large variation in the local velocity gradient is tantamount to only a modest variation in the density.

The two figures also show that over the density range 2×10^{10} $cm^{-3} < N_H < 2 \times 10^{12}$ cm^{-3} the dependences of $y_{v_{obs}}(H\alpha)$ and $y_{v_{obs}}(Pa\gamma)$ on temperature are strong for 5000 $K \leq T \leq 8750$ K, but weak for 8750 $K \leq T \leq 3 \times 10^4$ K. This is because, despite the stronger collisional excitation with T increasing above 8750 K, the concomitant more rapid buildup of population into high n levels produces a stronger collisional ionization and reduces the neutral fraction.

The 38 $Pa\gamma$ profiles in the reference sample of EFHK06 provide a convenient data set of $y_{v_{obs}}$s for comparison with our model results. To avoid the difficulty of extracting the underlying red emission when a red absorption is obviously or probably present, we concentrate on the blue wing emission and determine $y_{v_{obs}}$ at $v_{obs} = -150$ km s^{-1}. Of the 38 objects, 9 (DR, CW, DL, HL, DG, DK & HN Tau, AS 353 A, RW Aur A) have high $1\mu m$ veiling ($r_Y \geq 0.5$), of whom 8 have $y_{v_{obs}} > 0.25$ and 1 (DK Tau) has $y_{v_{obs}} \sim 0.15$; 11 (DS, HK, BP, DF, DO, GG, & GK Tau, YY, & GW Ori, UY Aur, UZ Tau E) have intermediate $1\mu m$ veiling ($0.3 \leq r_Y \leq 0.4$), of whom 10 (excepting GK Tau) have $0.1 \leq y_{v_{obs}} \leq 0.25$. Of the remaining 18 objects with low $1\mu m$ veiling ($r_Y \leq 0.2$), 2 (SU Aur, TW Hya) have $y_{v_{obs}}$ between 0.1 and 0.25, and the rest have $y_{v_{obs}} < 0.1$.

For members in the first veiling group, our model $y_{v_{obs}}$s, when scaled to the CTTS's stellar plus veiling continuum, need to be reduced by a factor of ~ 2 or more. Then, at the physical conditions needed to produce the Pa $n_u/Pa\beta$ ratios (N_H centered around 10^{11} cm^{-3}, $T \geq 8750$ K, or N_H centered around 5×10^{11} cm^{-3}, $T = 7500$ K, cf. §6.2.2 & Fig. 13) and assuming that these ratios of integrated fluxes are the same as the ratios of specific fluxes at $v_{obs} = -150$ km s^{-1}, the $y_{v_{obs}}$ values in the infall model will be less than 0.05. They fail to produce the values of those 9 objects by factors ranging from ~ 3 to ~ 15. We therefore conclude that a kinematic flow other than accretion infall is responsible for those hydrogen emission. We also draw the same conclusion for the majority of the members in the second $1\mu m$ veiling group. The infall model has difficulty not only accounting for their specific fluxes at $v_{obs} \leq -150$ km s^{-1} but also their observed line wing asymmetry (say, at $|v_{obs}| \geq 150$ km s^{-1}). Thus, whereas in the infall model the blue wing emission is occulted by the star and therefore expected to be weaker than the red wing emission, only GK Tau

shows this characteristic, 2 (DF & DO Tau) have comparable blue and red wing emission, and the remaining 8 have stronger blue wing emission. To be sure, DS Tau and YY Ori have obvious red absorptions, and DK Tau and UY Aur may have weak red absorptions that make it difficult to discern the underlying red wing emission; nevertheless, the lines of sight that favor seeing a red absorption are also the ones that incur stellar occultation of the blue wing emission. Then the earlier conclusion with regard to the high veiling group also implies that whatever kinematic region responsible for their hydrogen emission can also produce the moderate hydrogen emission seen in the second $1\mu m$ veiling group.

The wind model poses the opposite conundrum in that the model $y_{v_{obs}}$s are much larger than those observed in the high $1\mu m$ veiling group, by factors of about 4-10. It can be responsible for the observed hydrogen emission provided the optically-thick emitting gas ($\tau_{Pa\gamma} > 10$, cf. Fig. 19 right bottom panel) fills only a portion of the postulated flow, and covers but a fraction of the contour surface shown in Figure 1. This also happens to be the necessary proviso to avoid the occurrence of a blue absorption. Thus the wind flow needs to be highly inhomogeneous, with the density of the emitting gas considerably higher than that pervading the bulk of the flow. The temperature of the emitting gas is probably $\leq 10^4\ K$, since the line emissivity at a higher temperature is not higher and the filling factor likely decreases rapidly with increasing temperature above $10^4\ K$, owing to the stronger cooling at a higher temperature. It is also probably $> 7500\ K$, otherwise the density needed to produce the $Pa\ n_u/Pa\beta$ ratios would be around $6 \times 10^{11}\ cm^{-3}$, an order of magnitude greater than that needed at $T \geq 8750\ K$, yet the $Pa\gamma$ emissivity is about the same, so the filling factor required of the gas at $N_H \sim 6 \times 10^{11}\ cm^{-3}$ is as high and therefore more restrictive.

Among the optical hydrogen lines $H\alpha$ has the highest optical depth, $\sim 3 \times 10^3$. This can be seen from Figure 19 which shows that at $N_H = 10^{11}\ cm^{-3}$ and $T = 10^4\ K$ $\tau_{H\alpha}$ exceeds 10^3, the upper bound on the abscissa. The high $\tau_{H\alpha}$ leads to a fair amount of emission in the damping wings and likely accounts for the conspicuous extension of the observed $H\alpha$ profile at the base. Thus, assuming just natural broadening of the emission profile, the rate of emitting $H\alpha$ photons that are displaced from line center by $\geq x$ thermal widths is $n_u A_{H\alpha} 2a/(\pi x)$, where $a = \Gamma_R/(4\pi\Delta\nu_D)$, Γ_R is the summed radiative decay rate from the upper and lower states of $H\alpha$, and $\Delta\nu_D$ the thermal Doppler frequency width. It is assumed that x is sufficiently large that the emission is not re-absorbed. With the total $H\alpha$ emission rate being $n_u A_{H\alpha}\beta_{H\alpha}$, the fraction of photons emitted beyond x thermal widths is then $2a/(\pi x \beta_{H\alpha})$. At $10^4\ K$ the thermal Doppler velocity width is $\sim 13\ km\ s^{-1}$, so for $x = 27$, the fraction of $H\alpha$ photons emitted at $|v_{obs}| \geq 350\ km\ s^{-1}$ is ~ 0.16.

Figure 21 shows the analogous plots of $Pa\beta$ and $Br\gamma$ for the infall model. The stellar plus veiling continuum at $1.28\mu m$ of the CTTSs in the sample of Folha & Emerson (2001) is not

listed but most likely significantly stronger than our model value because of the typically high $1\mu m$ veiling observed and probable contribution from dust emission (Muzerolle et al. 2003). Even assuming that our model continuum is representative, the model $y_{v_{obs}}(Pa\beta)$, at the appropriate conditions indicated by the $Pa\,n_u/Pa\beta$ ratios, is ≤ 0.15 and falls short of quite a few observed values. Thus, among the 49 objects with $Pa\beta$ profiles 8 (DG, DL, DR, HL, & CW Tau, GM, & RW Aur, YY Ori) have, at $v_{obs} = -150\ km\ s^{-1}$, $y_{v_{obs}} \geq 0.5$, 8 (GG, RY, DO, DS, & FS Tau, UY, & SU Aur, V1331 Cyg) have $0.2 \leq y_{v_{obs}} < 0.5$, and 10 (BM And, DE, DF, DK, HK, BP, GI, HP, & T Tau, GW Ori) have $0.1 \leq y_{v_{obs}} < 0.2$. Again then, a comparison between model results and $Pa\beta$ data leads to the same conclusions deduced earlier. It is interesting that the objects with strong (moderate) $Pa\beta$ flux at $|v_{obs}| \geq 150\ km\ s^{-1}$ also have strong (moderate) $Pa\gamma$ flux. This may simply be a confirmation of both the finding of Bary et al. (2008) that the $Pa\gamma/Pa\beta$ ratio does not vary strongly among CTTSs and the assumption of similar $Pa\gamma$ and $Pa\beta$ profiles.

In summary, based on the hydrogen line specific fluxes at $|v_{obs}| \geq 150\ km\ s^{-1}$, we arrive at the following conclusions regarding the infall accretion and wind flows.

1. The infall accretion flow is not responsible for the strong or moderate hydrogen emission at $|v_{obs}| \geq 150\ km\ s^{-1}$. We can extend this inference to the bulk of the observed emission for the following reasons. First, the emission generated by gas with $|v| \geq 150\ km\ s^{-1}$ is a substantial fraction of the total, since the same particles also contribute to observed emission at $|v_{obs}| < 150\ km\ s^{-1}$ when their trajectories do not parallel the line of sight. A rough estimate of the line profile produced by them in an azimuthally symmetric distribution is a flat-top shape in the regime $-150\ km\ s^{-1} \leq v_{obs} \leq 150\ km\ s^{-1}$. Using this guideline to determine the fraction of the blueward emission (to avoid the red absorption), we find from Figure 3 of EFHK06 that 19 (excepting GK Tau) of 20 CTTSs in the high and intermediate veiling groups ($r_Y \geq 0.3$) have this fraction ≥ 0.5. Second, with the velocity distribution expected to be a smooth function, the infall model will also have difficulty accounting for the observed specific fluxes at $|v_{obs}|$ somewhat less than $150\ km\ s^{-1}$. Third, whatever kinematic structure called for to produce the observed emission at $|v_{obs}| \geq 150\ km\ s^{-1}$ will likely have gas particles moving at $< 150\ km\ s^{-1}$. All these considerations lead us to conclude that the bulk of the $Pa\gamma$ emission in these CTTSs arise from a kinematic structure other than the accretion flow.

2. For the wind flow to be responsible for the moderate or strong hydrogen emission the emitting gas, whose density is considerably higher than that of the gas occupying the bulk of the flow, can only fill a small fraction of the volume.

These conclusions remain true, of course, when the two flows are compared at the lower ionization rate of $\gamma_{HI} = 2 \times 10^{-5}\ s^{-1}$. For either flow the specific fluxes are almost identical

to those in the $\gamma_{HI} = 2 \times 10^{-4}$ case at $T \geq 8750\ K$, and are weaker at $T \leq 7500\ K$, as can be deduced from the contrast in the $\tau_{Pa\gamma}$ contours between the two ionization cases (Fig. 4). Thus, for $(H\alpha,\ Pa\gamma)$ the $y_{v_{obs}}$s at $N_H = 10^{11}$ and $10^{12}\ cm^{-3}$ with $\gamma_{HI} = 2 \times 10^{-5}\ s^{-1}$ are smaller by a factor of $(2.55,\ 4.14)$ and $(1.06,\ 1.16)$ respectively at $T = 7500\ K$, and $(3.67,\ 6.64)$, and $(1.92,\ 2.69)$ respectively at $T = 5000\ K$. This dependence of $y_{v_{obs}}$ on γ_{HI} when T is $\leq 7500\ K$, as well as $y_{v_{obs}}$'s rapid rise with T increasing above $7500\ K$ at a given γ_{HI} lead us to favor the temperature in the hydrogen emission region being $\geq 8750\ K$.

7.2. $HeI\lambda\lambda10830, 5876$

Figures 22 and 23 show the $HeI\lambda\lambda10830, 5876\ y_{v_{obs}}$s as a function of density and line optical depth for the wind and infall model respectively. Like the $HeI\lambda5876/\lambda10830$ ratio, the model results for the HeI specific fluxes at $T = 3 \times 10^4\ K$ are very close to those at $T = 2 \times 10^4\ K$ and are not shown.

The 22 $HeI\lambda5876$ broad-component profiles in Figure 7 of BEK01 present a convenient data set for comparison with our model results. We again look at the specific flux at $v_{obs} = -150\ km\ s^{-1}$ to avoid the red absorption which appears to affect several profiles. The 22 optical veilings range from 0.1 to 20, and the observed $y_{v_{obs}}$s range from 0.01 to 0.5, but the correlation between $y_{v_{obs}}$ and r_V does not appear to be strong. Eight objects (CW, HN, DG, DL, & DR Tau, AS 353 A, RW & UY Aur) have $0.2 \leq y_{v_{obs}} \leq 0.5$ and r_V between 0.8 and 20, 4 (GG, DQ, & DF Tau, GM Aur) have $0.1 \leq y_{v_{obs}} < 0.2$ and r_V between 0.2 and 0.7, and the rest have $y_{v_{obs}} < 0.1$ and r_V between 0.1 and 4.7. With our model r_V of 0.67, the model $y_{v_{obs}}$s likely need to be lowered (raised) for comparison with the first (second) veiling group. Even for observed $y_{v_{obs}}$s as high as 0.5, it appears that the infall model can accommodate them. As a specific example, we assume that the $HeI\lambda5876/\lambda10830$ ratio is 0.4 and determine from Figure 8 that the required physical conditions can be $(T = 2 \times 10^4\ K,\ N_H = 1.1 \times 10^{11}\ cm^{-3})$, $(T = 1.5 \times 10^4\ K,\ N_H = 3.2 \times 10^{11}\ cm^{-3})$, or $(T = 1.25 \times 10^4\ K,\ N_H = 1.5 \times 10^{12}\ cm^{-3})$ which produce, as seen from Figure 23, a $y_{v_{obs}} \sim 0.6$ in each case. The $HeI\lambda5876$ optical depth is greater than 50 (cf. Fig. 23 right bottom panel), so a red absorption will be seen for certain lines of sight. For smaller observed $y_{v_{obs}}$s, however, a small filling factor of the emitting gas can be invoked to reduce the incidence of red absorption.

The $1\mu m$ spectroscopic survey of CTTSs by EFHK06 also procures a set of $HeI\lambda10830$ profiles. Most of them have strong absorption features, so we consider solely the high $1\mu m$ veiling group ($r_Y \geq 0.5$) whose members are among the objects with the strongest $HeI\lambda10830$ emission. Excluding DK Tau which has only absorption features, we determine the $y_{v_{obs}}$s at $v_{obs} = 150\ km\ s^{-1}$ to avoid the blue absorptions. They range from 0.3 to 1.3. Our model

r_Y is 0.19, but even lowering the model $y_{v_{obs}}$s considerably for comparison with the CTTSs with particularly high r_Ys, it appears that the infall model can produce the highest observed $HeI\lambda10830$ specific fluxes.

For both $HeI\lambda10830$ and $\lambda5876$ it is also clear that their emission are far too strong in a laminar wind flow, and that the gas producing the helium emission can only occupy a fraction ≤ 0.01 of the contour area shown in Figure 1 in order to match the observed specific fluxes.

While the above analysis does not directly reject either model, we favor the wind region as the production site of strong helium emission for the following reasons.

1. Except near the accretion shock where UV photons are produced, the required temperature of $T \geq 1.25 \times 10^4$ K is difficult to generate and maintain in an accretion flow, which is primarily in free fall. On the other hand, it is reasonable to expect that acceleration of the gas in a wind would produce heating. Helium emission in the wind is also compatible with the earlier deduced condition for hydrogen emission in the wind in that the decreasing filling factor of the gas with increasing temperature from 10^4 to $\sim 2 \times 10^4$ K is consistent with the cooling and expansion of gas at a higher temperature.

2. An infalling flow is hard pressed to explain the strong blue asymmetry in the $HeI\lambda5876$ line wings. Judging the emission at $|v_{obs}| \geq 150$ km s^{-1} (cf. Fig. 7 of BEK01), we find that 18 of the 22 $HeI\lambda5876$ broad components are stronger on the blue side, although 3 of them (AS 353 A, RW & GM Aur) have red absorptions that clearly accentuate the asymmetry, 3 (DD, DF, & DO Tau) are stronger on the red side, and 1 (DE Tau) is too weak to discern. While lack of azimuthal symmetry or strong local inhomogeneities can generate asymmetries in the wing emission, their numbers of blue and red asymmetries should, for random lines of sight, statistically balance out. On the other hand, stellar occultation of the approaching accretion flow and disk occultation of the receding wind flow produce always a red and blue asymmetry respectively. As seen from Figure 1, the projected area of the $v_{obs} = -150$ km s^{-1} contour in the infall model is only slightly larger than the projected stellar surface area. There is little leeway in adjusting the accretion flow geometry to avoid diminishing the blue wing emission, let alone enhancing it above the red wing emission.

3. The accretion flow model has greater difficulty producing the $HeI\lambda10830$ profile morphologies of those objects with strong emission (cf. Fig. 4 of EFHK06). First, while most of the 38 objects have blue and/or red absorptions that make it difficult to decipher the wing emission at $|v_{obs}| \geq 150$ km s^{-1}, 4 have mostly emission, of whom BP Tau's wing emission is too weak to compare its two sides and the remaining 3(CW & HN Tau, RW Aur A) all have stronger blue wing than red wing emission, and will pose a challenge to the

infall model. Second, when emission above continuum is observed along with absorption, the objects with strong emission tend to associate with blue absorptions indicative of a stellar wind (cf. Fig. 10 of Kwan et al. 2007), whereas the objects with strong absorptions on the red side only do not have comparably strong emission (e.g., AA Tau, BM And, RW Aur B, LkCa 8 in Fig. 4 of EFHK06 or Fig. 2 of Fischer et al. 2008). The latter appear to have both a lower r_Y and a smaller equivalent width in the emission above the continuum. Bearing in mind that the observed emission is contributed in part already by scattering of continuum photons, it is surprising, if the accretion flow is the site of helium emission, that the in-situ emission are relatively weak in those accretion flows with particularly large widths and sizes that are needed to produce the broad and deep red absorptions (cf. §4.2 & 4.3 of Fischer et al. 2008). On the other hand, the above-mentioned correlation naturally follows if the wind flow is the site of helium emission. Also, in producing the needed in-situ emission there is more leeway afforded the wind model in the choices of r and filling factor of the high temperature regions. The Monte Carlo simulations by Kwan et al. (2007) already indicate that the $HeI\lambda10830$ profile morphologies can be accounted for by a stellar wind, depending on the opening angle of the wind and the viewing angle. However, in light of the present finding that the emission regions do not occupy the bulk of the volume, there is the constraint that these regions share the velocity distribution of the gas occupying the bulk of the volume and responsible for the $HeI\lambda10830$ absorption.

In §6.1 where the $HeI\lambda5876/\lambda10830$ and $Pa\gamma/HeI\lambda10830$ ratios are discussed it was mentioned that, even though their model values generated at $T = 5000~K$, $5 \times 10^{10}~cm^{-3} \leq N_H \leq 10^{12}~cm^{-3}$ are closest to the observed values (cf. Fig 10), several reasons argue for a higher temperature. One, given in §6.2.2, is based on the difficulty of simultaneously matching $Pa\gamma/Pa\beta$ at $T = 5000~K$. We add a second reason here, based on the weakness of the $HeI\lambda5876$ flux at $T = 5000~K$. As seen from Figure 22, its model $y_{v_{obs}}$ in the wind model increases from 0.1 to 1.3 as N_H increases from 5×10^{10} to $10^{12}~cm^{-3}$. Reducing it by a factor of 2 upon rescaling it to the continua of the 8 objects with r_Vs between 0.8 and 20 and observed $y_{v_{obs}}$s between 0.2 and 0.5, it is clear that the emitting gas need to fill a substantial portion of the contour surface shown in Figure 1 in order to match the observed values. This would, however, produce a blue $HeI\lambda5876$ absorption which is never seen.

As T increases from $5000~K$, the $HeI\lambda5876/\lambda10830$ ratio first decreases (cf. Fig. 8) and then rises again when T exceeds $10^4~K$, so we expect the helium emission to arise from regions of temperature above $10^4~K$. With T increasing from 10^4 to $2 \times 10^4~K$, the specific fluxes of both $HeI\lambda5876$ and $\lambda10830$ increase rapidly (cf. Fig. 22), but then stay nearly constant for T between 2×10^4 and $3 \times 10^4~K$. If regions in the wind flow are raised to temperatures above $2 \times 10^4~K$ before cooling and expansion come into play, we anticipate them to be most effective in contributing to the observed helium emission when they are at

temperatures near 2×10^4 K.

When γ_{HeI} is reduced from 10^{-4} to 10^{-5} s^{-1} the specific fluxes of both $HeI\lambda10830$ and $\lambda5876$ remain almost the same for $T \geq 1.5 \times 10^4$ K, but fall rapidly for $T < 1.5 \times 10^4$ K. This result can be anticipated from the large difference in the $\tau_{HeI\lambda10830}$ or $\tau_{HeI\lambda5876}$ contour between the two cases of γ_{HeI} in the temperature range 10^4 $K < T < 1.5 \times 10^4$ K (cf. Fig. 4). This strong dependence of HeI emission on γ_{HeI} in that temperature regime, and the need for a higher density to obtain the same $HeI\lambda5876/\lambda10830$ ratio as T decreases from 2×10^4 K lead us to favor a temperature range from 1.5×10^4 to 2×10^4 K for the $HeI\lambda5876$ emission.

7.3. $CaII\lambda8498$, $OI\lambda8446$

It was pointed out in §6.3.2 that the observed $CaII\lambda8498/Pa\gamma$ ratios of integrated fluxes appear to fall into two groups and, earlier in §7, that the strong $CaII\lambda8498$ lines are narrower than $Pa\gamma$. For those objects with $CaII\lambda8498/Pa\gamma \sim 1$ or less, the $CaII$ emission can be produced by the set of physical conditions (8750 $K \leq T \leq 1.25 \times 10^4$ K, N_H around 10^{11} cm^{-3}) producing primarily hydrogen emission. The larger issue, of course, concerns the strong emitters with $CaII\lambda8498/Pa\gamma$ greater than ~ 5. Their $CaII$ profiles appear narrower than the $Pa\gamma$ profiles in the data set of Edwards et al. (2010). There may already be a hint of this property from a comparison of non-simultaneous $CaII$ and $Pa\gamma$ profiles. Thus, the ratio of specific flux at $v_{obs} = -150$ km s^{-1} to that at $v_{obs} = 0$ is smaller for $CaII\lambda8542$, being 0.27, 0.1, and 0.4 for DG, DR, and DL Tau respectively (Muzerolle et al. 1998b), than for $Pa\gamma$, being 0.46, 0.33, and 0.54 (EFHK06).

In view of the possibly different $CaII\lambda8498$ and $Pa\gamma$ profiles, we will, in comparing between model and observed values of the $CaII\lambda8498$ specific flux at $v_{obs} = -150$ km s^{-1}, not utilize the constraint imposed on the physical conditions by the $CaII\lambda8498/Pa\gamma$ ratio of integrated fluxes, and consider all densities in the regime $5000 \leq T \leq 1.25 \times 10^4$ K as possible. Figure 24 shows the dependences of $y_{v_{obs}}$ on N_H, T, and line optical depth for the infall model. The observed values of DG, DR, DL Tau and RW Aur are 1.4, 0.6, 2.5 and 3.7 (Muzerolle et al. 1998b). Anticipating that the model $y_{v_{obs}}$s have to be reduced by a factor of ≥ 2, owing to the strong veilings at $\lambda8498$ (between 0.7 and 5.1) of those objects, we find that, with the exception of RW Aur, the infall model can produce the wing emission. We do not consider this strong enough evidence to argue against the infall model.

The issue concerning the strong $CaII$ emission is, of course, its emission near line center. While our specific flux calculation provides no aid in discriminating between the wind and

infall models, the earlier derivation of requisite physical conditions for strong $CaII$ emission (i.e., $T \leq 7500~K$, N_H close to $10^{12}~cm^{-3}$) remains true, because of the much stronger dependence of the specific fluxes and flux ratios on N_H or T than on the velocity gradient. With this in mind, we do not think the wind region is the site of strong $CaII$ emission for the following reasons.

1. The physical condition of high density and low temperature is incongruous with that inferred from the helium and hydrogen emission, and with the constraint imposed by the lack of blue absorption in $Pa\gamma$. With the bulk of the wind region occupied by gas at a density of $< 10^{10}~cm^{-3}$ (cf. Fig. 4), the hydrogen emitting regions at $T \leq 1.25 \times 10^4~K$ and $N_H \sim 10^{11}~cm^{-3}$, and the indication that lower temperature is associated with lower density and larger filling factor, it does not appear the wind region has the physical conditions needed for strong $CaII$ emission.

2. The strong $CaII$ emission has a linewidth narrower than the $Pa\gamma$ width or the typical velocity extent seen in a broad, blue $HeI\lambda10830$ absorption. If $CaII$ emission originates from the wind region, it is surprising , particularly in the case of DR Tau, that, while the $Pa\gamma$ and $HeI\lambda5876$ line shapes are quite similar, the $CaII$ line shape is so different.

3. The strong $CaII$ line appears symmetrical about line center. It does not have the characteristic feature of a stronger blue emission as exhibited often by $Pa\gamma$ and $HeI\lambda5876$, and attributable to disk occultation of the receding wind.

The strong $CaII$ emission near line center can be produced in an accretion flow. Its narrower width and different line shape from $Pa\gamma$ will not be issues. The condition of $T \leq 7500~K$ is not unreasonable in light of Martin's (1996) calculation of the thermal structure of the infalling gas, and the density criterion of close to $10^{12}~cm^{-3}$ may not be too restrictive a constraint on the mass accretion rate if the flow is dilutely filled. There is a second possible site, the disk boundary layer where the gas dissipates part of its rotational energy before infalling along a stellar magnetic field line. We will elaborate on our preference in the next section when all the deductions and arguments put forth in §§5, 6, 7 are synthesized.

We will not comment much on the $OI\lambda8446$ specific flux. Our calculations indicate that the specific flux of $OI\lambda8446$ rises more rapidly than $Pa\gamma$ with N_H increasing from 10^{11} to $10^{12}~cm^{-3}$, causing $OI\lambda8446/Pa\gamma$ to be higher at the conditions suitable for strong $CaII$ emission. Thus there is a larger contribution to the $OI\lambda8446$ line from the $CaII$ emission region than is the case for $Pa\gamma$.

8. Origins of the Strong H, HeI, and $CaII$ Line Emission

In §§5, 6 we have presented calculations that shed light on the physical conditions giving rise to the absorption and emission features of most of the prominent lines observed in CTTSs. These are excitation calculations that include all the important physical processes affecting the atomic/ionic level population. They are facilitated by the presence of large velocity gradients expected in a wind or infalling flow in that the level population depend only on the local density (N_H), temperature (T), photon ionization rate (γ_{HeI}), and velocity gradient ($2v/r$). Thus the resulting line emissivity ($erg\ s^{-1}\ cm^{-3}$) can be calculated in the (N_H, T, γ_{HeI}, $2v/r$) parameter space and the ratio of two line emissivities will demarcate the requisite physical conditions. One of our findings is that the H and HeI emission regions can occupy only a very small fraction of the wind flow. Our use of $2v/r$ for the velocity gradient is then inaccurate, and a more suitable choice would be $\delta v/\delta l$, where δl is the linear dimension of an emission region and δv the thermal/turbulence velocity width. However, as demonstrated in §7.1, the line emissivity is much more sensitive to N_H than to $2v/r$ or $\delta v/\delta l$, particularly when the line is optically thick, as is true for the H, HeI, and $CaII$ lines studied, so a large change in $2v/r$ or $\delta v/\delta l$ occasions only a small change in N_H. Because the requisite physical conditions deduced for the gases responsible for the $HeI\lambda10830$ absorption, H emission, HeI emission, and $CaII$ emission are so disparate, we are confident our conclusions are not fundamentally altered by the uncertainty in this parameter. For the same reason, even though we emphasize the two locations of $r = 4$ and $2.5R_*$ and the velocity $v = 150\ km\ s^{-1}$, the results on the ordering of line opacities and the responses of line emissivity ratios to N_H, T, and γ_{HeI} are applicable to other locations and not sensitive to the kinematic structure. Then in §7 we distinguish between the wind and accretion flows by evaluating the specific fluxes of the more important lines at $|v_{obs}| = 150\ km\ s^{-1}$. Here we recapitulate and synthesize the deductions reached separately in §§5, 6, 7 and, in conjunction with other arguments, decide on the locations of the H, HeI, and $CaII$ line emission.

Our conclusions drawn with regard to the H, HeI, and $CaII$ broad line emission in the following subsections apply only to the strong emitters, specific examples of which have been mentioned in §§6, 7. This qualification arises for the following reasons. First, the determination of observed line ratios, particularly $HeI\lambda5876/\lambda10830$, is not as reliable for weak emitters because of the presence of absorption features and the contribution to emission from scattering of continuum photons. Second, a couple of our arguments concern the limitations of an infalling flow on the production of line photons, and therefore hinge upon the observational bar placed by the strong emitters.

8.1. Physical Conditions of the Gases Producing Emission and Absorption Lines

Below we summarize and discuss the findings obtained from a comparison between model results and observational data on line opacities and line ratios. They shed light on the properties of the gases responsible for the emission and absorption lines.

1. Optically thick H and HeI emission lines. The gases producing the $HeI\lambda\lambda10830, 5876$ and $Pa\gamma$, $Pa\beta$ emission are very optically thick in those lines, in order to produce the observed $HeI\lambda5876/\lambda10830$, $Pa\gamma/Pa\beta$, and $Pa\gamma/HeI\lambda10830$ ratios (cf. §§6.1.2., 6.2.2.).

2. Separate physical conditions for H, HeI, and $CaII$ emission. The need for distinct physical conditions conducive to H and HeI emission is demonstrated clearly in Figure 10 where it is seen that many of the marked CTTSs, which are among the strong $HeI\lambda5876$ emitters, have $HeI\lambda5876/\lambda10830$ and $Pa\gamma/HeI\lambda10830$ ratios that cannot be simultaneously produced with a common temperature range, but must require that the bulk of the $HeI\lambda5876$ emission be produced at temperatures higher than those producing the bulk of the $Pa\gamma$ emission (cf. §6.1.2.).

For the strong $HeI\lambda5876$ emission we favor the temperature range $1.5 \times 10^4\ K \leq T \leq 2 \times 10^4\ K$. The upper bound is adopted because the line emissivity at a higher temperature is not higher (§7.2), while presumably the emission area is smaller. The lower bound is adopted because at a lower temperature the line emissivity is much more dependent on γ_{HeI} and a higher density is needed to produce the same $HeI\lambda5876/\lambda10830$ ratio, as seen in Figures 8 and 9 (cf. §7.2). The same figures also show that within the favored temperature range $HeI\lambda5876/\lambda10830$ rises steeply with increasing density, and the density needed to produce $HeI\lambda5876/\lambda10830 \geq 0.3$ is $\geq 10^{11}\ cm^{-3}$.

The physical conditions responsible for H emission, as deciphered by examining the ratios among the hydrogen lines themselves, namely $Pa\ n_u/Pa\beta$ and $Br\gamma/Pa\ n_u$, indicate that N_H is centered around $10^{11}\ cm^{-3}$ for $T \geq 8750\ K$, and $\geq 5 \times 10^{11}\ cm^{-3}$ for $T \leq 7500\ K$ (cf. §6.2.2.). In conjunction with the observed $Pa\gamma/HeI\lambda10830$ ratio, however, the temperature can be narrowed to the range $5000\ K < T \leq 1.25 \times 10^4\ K$. The upper bound comes from the small $Pa\gamma/HeI\lambda10830$ ratio (≤ 0.2) that can only be generated at N_H around $10^{11}\ cm^{-3}$ at $T \geq 1.5 \times 10^4\ K$ (cf. Figs. 8 & 9 right top panel). The lower bound is due to the need of very high densities ($> 2 \times 10^{12}\ cm^{-3}$) to produce $Pa\gamma/Pa\beta > 0.8$ (cf. Fig. 11 left top panel) and the concomitant result of $Pa\gamma/HeI\lambda10830$ lower than observed (cf. Figs. 8 & 9 right top panel, §6.2.2). We further favor the temperature range conducive to H emission being $8750\ K \leq T \leq 1.25 \times 10^4\ K$, because the line emissivities, particularly $Pa\gamma$ and $Br\gamma$, decrease rapidly with T decreasing below $8750\ K$ (cf. Figs. 19,

20, 21 right top panel, §7.1). In this temperature range and with N_H around 10^{11} cm^{-3} the $CaII\lambda8498/Pa\gamma$ ratio is also in line with the observed values among the weak $CaII$ broad emitters (cf. §6.3.2).

The observed $HeI\lambda10830/Pa\gamma$ ratio, typically ~ 1.5 among the strong emitters, also indicates that the HeI emission area is smaller than the H emission area. Thus, if the emission area contributing to HeI emission, primarily with T around 2×10^4 K, were the same as that with T around 10^4 K, $HeI\lambda10830/Pa\gamma$ would be ≥ 10, because while the $Pa\gamma$ emission from each area is about the same (cf. Fig. 19 right top panel) the $HeI\lambda10830$ emission at 2×10^4 K and N_H around 10^{11} cm^{-3} is ≥ 20 times the $Pa\gamma$ emission (cf. Figs. 8 & 9 right top panel).

The physical conditions responsible for strong broad $CaII$ emission are most evident in Figures 17 and 18 where the observed $CaII\lambda8498/OI\lambda8446$ values greater than ~ 7 point to a temperature $T \leq 7500$ K and then from Figure 16 (left top panel) a density N_H close to 10^{12} cm^{-3} (cf.§6.3.2). They can also be inferred from the large $CaII\lambda8498/Pa\gamma$ values. There are, however, also CTTSs observed to have $CaII\lambda8498/OI\lambda8446$ and $CaII\lambda8498/Pa\gamma$ of ~ 1 or less (e.g. BP Tau in Figs. 17 & 18), and $Pa\gamma$ emission strengths not much weaker than those among the strong $CaII$ emitters. Their H and $CaII$ emission indicate 8750 $K \leq T \leq 1.25 \times 10^4$ K and N_H around 10^{11} cm^{-3} (cf. §6.3.2), as mentioned just earlier. Such physical conditions also naturally arise through cooling of the regions responsible for HeI emission, which is often observed to be strong when $CaII$ emission is strong. Thus we conclude that this set of physical conditions producing primarily H emission is also present. It may indeed be the most prevalent since it is needed when both $HeI\lambda5876$ and $CaII$ emission are weak. When the latter emission are strong, the other two sets, namely $(1.5 \times 10^4$ $K \leq T \leq 2 \times 10^4$ K, $N_H \geq 10^{11}$ $cm^{-3})$ for the bulk of the HeI emission and $(T \leq 7500$ K, $N_H \sim 10^{12}$ $cm^{-3})$ for the bulk of the $CaII$ emission, are also present.

The fundamental cause of the distinct sets of physical conditions conducive to H, HeI, and $CaII$ emission is the different H, HeI, and $CaII$ atomic/ionic structures, making their efficacies in photon production sensitive to different temperature ranges. Thus, while $HeI\lambda10830$ and $\lambda5876$ emission rise rapidly with increasing T up to 2×10^4 K, hydrogen emission in Balmer, Paschen, and higher order lines are not more efficient at $T > 10^4$ K because the stronger collisional ionization reduces the neutral hydrogen fraction, and a temperature decreasing below 10^4 K clearly favors $CaII$ over H emission. The separate physical conditions we identify for the H, HeI, and $CaII$ emission regions are therefore understandable and not particular to our excitation model despite its simplifications and approximations.

3. Higher densities for the gases producing the H and HeI emission lines than the gas producing the broad, blue absorption. Broad, blue absorptions indicative of a stellar wind are

often seen in $HeI\lambda10830$ but almost never in $HeI\lambda5876$, $Pa\beta$, or $Pa\gamma$. This observational constraint, in conjunction with finding 1 above, means that a laminar wind will not be able to produce simultaneously the observed absorption and emission features seen in either HeI or H lines. This dilemma is the same as that realized in earlier wind models of hydrogen line emission (Hartmann et al. 1990). Anticipating that the temperature of the gas occupying the bulk of the wind volume is $\leq 10^4$ K, the constraint placed by the observed absorption features limits the density of this gas to be no more than $\sim 10^{10}$ cm^{-3} (cf. Fig. 4), which is considerably lower than the density of the H or HeI emission gas. Thus a highly clumpy flow is called for if the H and HeI emission regions also reside in the wind (cf. §§7.1, 7.2).

4. In order to produce a $\tau_{HeI\lambda10830} \geq 1$ in the radial wind, the minimum density needed at the location where the wind reaches a speed of 150 km s^{-1} is $\sim 5 \times 10^8$ cm^{-3} (cf. Fig. 4), and the corresponding mass loss rate is $\sim 0.5 \times 10^9$ $M_\odot$ yr^{-1}.

5. The red absorption gas has a temperature $T < 10^4$ K and a density N_H greater than or about 10^{11} cm^{-3}. The former condition is needed to ensure a more prevalent occurrence of red absorptions in the NaI doublet than in $Pa\gamma$ (cf. Fig. 6, §5.2). The latter condition is inferred from the observed ordering of the lines in propensity of showing a red absorption.

6. UV photoionization is necessary to produce the broad red and blue absorptions seen in $HeI\lambda10830$. This is demonstrated forcefully by the more prevalent occurrence of red absorptions in $HeI\lambda10830$ than in $Pa\gamma$, given that the low temperature of the absorption gas ($T < 10^4$ K as noted above) renders collisional excitation futile (cf. §5.2). UV photoionization of HeI in the gas occupying the bulk of the wind flow is also needed to produce $HeI\lambda10830$ blue absorptions since it is most likely that the temperature of that gas is also $< 10^4$ K if the hydrogen emission regions occupy only a small fraction of the volume and have a temperature 8750 $K \leq T \leq 1.25 \times 10^4$ K. With the main depopulation path of the highly metastable $HeI\lambda10830$ lower level being collisional excitation to the $2s$ ^1S state, whose rate decreases with decreasing T and N_e, a $\tau_{HeI\lambda10830} \sim 1$ is quite realizable at $T \leq 6250$ K even for low ionization fluxes (cf. §5.1). We therefore think UV photoionization is also the excitation mechanism responsible for the sharp blue absorptions and central absorptions seen in $HeI\lambda10830$.

UV photoionization of HI in the bulk of either the wind or accretion flow is not as crucial, but it likely contributes, particularly if the gas temperature is < 7500 K, given that UV photons are already present for HeI ionization. In the regions producing either H or HeI optical and infrared line emission collisional excitation is the primary mechanism, and UV photoionization plays a less significant role.

We will make use of these findings and additional ones deduced in §7, as well as argu-

ments based on correlations among absorption and emission features, to support our decisions on the emission sites of the strong HeI, H, and $CaII$ lines in the following two subsections.

8.2. Wind Region as the Site of the Strong HeI and H Emission

We first summarize the arguments against the accretion flow as the appropriate site.

1. Difficulty for an infalling flow to account for the stronger blue wing emission. In §§7.1, 7.2 we have listed CTTSs to show that both $Pa\gamma$ and $HeI\lambda5876$ have distinctly a stronger blue wing. In an infalling flow the emission area at $v_{obs} \leq -150$ km s^{-1} is not much larger than πR_*^2 (cf. Fig. 1), so it is very difficult to avoid stellar occultation of the infalling flow approaching an observer. This preferential attenuation of the blue wing emission is intrinsic to the infall flow geometry, but is counter to the observed trend.

2. Difficulty for an infalling flow to produce the observed fluxes in the line wings. The finding that the H and HeI emission lines are optically thick means that their specific fluxes depend on the emission area and the line excitation temperatures. For an infalling flow its geometry severely confines the projected areas with large $|v_{obs}|$s. The hydrogen lines face, in addition, a strong limitation on their excitation temperatures through the $n \rightarrow n + 1$ collisional excitations that lead to rapid ionization at $T > 10^4$ K. As a result we find that the observed $Pa\beta$ and $Pa\gamma$ fluxes at $|v_{obs}| \geq 150$ km s^{-1} cannot be produced by our infall model over the broad ranges of physical parameters explored. This result is not surprising, as it is simply an alternative, albeit more explicit, way of phrasing previous findings that the hydrogen profiles calculated from accretion flow models are narrower than observed (Folha & Emerson 2001). Interestingly, the steep rise of the helium line emissivity with increasing T from 10^4 to 2×10^4 K (cf. Fig. 23) enables the infall model to reproduce the observed HeI line fluxes. However, a temperature $\geq 1.25 \times 10^4$ K is required, and we think it is difficult to heat the gas, which is primarily in free fall, to those temperatures, except possibly near the impact sites where photoionization heating by photons generated in the shocks can be important. It has also been deduced earlier that the gas occupying the bulk of the infalling flow has a temperature $< 10^4$ K, so we do not think the accretion flow generally has the physical conditions conducive to strong HeI emission.

3. Weak or no correlation between strong $HeI\lambda10830$ red absorptions and strong $Pa\gamma$ or $HeI\lambda5876$ emission. If $Pa\gamma$ or $HeI\lambda5876$ is produced in the accretion flow, it is reasonable to expect that presence of a strong $HeI\lambda10830$ red absorption should be accompanied by a strong $Pa\gamma$ or $HeI\lambda5876$ line. From Figures 3 and 4 of EFHK06 it is seen that among the CTTSs with the strongest $HeI\lambda10830$ red absorptions, 2 (DK Tau, YY Ori) have moderate

$Pa\gamma$ emission, but 7 (AA, GI, DN, & V830 Tau, BM And, RW Aur B, LkCa 8) have only weak $Pa\gamma$ emission. In the simultaneous $1\mu m$ and optical data sample of Edwards et al. (2010), of the 6 objects with strong $HeI\lambda10830$ red absorptions, only 1 (DR Tau) has strong $Pa\gamma$ and $HeI\lambda5876$ emission, while the rest (DK, GK, AA, & GI Tau, BM And) have weak $Pa\gamma$ and $HeI\lambda5876$ (broad component) emission.

4. It is noted in §5.2 that when $\tau_{HeI\lambda10830}$ is ~ 1 the $H\alpha$ opacity is close to or higher than $\tau_{HeI\lambda10830}$. Then if the $H\alpha$ emission originate in the accretion flow, which is probably within the radial wind, it will be scattered by the wind, and the resulting observed profile will be highly asymmetric with the red side much strong than the blue side. The collection of 31 $H\alpha$ profiles in Figure 15 of BEK01 shows that such profiles are rare, with AS 353A, DR Tau, and DO Tau being the lone examples.

5. Absence of correlation between $HeI\lambda5876$ broad component and narrow component emission. A narrow line, either on top of a broad one or by itself, is seen in $Pa\gamma$ (EFHK06), the $CaII$ infrared triplet (Muzerolle et al. 1998b), and most frequently and prominently in $HeI\lambda5876$ (BEK01). This observational result is understandable if the narrow line emission is formed in the post-shock regions at the impact sites of the infalling flow on the star, since the HeI lines form at higher temperatures and will likely reach higher excitation temperatures than the H and $CaII$ lines. The $HeI\lambda5876$ narrow component (NC) strength, being sensitive to the surface area of impact and the pre-shock density, is then a good indicator of the accretion flow magnitude. Then, if the $HeI\lambda5876$ broad component (BC) arises from the accretion flow, one would expect a correlation between the BC and NC strengths. Even though, with the available information of BC and NC equivalent widths (W_λ) and red veilings (r_R), a direct plot of the BC flux versus NC flux for the sample of 31 CTTSs cannot be made, we can obtain a sense of this correlation from Figure 1 of BEK01. There it is seen that among those CTTSs with the highest values of $(1 + r_R)W_\lambda$ in the BC 4(CW, HN, & DG Tau, AS 353A) have no or comparatively much weaker NC, 3(DL Tau, RW & UY Aur) have a comparatively weaker NC (but typical, in terms of $(1 + r_R)W_\lambda$ in the NC, relative to the whole sample), and 1 (DR Tau) has a comparatively weaker NC (but strong relative to the whole sample). Then among those CTTSs with the highest values of $(1 + r_R)W_\lambda$ in the NC 2(DD & DO Tau) have a comparable BC, and 2(FM & HK Tau) have no BC. We judge from this comparison between the BC and NC values of $(1 + r_R)W_\lambda$ that there is no correlation between their strengths, and conclude that the broad helium line emission is generally not related to the accretion flow. We can extend this conclusion to the hydrogen line emission. Even though the 38 $Pa\gamma$ profiles in EFHK06 and the 31 $HeI\lambda5876$ profiles in BEK01 are not simultaneous, we see that the group of CTTSs with strong (weak) $HeI\lambda5876$ BC is almost the same as the group of CTTSs with strong (weak) $Pa\gamma$ emission.

While the above-mentioned characteristics of the H and HeI line profiles pose severe difficulties for an infalling flow, they favor a wind flow for the line origin. These include the stronger blue wing emission and the usually blue centroid (both owing to disk occultation of the wind flow receding from an observer), high blue wing velocities (as there is no limitation on the terminal wind speed), and the association of strong H and HeI emission with blue absorptions in $HeI\lambda10830$ that are indicative of a stellar wind. The H and HeI specific fluxes, either at the line wings or at line center, are not fundamental issues in the wind model, even though their observed values, as well as the absence of blue $Pa\gamma$ and $HeI\lambda5876$ absorptions, stipulate that the emission arise from only a small fraction of the wind volume. The physical conditions and filling factors deduced for the H and HeI emission regions may indeed be brought about through the expansion and cooling of high temperature, high pressure clumps. It does remain to be demonstrated, however, that there is a viable acceleration process that produces a highly clumpy flow. Despite this uncertainty, the overall positive comparision between model and observed line profiles and strengths, together with earlier arguments against the accretion flow, lead us to decide squarely on the wind region as the site of the strong H and HeI line emission.

The possibility of strong photoionization heating of the accretion flow near the impact shock, however, means that HeI line emission, possibly strong, may occasionally arise from the accretion flow. In §7.2 it is pointed out that statistically the $HeI\lambda5876$ profiles show a definite preference for a stronger blue wing, but 3 (DD, DF, & DO Tau) clearly have a red centroid (cf. Fig. 7 of BEK01). Such a red asymmetry can be brought about if the emission arise primarily from the part of the accretion flow with a z velocity component towards the disk, specifically the part at polar angle $\theta < 54.7^o$ in a dipolar trajectory, which is the part close to the impact shock (BEK01). The three profiles are much weaker at $v_{obs} \leq -150\ km\ s^{-1}$ than at $v_{obs} \geq 150\ km\ s^{-1}$ and also have strong narrow components. Thus, based on the $HeI\lambda5876$ profile morphologies, an origin of the helium emission in an accretion flow is favored for those three objects. A possible caveat is the uncertain extent to which azimuthal asymmetries in flow geometry and physical conditions affect the profiles. This can only be answered by time monitoring in both optical and $1\mu m$ spectral regions, so that the relative contributions from the radial wind and accretion flow can be assessed through analysis of both $HeI\lambda10830$ and $\lambda5876$ profiles. The great majority of observed HeI profiles, however, show characteristics that favor a wind origin.

8.3.   Disk Boundary Layer and Accretion Flow as Sites of $CaII$ Line Emission

In §7.3 we argue against the wind region as the site of the strong $CaII$ infrared triplet emission and mention that, in addition to the accretion flow, the disk boundary layer is a possible site. In essence this boundary layer, where the accreting particles dissipate part of their rotational energies before falling along the stellar field lines, is the base of the accretion flow. Here we list the reasons why the $CaII$ emission from this base may be significant.

1. The energy dissipated in the disk boundary layer is a significant fraction of the total gravitational potential energy released by the infalling gas. Most of this energy emerges in a photon continuum which we identify as part of the observed continuum excess around $1\mu m$. Like the situation in a stellar atmosphere, the chromospheric region above the continuum formation zone in this boundary layer will produce $CaII$ infrared triplet emission, but the line profile, instead of being narrow, will be Doppler broadened by the strong rotational motion. There appears to be a correlation between the $CaII\lambda 8498$ line strength and the excess $1\mu m$ continuum flux (Fischer et al. 2010)

2. The profiles of the strong $CaII\lambda 8498$ emitters (Muzerolle et al. 1998b, Edwards et al. 2010) appear fairly symmetrical. To be sure the $Pa\,16$ line in the red wing needs to be subtracted, and the profile contains uncertain amounts of contribution from the accretion flow and the hydrogen emission regions in the wind flow. But if this profile characteristic, as well as the narrower width in comparison with the H and HeI lines, holds up in more strong $CaII$ emitters, it is consistent with rotational broadening. The same broadening also produces a depression at line center, but the centrally peaked $CaII$ emission from the accretion flow and from the hydrogen emission regions in the wind flow may fill it up.

3. The continuum produced in the disk boundary layer, like that produced at the accretion footpoints, increases with mass accretion rate, but unlike the latter, also increases with decreasing distance of its location from the star. Thus there may only be a weak correlation between the optical/UV and $1\mu m$ continuum excesses. Then, if the $CaII$ narrow and broad emission arise from the accretion shocks and disk boundary layer respectively, they will reflect a similar relation between their strengths. The 11 $CaII$ line profiles shown in Figure 1d of Muzerolle et al. (1998b) show that the weak broad $CaII$ emitters have small $r_{8600}s$ and distinct narrow components, while the strong broad emitters have larger $r_{8600}s$ and at best weak narrow components, although their appearances are rendered less conspicuous by the presence of the strong broad emission and the stronger underlying continuum. It does appear that the correlation between the $CaII$ broad and narrow emission strengths is weak, but more objects are needed for better statistics.

We are confident that the strong $CaII$ emission do not originate from the wind region,

and think that a good portion of it arises from the disk boundary layer.

9. Discussion

In this section we discuss the implications of the findings described earlier in §8. They include the need of a clumpy wind, identifying the source of ionizing photons, and determining the underlying cause of the correlation between strong $CaII$ and HeI line emission. Most of this discussion is speculative in nature.

A clumpy wind has also been advanced by Mitskevich et al. (1993). Their motivation is to explain the blue absorption seen in $H\alpha$ as being an intrinsic part of line formation in a stellar wind that accelerates to a peak velocity and then decelerates towards zero. Our arguments for a clumpy wind are not dependent on a specific velocity structure. One is based on the lack of blue absorptions in $Pa\gamma$ and $HeI\lambda5876$, whose observed intensities are not strong enough to cover up underlying absorptions of the continuum. So, whatever the velocity structure, the optically thick emission regions can only screen a small fraction of the stellar surface at each v_{obs}. The other is based on the need to reduce the model intensities of all the H and HeI lines, calculated assuming a smooth flow with physical conditions suitable to produce the line ratios, in order to match the observed values.

With regard to the accelerating and then decelerating wind advocated by Mitskevich et al. (1993), we have several reservations for its general applicability to CTTSs. First, the $Pa\beta$ and $Pa\gamma$ lines are also quite optically thick ($\tau_{Pa\gamma} > 20$, cf. Fig. 11) but, unlike $H\alpha$, they rarely show a blue absorption. Second, the maximum blue velocity seen in $HeI\lambda10830$ or $Pa\gamma$ is often $\geq 350\ km\ s^{-1}$ (EFHK06). If this is reached at $3R_*$, the locale adopted by Mitskevich et al. (1993), the gravitational pull of a CTTS of 1 $M_\odot$ and $2R_\odot$ will only decelerate it to 240 $km\ s^{-1}$, not low enough to explain most of the $H\alpha$ blue absorptions, whose maximum depths usually occur at $v_{obs} > -100\ km\ s^{-1}$ (cf. Fig. 15 of BEK01). We think that the $H\alpha$ blue absorptions, other than the broad ones that originate in a radial wind, are caused by disk winds lying beyond the hydrogen emission zone. They are fairly sharp and narrow, similar to those produced by a disk wind scattering the stellar continuum (Kwan et al. 2007). However, because the hydrogen emission zone is more extensive than the stellar surface, a revised modelling is needed to ascertain the absorption profile.

One possible mechanism for accelerating the gas and initiating a clumpy flow is the occurrence of multiple coronal mass ejections. These ejections will have to be much more energetic than those in the solar corona and occur at a much higher frequency, since the wind density needs to be $\geq 5 \times 10^8\ cm^{-3}$ to produce a $\tau_{HeI\lambda10830}$ of ≥ 1, thereby implicating

a minimum mass loss rate of $\sim 0.5 \times 10^{-9} \ M_\odot \ yr^{-1}$. The clumpy gas distribution can arise from the initial multiple ejection centers and the shocked regions produced when the different ejectas intersect.

There can be several sources for the photons needed for helium ionization. One, known already, is the shocked region at the footpoint of the accretion stream. For an impact velocity of 300 $km \ s^{-1}$, the temperature in the post-shock region reaches $10^6 \ K$. Cooling by free free emission will produce many photons more energetic than 24.6 eV. A fraction of this radiative luminosity will propagate towards the star and be re-processed into optical and UV continuum seen as veiling, but a fraction will propagate away from the star and may even escape absorption by the infalling flow if the gases fill only partially the overall accretion envelope (Fischer et al. 2008). For an accretion rate of $3 \times 10^{-9} \ M_\odot \ yr^{-1}$, if 1% of the radiative luminosity generated escape, the luminosity in photons with energies $\geq$ 24.6 eV will be $\sim 10^{-4} L_\odot$. Ionizing photons can also originate from the wind region, e.g., at the sites of coronal mass ejections and the filaments formed by intersecting ejectas, likely with comparable luminosities. As mentioned before, however, the issue with ionizing photons is not so much the availability of sources, but more the propagation distance from a given source. Both a clumpy accretion flow and a clumpy wind help to increase the propagation length, but a definitive understanding will probably need Monte Carlo simulation of the propagation of photons with energies both near and far away from ionization thresholds, and of photons produced from subsequent recombinations to the ground state, as well as consideration of multiple ionizations when the ejected electron has an energy exceeding the HI ionization threshold.

We have identified the disk/magnetosphere interface where accreting gases dissipate part of their rotational energies before falling along stellar field lines as a source of energy for both the veiling continuum near $1\mu m$ and the $CaII$ line emission, and there appears to be a correlation between r_Y and the strength of the $CaII$ infrared triplet (Fischer et al. 2010). The correlation of strong HeI line emission and strong $CaII$ line emission is probably a consequence of the correlation between HeI emission and r_Y. BEK01 noted that when $HeI\lambda5876$ has a signature indicative of a wind origin the NC is comparatively weak and may be even absent, and suggested a scenerio in which high accretion rates or weak stellar fields may cause the magnetosphere to be crushed sufficiently that the disk extends almost to the star, so impact velocities of the accreting matter will be smaller and less energy will be available for the NC emission. At the same time a larger fraction of the rotational energy of the accreting matter needs to be dissipated, possibly leading to a larger r_Y. Also, the equatorial region of the star will be preferentially torqued, and the resulting differential rotation with latitude may induce stronger magnetic activities for field lines anchored at the polar region and produce a greater mass ejection, leading to stronger HeI line emission.

The minimum coronal density we derive is $\sim 5 \times 10^8$ cm^{-3}, and the corresponding mass loss rate is $\sim 0.5 \times 10^{-9}$ $M_\odot$ yr^{-1} in order to produce a $\tau_{HeI\lambda10830}$ of 1. The density and mass loss rate probably span a factor of ≥ 10 in range. They are germane to the investigation of the role of a stellar wind on the angular momentum evolution of a CTTS (Matt & Pudritz 2005) and the numerical simulation of magnetospheric accretion of matter in various field geometries (Romanova et al. 2009).

We have applied our model calculations to CTTSs because of their extensive information on line fluxes and profiles. These results on line optical depths, line emissivity ratios, and specific line emissivities from local excitation calculations are usable for the broad lines of other pre-main-sequence stars because the individual star affects the calculations only through its stellar and veiling continua. For H, HeI, and OI excitations, the effects of these continua via photoionization of and stimulated absorption by excited states are not significant. The effects on photoionizing $CaII$ and NaI are stronger. They can be gauged from comparing Figures 6 & 7, which show results for the locations of 4 and $2.5R_*$ respectively. The $CaII$ and NaI line optical depths in the $r = 2.5R_*$ calculation are affected by a smaller $2r/v$ factor in the τ expression and a larger photoionization rate by a factor of 2.56 (cf. §5.1). Together the two factors affect little the $\tau_{CaII\lambda8498}$ contour, but produce a displacement of the $\tau_{NaI\lambda5892}$ contour by a factor of ~ 2 or less.

10. Conclusion

We first summarize the main results of this work and then comment on future studies that may shed further light on the formation and origins of the line emission in CTTSs. Our primary conclusions are:

1. UV photoionization is needed to produce the $HeI\lambda10830$ opacities in both the accretion flow and radial wind that generate the observed red and broad blue absorptions respectively. It is also the most probable excitation mechanism responsible for the narrow, sharp blue absorptions and the central absorptions.

2. The strong HeI and H line emission originate primarily in a radial outflow that is highly clumpy. The bulk of the wind volume is filled by gas at a density $\sim 10^9$ cm^{-3} and optically thick to $HeI\lambda10830$ and $H\alpha$, but optically thin to $HeI\lambda5876$, $Pa\gamma$, and the $CaII$ infrared triplet. The optically thick $HeI\lambda5876$ emission occur mostly in regions of density $\geq 10^{11}$ cm^{-3} and temperature $\geq 1.5 \times 10^4$ K, while the optically thick $H\alpha$ and $Pa\gamma$ emission occur mostly in regions of density around 10^{11} cm^{-3} and temperature between 8750 and 1.25×10^4 K. In producing the observed line flux at a given v_{obs} the area covering

factor of these emission clumps is sufficiently small to not incur significant absorption of the stellar and veiling continua in either HeI and H lines. HeI emission, possibly strong, may occasionally arise from the accretion flow close to the impact shock as a result of photoionization heating by the UV photons.

3. The strong $CaII$ line emission likely arise in both the magnetospheric accretion flow and the disk boundary layer where the gases dissipate part of their rotational energies before infalling along magnetic field lines. The needed density and temperature are $\sim 10^{12}~cm^{-3}$ and $\leq 7500~K$ respectively. Weak $CaII$ line emission, on the other hand, can come from the clumps producing the H emission in the wind.

We plan to follow up this work by presenting all the optical and $1\mu m$ spectral data procured simultaneously or near-simultaneously (Edwards et al. 2010), with an aim to provide more comparisons with model results on the ratios and specific fluxes of not only lines alluded to here but also others, such as $H\beta$, $H\gamma$, $HeI\lambda 6678$, that are useful as consistency checks. The larger sample will also convey information on the ranges of variation in the line properties and related physical conditions. It will also apprise of possible correlations among continuum veilings, line ratios, and line fluxes that may elucidate the relationship between accretion and stellar wind activities.

A future project that will be enlightening is time monitoring at optical and $1\mu m$ spectral regions simultaneously over more than a rotational period for several CTTSs. The simultaneous coverage of both spectral regions is needed to include $HeI\lambda 10830$, the key indicator of intervening kinematic structures through its absorption features, and the many optical lines whose strengths and profiles delimit the requisite physical conditions. The time sequence data can test the often presumption of azimuthal symmetry for either the accretion flow or radial wind and its physical conditions, and provide detailed information for a realistic modelling of both the accretion flow and radial wind geometric structures.

Further understanding of the origins and formation of spectral lines can be gained from studying the highly ionized lines, notably $CIV\lambda 1549$, and optical as well as UV $FeII$ and FeI lines. There are two potential sites for the highly ionized lines, the stellar wind region and the part of the accretion flow close to the impact shock. It is important to determine their origin, through analysis of their profiles and excitations, and check for consistency/conflict with the formation and origin of the HeI lines. $FeII$ and FeI emission can be significant from both the H and $CaII$ emission regions. Their strengths and profiles, in comparison with those of H and $CaII$ lines, as well as the similarities/contrasts between $FeII$ and FeI lines, can provide additional information on the excitation conditions in those regions.

Eventually confirmation of a clumpy stellar wind requires an understanding of the energy

generation and acceleration process. It also needs numerical simulation of the ejectas and gas flows to check if the resulting density, temperature, and velocity distributions are consistent with those inferred from the line emission strengths and profiles.

In conclusion, the frequent presence in $HeI\lambda10830$ of absorption features indicative of a radial flow, and our deduction of strong line emission from this flow, if correct, indicate that a significant stellar wind, in terms of mass loss and energy output rates, is an essential component of the star formation process. It is clearly in response to the active accretion of matter onto the star. This dynamic action-reaction between accretion disk and star may ultimately determine the mass and angular momentum of the emerging star.

A.   Atomic Parameters

A.1.   HI

We obtain the rate coefficients for collisional transitions between HI levels from Anderson et al. (2002). Unfortunately they have included only levels $n = 1 - 5$. The $\Delta n = 1$ transitions have the largest rates and we fit their collisional rate coefficients, i.e. $C_{n+1,n}$, $1 \le n \le 4$, with the expression $C_{n+1,n} = C_{3,2}(n/2)^{\kappa}exp(\chi[ln(n/2)]^2)$, where κ and χ are the fit parameters, and extrapolate to $5 \le n \le 14$. To check the accuracy of the extrapolated rate coefficients, we compare them to those obtained from the formulas given in Johnson (1972). The differences are $\sim 30\%$, comparable to those for $n \le 4$. The $\Delta n = 2$ collisional rate coefficients are the next strongest and, for the same lower level, are a factor of ~ 2.5 or more smaller than the $\Delta n = 1$ ones, i.e. $C_{n+2,n}/C_{n+1,n} \le 1/2.5$. They are quite different from Johnson's values, being larger by a factor of between 1.2 and 1.8 at $T = 10^4$ K. We fit them, i.e. $C_{n+2,n}$, $1 \le n \le 3$, with the simple power-law expression $C_{n+2,n} = C_{4,2}(n/2)^{\delta}$, where δ is the fit parameter, and the proviso that the extrapolated $C_{n+2,n}$ for $4 \le n \le 13$ is no more than a factor of ~ 2 larger than Johnson's corresponding rate coefficient. The $\Delta n = 3$ collisional rate coefficients are a factor of ~ 2.3 or more smaller than the $\Delta n = 2$ ones, i.e. $C_{n+3,n}/C_{n+2,n} \le 1/2.3$, $1 \le n \le 2$. They are larger than Johnson's values by a factor of ~ 2.2 at $T = 10^4$ K, so we again extrapolate them to higher values of n with a power-law fit, i.e. $C_{n+3,n} = C_{5,2}(n/2)^{\epsilon}$, and the proviso that the extrapolated rate coefficients are no more than a factor of ~ 2.5 larger than Johnson's. For level $n = 6$ only, the upper state of the

$Pa\gamma$ transition, we also extrapolate the rate coefficients of Anderson et al. (2002) to obtain $C_{6,1}$ and $C_{6,2}$. We fit $C_{n,1}$, $2 \leq n \leq 5$, with the expression $C_{n,1} = C_{2,1}[1/(n-1)]^\zeta$, and $C_{n,2}$, $3 \leq n \leq 5$, with the expression $C_{n,2} = C_{3,2}[1/(n-2)]^\eta$, and extrapolate to $n = 6$. It turns out that in the regions responsible for the observed emission the electron densities are quite high, $\geq 3 \times 10^{10}$ cm^{-3}, so collisions dominate the population exchange among the higher energy levels. The level population then depend mostly on the scaling of the collisional rate coefficients with n, which we hope to capture with our fitting procedure.

We calculate the rate coefficients for collisional ionization from the formulas given in Johnson (1972) and determine the three-body recombination coefficients by detailed balance. In addition to UV photoionization of the ground state, we include photoionizations of the $n = 2 - 4$ levels by the stellar and veiling continua. The photoionization cross-sections are gathered from Allen (1973) and the radiative recombination coefficients to the 15 levels from Seaton (1959). We also include radiative absorptions of the stellar and veiling continua at all permitted line transitions except the Lyman ones. In principle, the probability of stimulated absorption is the same as the escape probability calculated with the velocity gradient along the trajectory of the incident continuum photon. It is therefore different from the escape probability of a photon emitted by spontaneous emission, in general. We will ignore this distinction here, since it does not affect the order of the lines in their opacity magnitudes.

A.2.   HeI

We adopt the helium atomic parameters and many of the collision strengths from the Chianti data base (Young et al. 2003) which lists energy levels, Einstein A rates, and collision strengths for transitions involving one of the four lowest energy states. For the rest of the collision strengths, we obtain them from Sawey and Berrington (1993), the basis of Chianti's compilation. We determine the collisional ionization rate coefficient of the ground state from the cross-sections measured by Montague, Harrison, & Smith (1984), and that of the $2s$ ^3S level from the theoretical calculation of cross-sections by Taylor, Kingston, & Bell (1979), and gather the rest from the compilation of Benjamin, Skillman, & Smits (1999). We obtain the $2s$ ^3S and $2s$ ^1S photoionization cross-sections from Fernley, Taylor, & Seaton (1987), and the radiative recombination rate coefficients from Benjamin et al. (1999).

The absence of collision strengths involving $n \geq 5$ levels is the reason why our helium model atom has only 19 levels. There is the concern that, like the case of hydrogen, collisional excitation from the 19 levels to higher ones will likely lead to ionization, so limiting helium to 19 levels will underestimate the helium ionization rate and overestimate the helium level population. This problem may be somewhat less severe for helium because the separations

in energy of the angular momentum states with the same energy quantum number n lead to more radiative decay channels, and the ionization of hydrogen by $\lambda584$ photons provides a steady drainage of the $2p$ ^1P population. Both features tend to dampen the rapid build up of population into levels of higher n as the collisional excitations and line opacities increase with increasing density. From the results of the calculations we find that under the physical conditions responsible for the $\lambda5876$ emission the 8 $n = 4$ levels account for less than 20% of the total helium ionization rate. Hopefully the errors in helium line fluxes and line ratios are within 20%.

A.3.   OI, CaII, NaI

We obtain most of the Einstein A rates of the pertinent OI transitions from Hibbert et al. (1991), Biémont & Zeippen (1992), and Carlsson & Judge (1993). The $\lambda11287$ Einstein A rate of 1.1×10^7 s^{-1} is deduced from the experimental work of Christensen & Cunningham (1978). The $3s$ ^3S level has also a radiative decay route to the $2p^4$ ^1D state that is not indicated in Figure 3. Its Einstein A rate of 1.83×10^3 s^{-1} (Biémont & Zeippen 1992) is included as an additional decay rate of $3s$ ^3S to the ground level. We gather the collisional rate coefficients for the various transitions from Barklem (2007), the radiative recombination rate coefficients from Péquignot, Petitjean, & Boisson (1991), and the $OI - HII$ and $OII - HI$ charge-exchange reaction rates from Field & Steigman (1971).

We obtain the Einstein A rates and collisional rate coefficients for all relevant $CaII$ transitions from Burgess, Chidichimo, & Tully (1995), the photoionization cross-sections from Verner et al. (1996), and Shine & Linsky (1974), the collisional ionization rate coefficients from Arnaud & Rothenflug (1985), and Shine & Linsky (1974), the total radiative recombination rate coefficient from Shull & Van Steenberg (1982), and the direct radiative recombination rate coefficients to the three levels from their photoionization cross-sections through detailed balance.

For the relevant atomic parameters of NaI, we obtain the Einstein A rate from Sansonetti (2008), the $3s$ ^2S and $3p$ ^2P photoionization cross-sections from the experimental work of Hudson & Carter (1967) and Rothe (1969) respectively, the $3s$ ^2S collisional ionization rate coefficient from Arnaud & Rothenflug (1985), the $3s$ $^2S \to 3p$ ^2P collisional excitation rate coefficient from Clark et al. (1982), and the radiative recombination rate coefficient from Verner & Ferland (1996).

REFERENCES

Allen, C. W. 1973, Astrophysical Quantities (London: Athlone)

Anderson, H., Ballance, C.P., Badnell, N.R., & Summers, H. P. 2002, J. Phys. B, 35, 1613

Appenzeller, I., & Wolf, B. 1977, A&A, 54, 713

Arnaud, M., & Rothenflug, R. 1985, A&AS, 60, 425

Barklem, P. S. 2007, A&A, 462, 781

Bary, J. S., Matt, S. P., Skrutskie, M. F., Wilson, J. C., Peterson, D. E., & Nelson, M. J. 2008, ApJ, 687, 376

Benjamin, R. A., Skillman, E. D., & Smits, D. P. 1999, ApJ, 514, 307

Beristain, G., Edwards, S., & Kwan, J. 2001, ApJ, 551, 1037 (BEK01)

Biémont, E., & Zeippen, C. J. 1992, A&A, 265, 850

Bowen, I. S. 1947, PASP, 59, 196

Burgess, A., Chidichimo, M. C., & Tully, J. A. 1995, A&A, 300, 627

Calvet, N., & Gullbring, E. 1998, ApJ, 509, 802

Carlsson, M., & Judge, P. G. 1993, ApJ, 402, 344

Christensen, A. B., & Cunningham, A. J. 1978, J. Geophys. Res., 83, 4393

Clark, R. E. H., MaGee, N. H. Jr., Mann, J. B., & Merts, A. L. 1982, ApJ, 254, 412

Edwards, S., Fischer, W., Hillenbrand, L., & Kwan, J. 2006, ApJ, 646, 319 (EFHK06)

Edwards, S., Fischer, W., Hillenbrand, L., & Kwan, J. 2010 (in preparation)

Edwards, S., Hartigan, P., Ghandour, L., & Andrulis, C. 1994, AJ, 108, 1056

Fernley, J. A., Taylor, K. T., & Seaton, M. J. 1987, J. Phys. B, 20, 6457

Field, G. B., & Steigman, G. 1971, ApJ, 166, 59

Fischer, W., Edwards, S., Hillenbrand, L., & Kwan, J. 2010 (in preparation)

Fischer, W., Kwan, J., Edwards, S., & Hillenbrand, L. 2008, ApJ, 687, 1117

Folha, D. F. M., & Emerson, J. P. 2001, A&A, 365, 90

Hartmann, L., Calvet, N., Avrett, E. H., & Loeser, R. 1990, ApJ, 349, 168

Hibbert, A., Biémont, E., Godefroid, M., & Vaeck, N. 1991, J. Phys. B., 24, 3943

Hirth, G., Mundt, R., & Solf, J. 1994, A&A, 285, 929

Hudson, R. D., & Carter, V. L. 1967, J. Opt. Soc. Am., 57, 651

Johns-Krull, C. M. 2007, ApJ, 664, 975

Johnson, L. C. 1972, ApJ, 174, 227

Königl, A., & Pudritz, R. E. 2000, in Protostars and Planets IV, ed. V. Mannings, A. P. Boss, & S. S. Russell (Tucson: Univ. Arizona Press), 759

Kurosawa, R., Romanova, M. M., & Harries, T. J. 2008, MNRAS, 385, 1931

Kwan, J. 1997, ApJ, 489, 284

Kwan, J., Edwards, S., & Fischer, W. 2007, ApJ, 657, 897

Kwan, J., & Tademaru, E. 1988, ApJ, 332, L41

Lodders, K. 2003, ApJ, 591, 1220

Martin, S. C. 1996, ApJ, 470, 537

Matt, S., & Pudritz, R. 2005, ApJ, 632, L135

Mitskevich, A. S., Natta, A., & Grinin, V. P. 1993, ApJ, 404, 751

Mohanty, S., & Shu, F. 2008, ApJ, 687, 1323

Montague, R. G., Harrison, M. F. A., & Smith, A. C. H. 1984, J. Phys. B., 17, 3295

Muzerolle, J., Calvet, N., & Hartmann, L. 1998a, ApJ, 492, 743

Muzerolle, J., Calvet, N., & Hartmann, L. 2001, ApJ, 550, 944

Muzerolle, J., Calvet, N., Hartmann, L., & D'Alessio, P. 2003, ApJ, 597, L149

Muzerolle, J., Hartmann, L., & Calvet, N. 1998b, AJ, 116, 455

Natta, A., Giovanardi, C., & Palla, F. 1988, ApJ, 332, 921

Péquignot, D., Petitjean, P., & Boisson, C. 1991, A&A, 251, 680

Romanova, M. M., Long, M., Kulkarni, A. K., Kurosawa, R., Ustyugova, G. V., Koldoba, A. V., & Lovelace, R. V. E. 2007, Proceedings IAU Symp. No. 243, 277

Romanova, M. M., Ustyugova, G. V., Koldoba, A. V., & Lovelace, R. V. E. 2009, MNRAS, 399, 1802

Rothe, D. E. 1969, J. Quant. Spectrosc. Radiat. Transfer, 9, 49

Sansonetti, J. E. 2008, J. Phys. Chem. Ref. Data, 37, 1659

Sawey, P. M. J., & Berrington, K. A. 1993, At. Data Nucl. Data Tables, 55, 81

Seaton, M. J. 1959, MNRAS, 119, 81

Shine, R. A., & Linsky, J. L. 1974, Solar Phys. 39, 49

Shull, J. M., & Van Steenberg, M. 1982, ApJS, 48, 95

Sobolev, V. V. 1960, Moving Envelopes of Stars (Cambridge: Harvard Univ. Press)

Taylor, I. R., Kingston, A. E., & Bell, K. L. 1979, J. Phys. B, 12, 3093

Verner, D. A., & Ferland, G. J. 1996, ApJS, 103, 467

Verner, D. A., Ferland, G. J., Korista, K. T., & Yakovlev, D. G. 1996, ApJ, 465, 487

Young, P. R., Zanna, G. D., Landi, E., Dere, K. P., Mason, H. E., & Landini, M. 2003, ApJS, 144, 135

Table 1.   Line Types and Designated Temperatures

Line Type	$T(10^4\ K)$	Figures
short dash-long dash	0.5	5,8,9,10,11,12,15,16, , , 19,20,21,22,23,24
short dash	0.75	5,8,9,10,11,12,15,16,17,18,19,20,21,22,23,24
long dash	0.875	5,8,9, ,11,12,15,16,17,18,19,20,21,22,23, 24
solid	1.0	5,8,9,10,11,12,15,16,17,18,19,20,21,22,23,24
dotted	1.5	5,8,9,10,11,12,15,16,17,18,19,20,21,22,23,24
dot-short dash	2.0	5,8,9,10,11,12,15,16,17,18,19,20,21,22,23,24
dot-long dash	1.25	5,8,9,10, , , , , , , , , ,22,23,
	3.0	, , , ,11, , , , , ,19,20,21, , ,
	0.625	, , , , , ,15,16,17,18, , , , , ,24
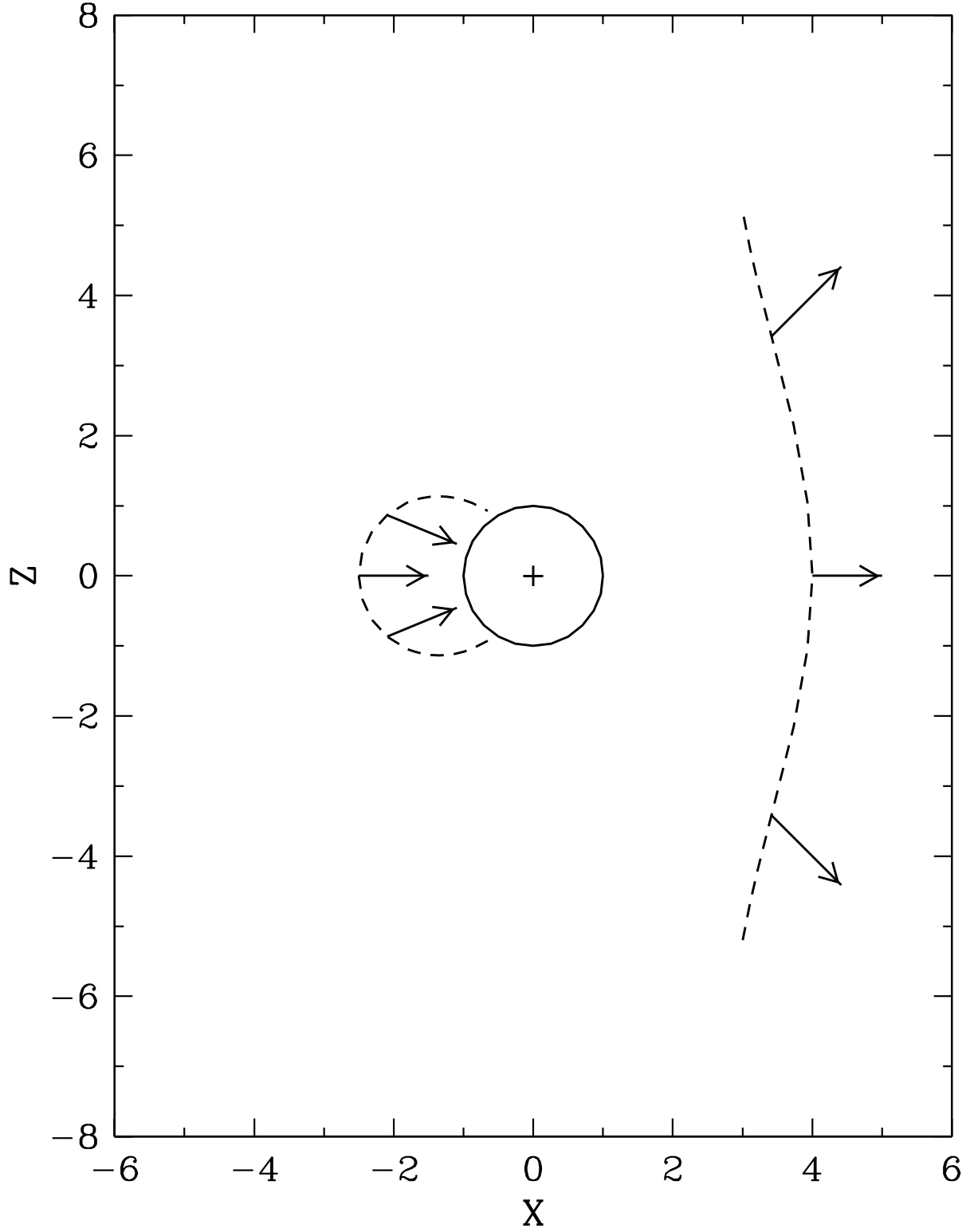
Fig. 1.— Contour of $v_{obs} = -150\ km\ s^{-1}$ for a spherical wind (right side) reaching $150\ km\ s^{-1}$ at $4R_*$ and radial infall (left side) reaching $150\ km\ s^{-1}$ at $2.5R_*$, for a viewer at $x \to \infty$. The contour gives rise to a projected area of $27\pi R_*^2$ and $1.286\pi R_*^2$ for the wind and infall flow respectively.
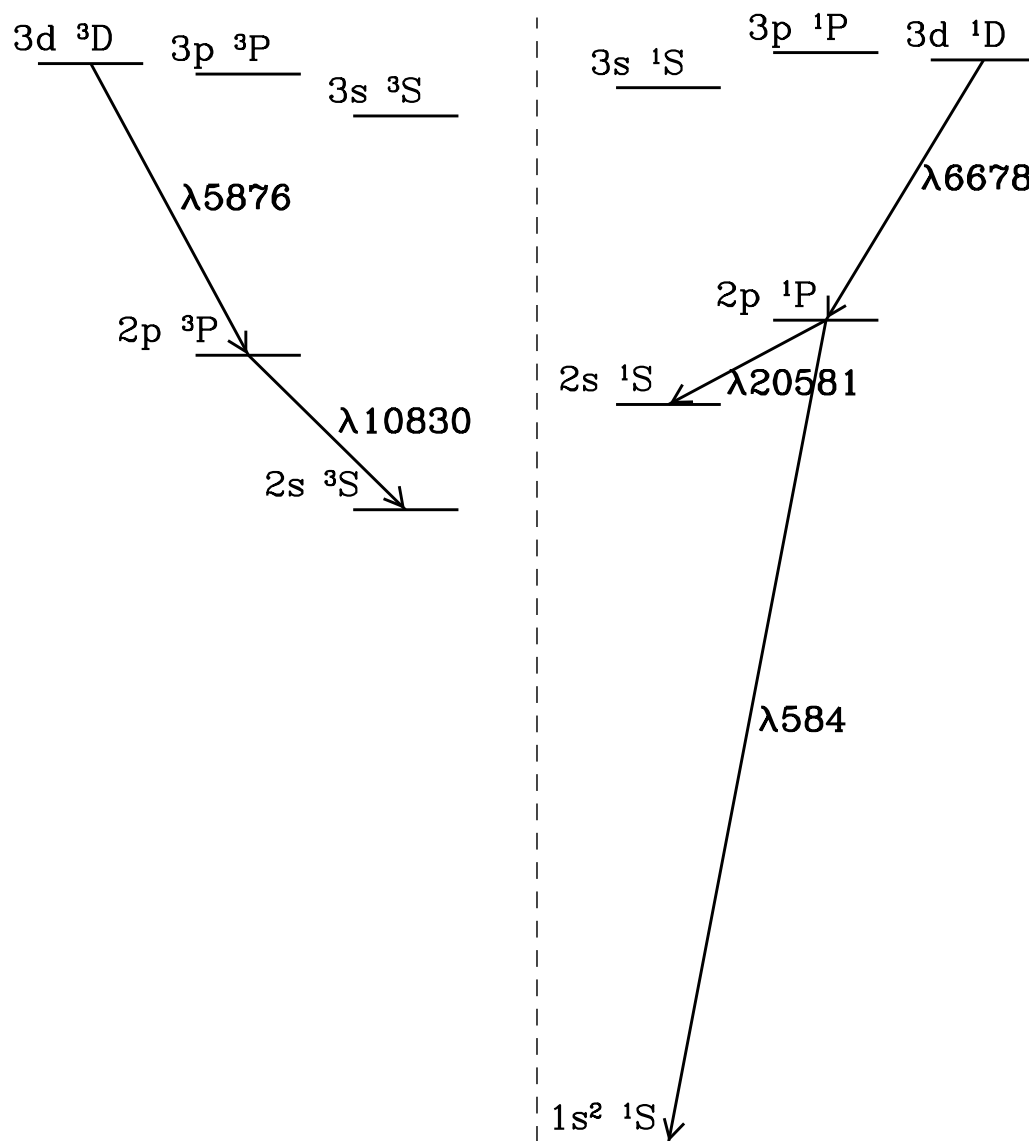
Fig. 2.— Energy level diagram of HeI, not drawn to scale.
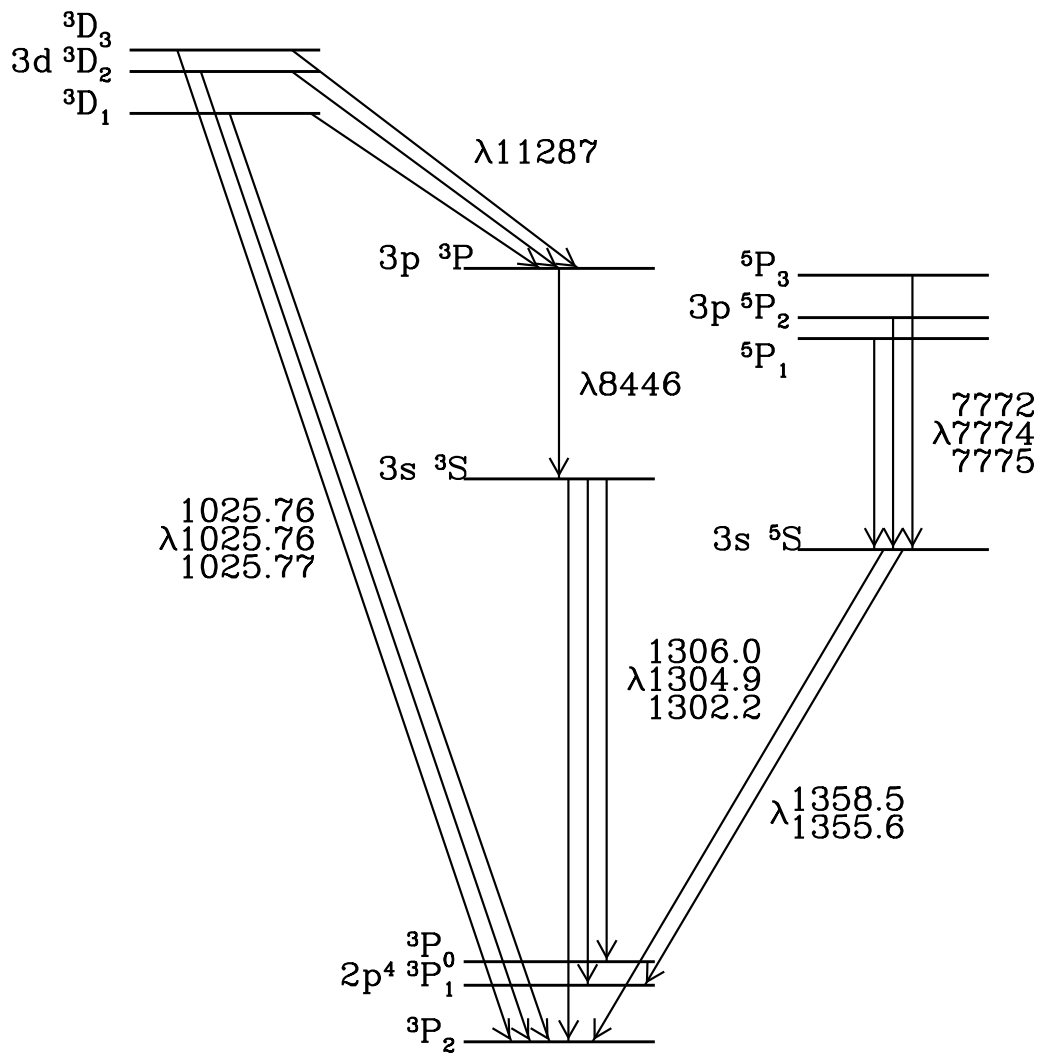
Fig. 3.— Energy level diagram of OI, not drawn to scale.
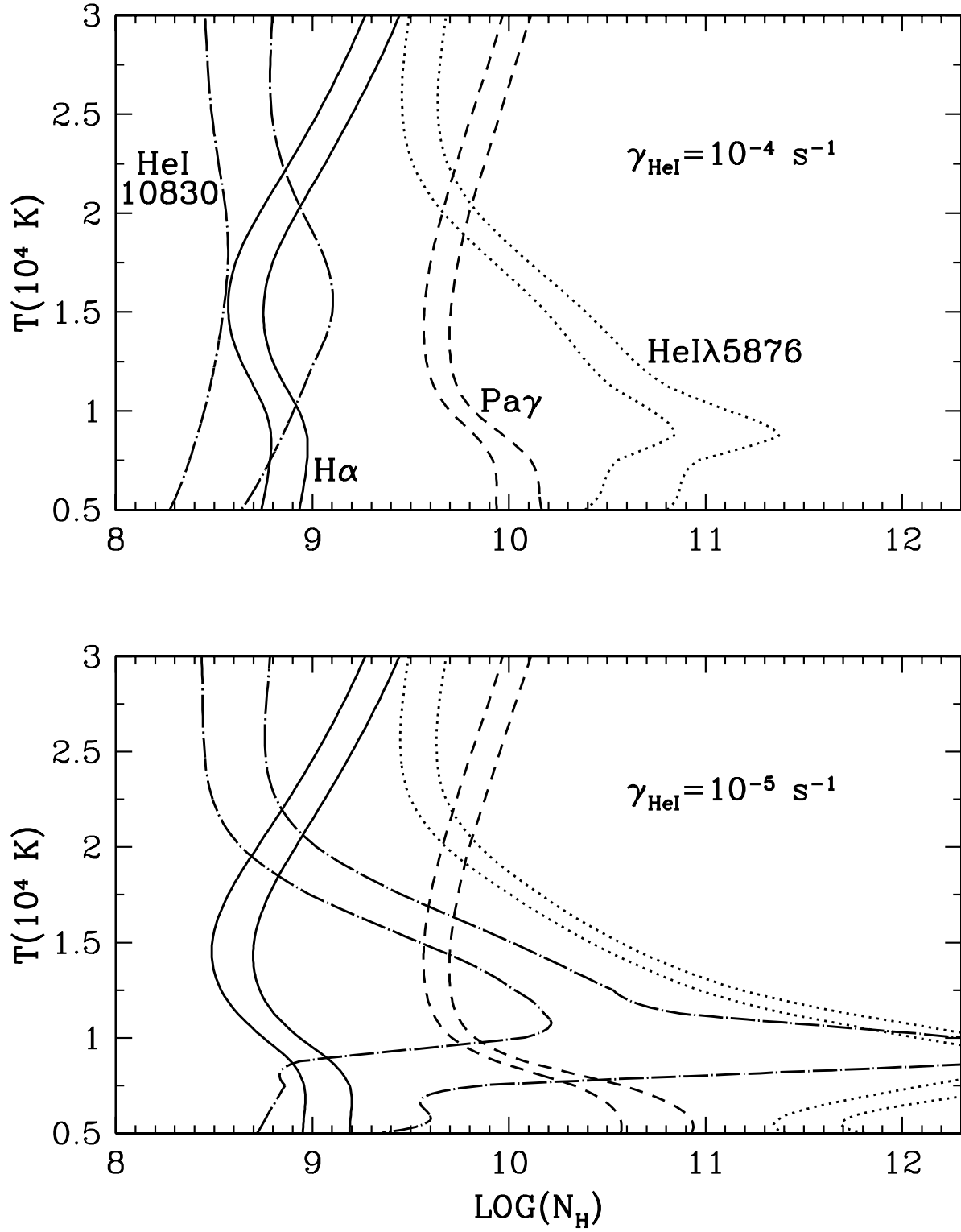
Fig. 4.— Contour plots of line optical depths for $r = 4R_*$ and $\gamma_{HeI} = 10^{-4}$ (top panel) and 10^{-5} s^{-1} (bottom panel). $HeI\lambda10830$ and $H\alpha$ have $\tau = 1$ and 3.16 contours, and $HeI\lambda5876$ and $Pa\gamma$ have $\tau = 0.1$ and 0.316 contours.
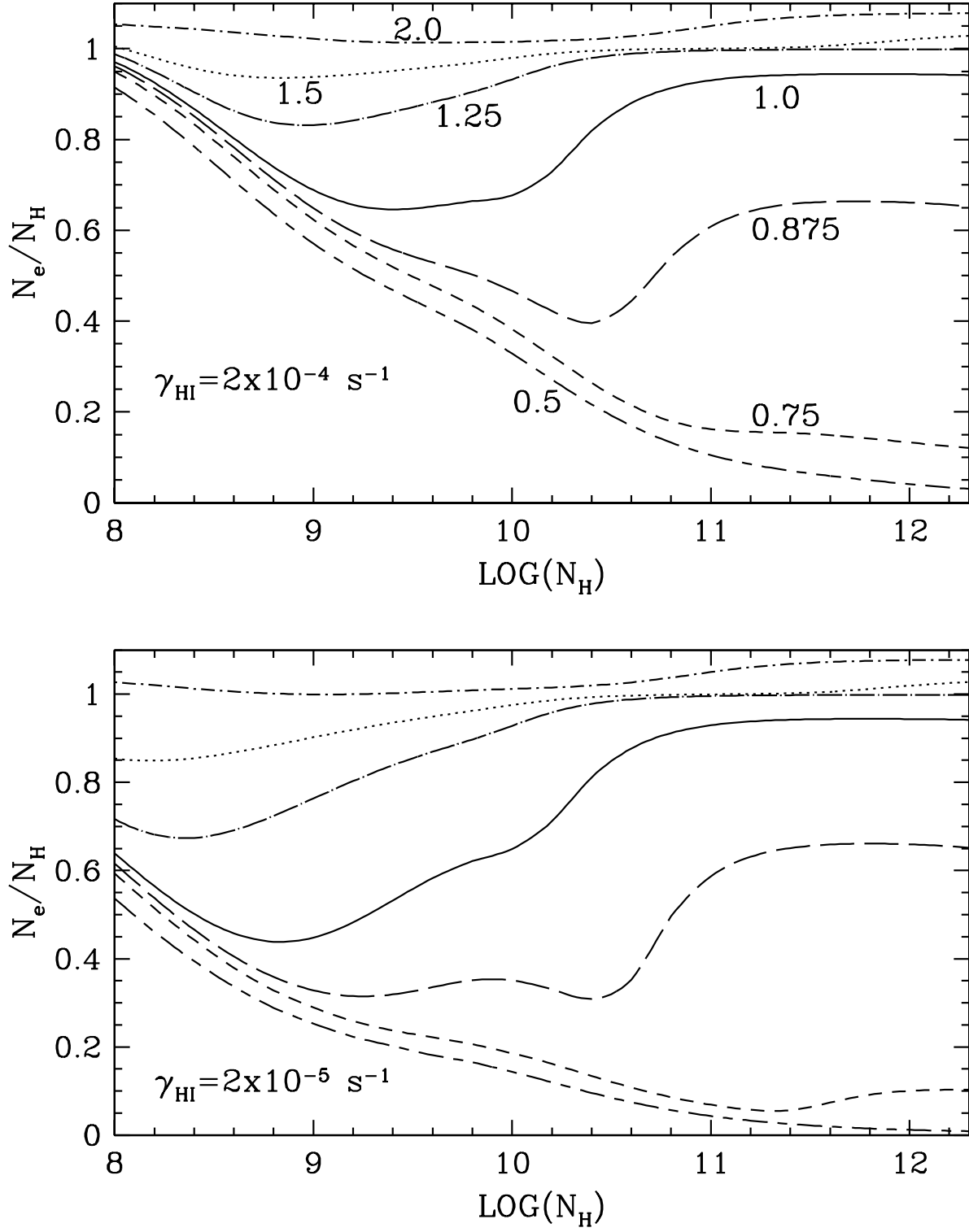
Fig. 5.— Dependence of electron fraction N_e/N_H on N_H for $r = 4R_*$, $\gamma_{HI} = 2 \times 10^{-4}$ (top panel) and 2×10^{-5} s^{-1} (bottom panel), and seven temperatures (in unit of 10^4 K).
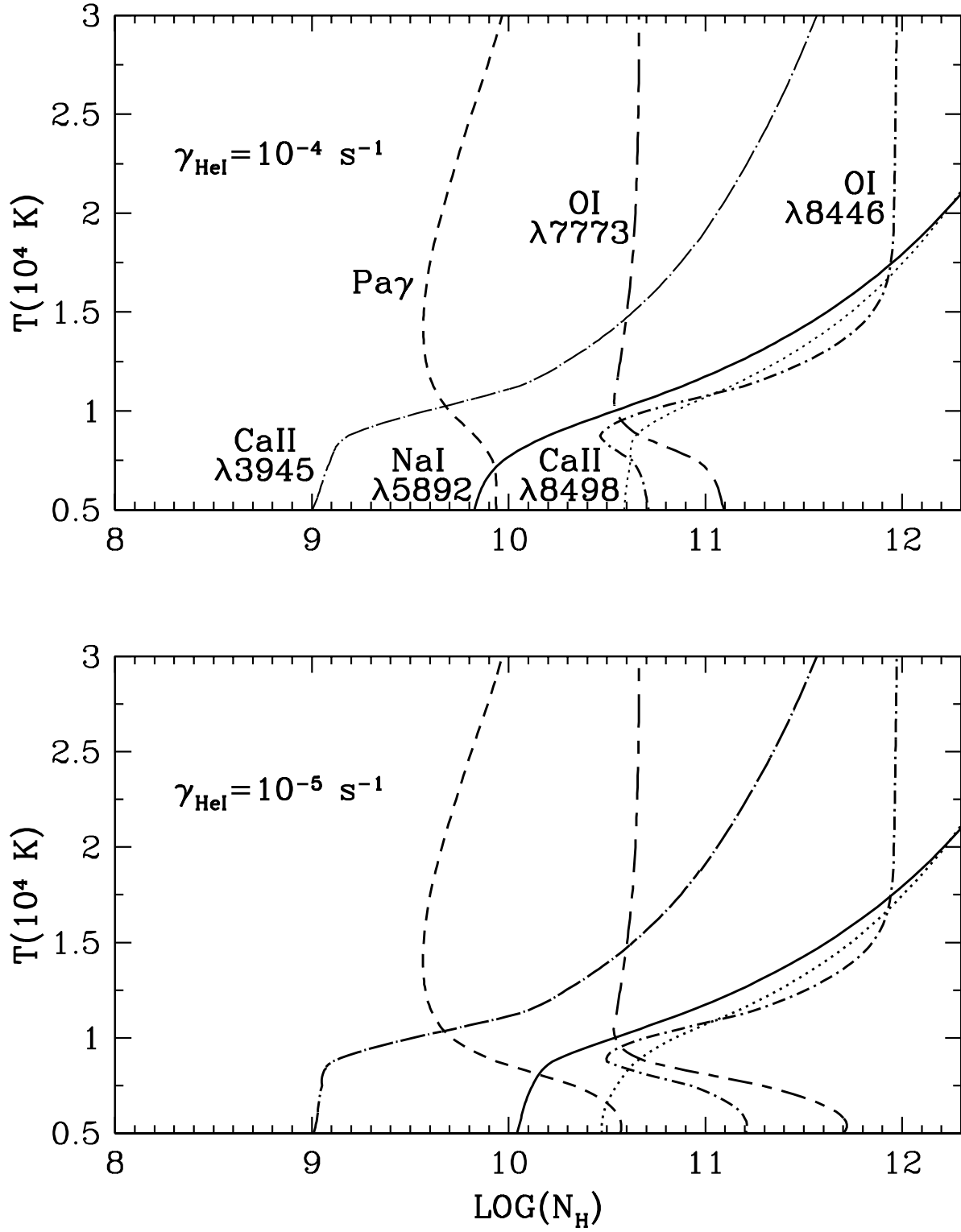
Fig. 6.— Contour plots of line optical depths for $r = 4R_*$ and $\gamma_{HeI} = 10^{-4}$ (top panel) and 10^{-5} s^{-1} (bottom panel). $CaII\lambda\lambda3945, 8498$, and $NaI\lambda5892$ have $\tau = 1$ contours, and $Pa\gamma$, $OI\lambda\lambda8446, 7773$ have $\tau = 0.1$ contours.
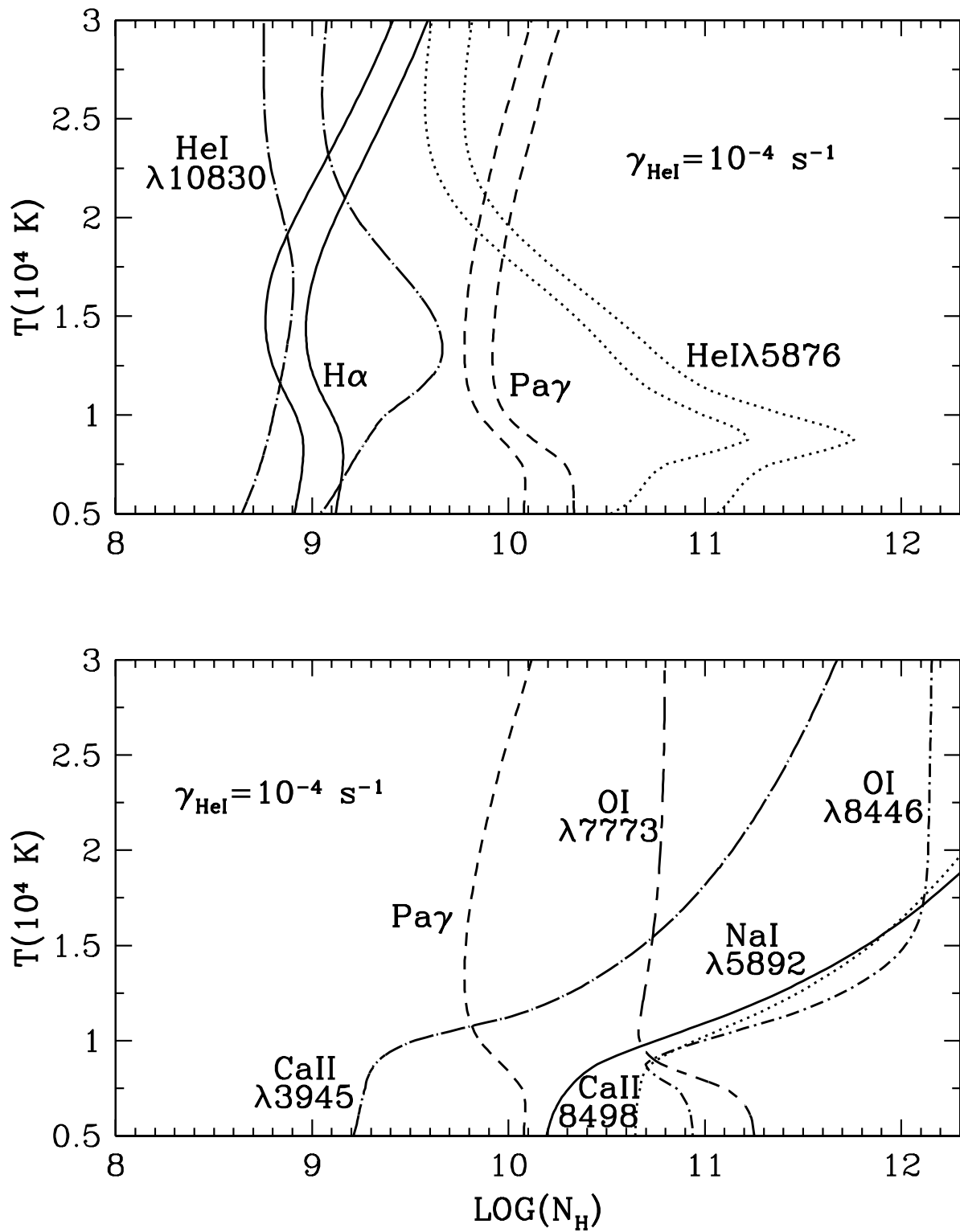
Fig. 7.— Top panel same as top panel of Fig. 4 and bottom panel same as top panel of Fig. 6 but for $r = 2.5R_*$.
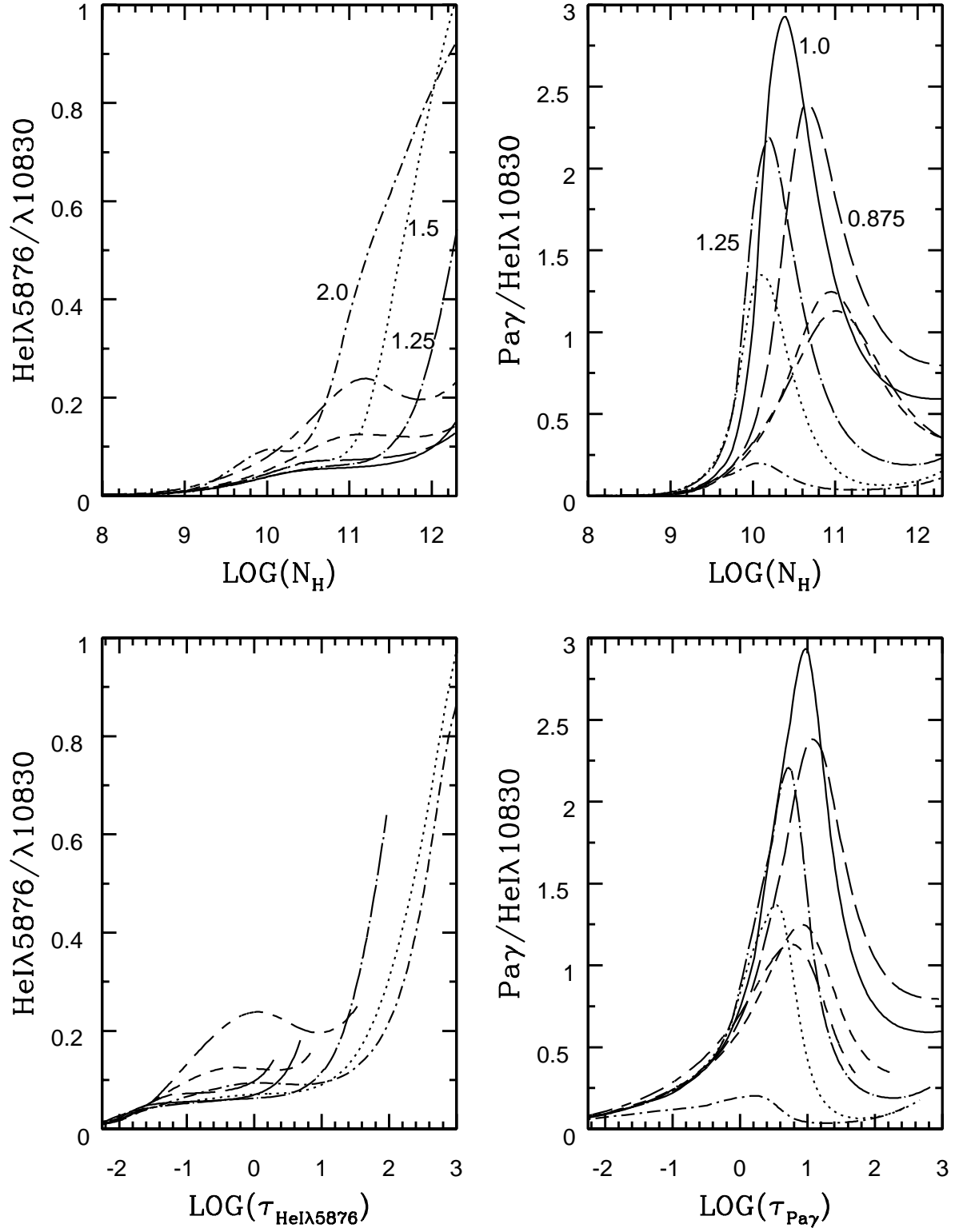
Fig. 8.— Dependences of $HeI\lambda5876/\lambda10830$ and $Pa\gamma/HeI\lambda10830$ on density and line optical depth for $r = 4R_*$, $\gamma_{HeI} = 10^{-4}\ s^{-1}$, and various temperatures. See Table 1 for the designations between line types and temperatures.
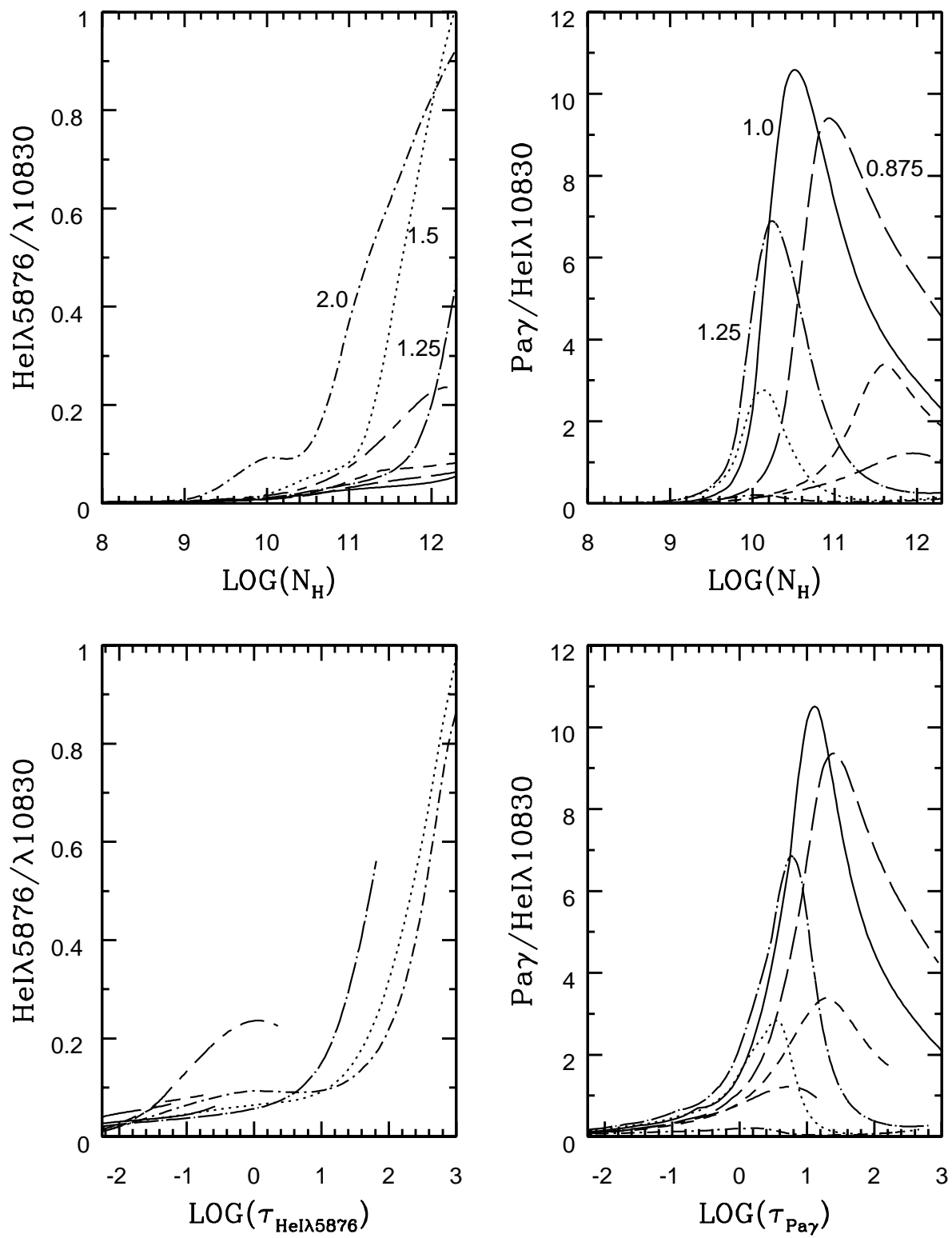
Fig. 9.— Same as Fig. 8 but for $\gamma_{HeI} = 10^{-5}\ s^{-1}$.
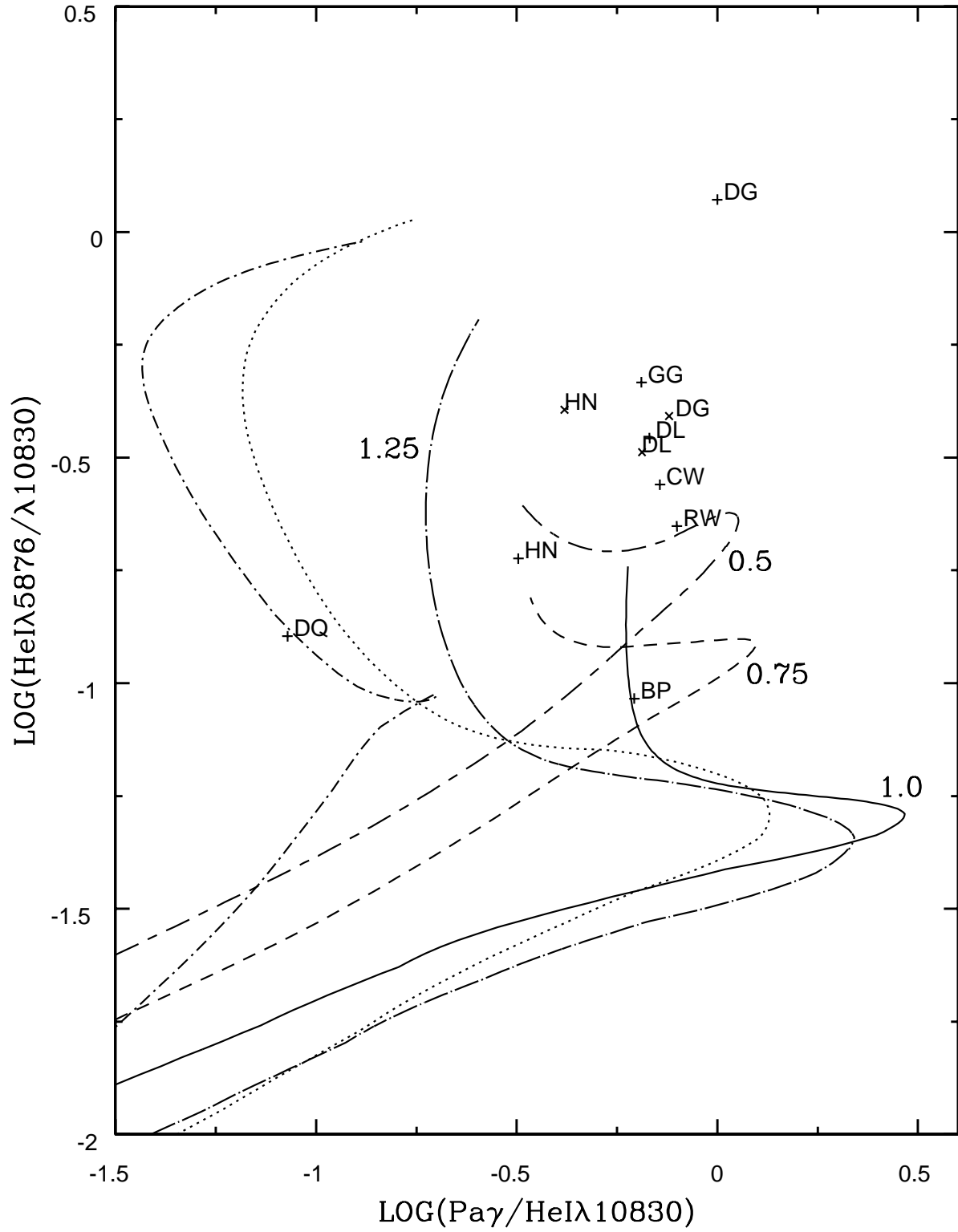
Fig. 10.— Plot of $\log(HeI\lambda5876/\lambda10830)$ versus $\log(Pa\gamma/HeI\lambda10830)$ for $r = 4R_*$, $\gamma_{HeI} = 10^{-4}\ s^{-1}$, and various temperatures(cf. Table 1). Data points marked by +s are determined from BEK01 and EFHK06. Those marked by xs are from Edwards et al. (2010).
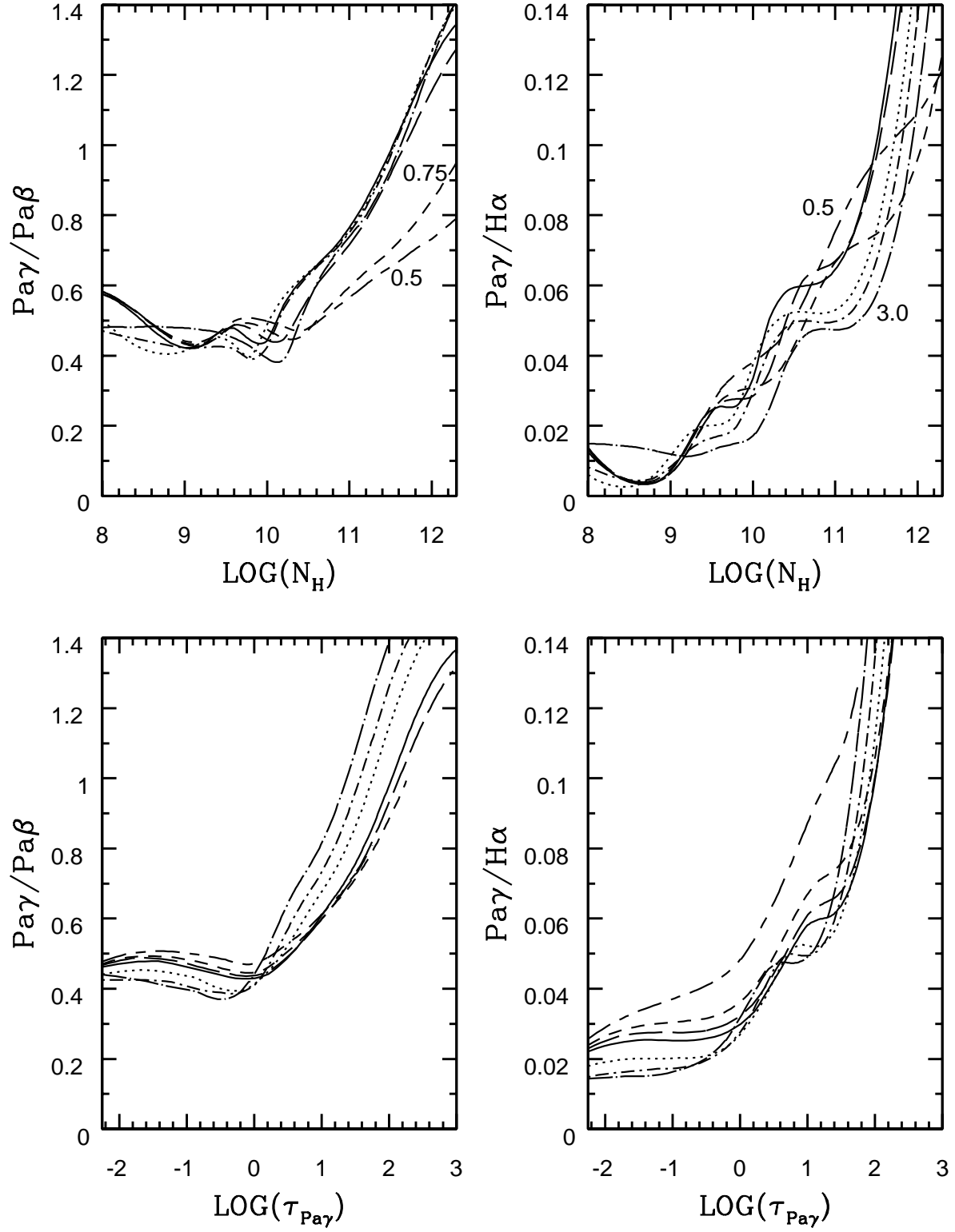
Fig. 11.— Dependences of $Pa\gamma/Pa\beta$ and $Pa\gamma/H\alpha$ on density and line optical depth for $r = 4R_*$, $\gamma_{HI} = 2 \times 10^{-4}\ s^{-1}$, and various temperatures(cf. Table 1).
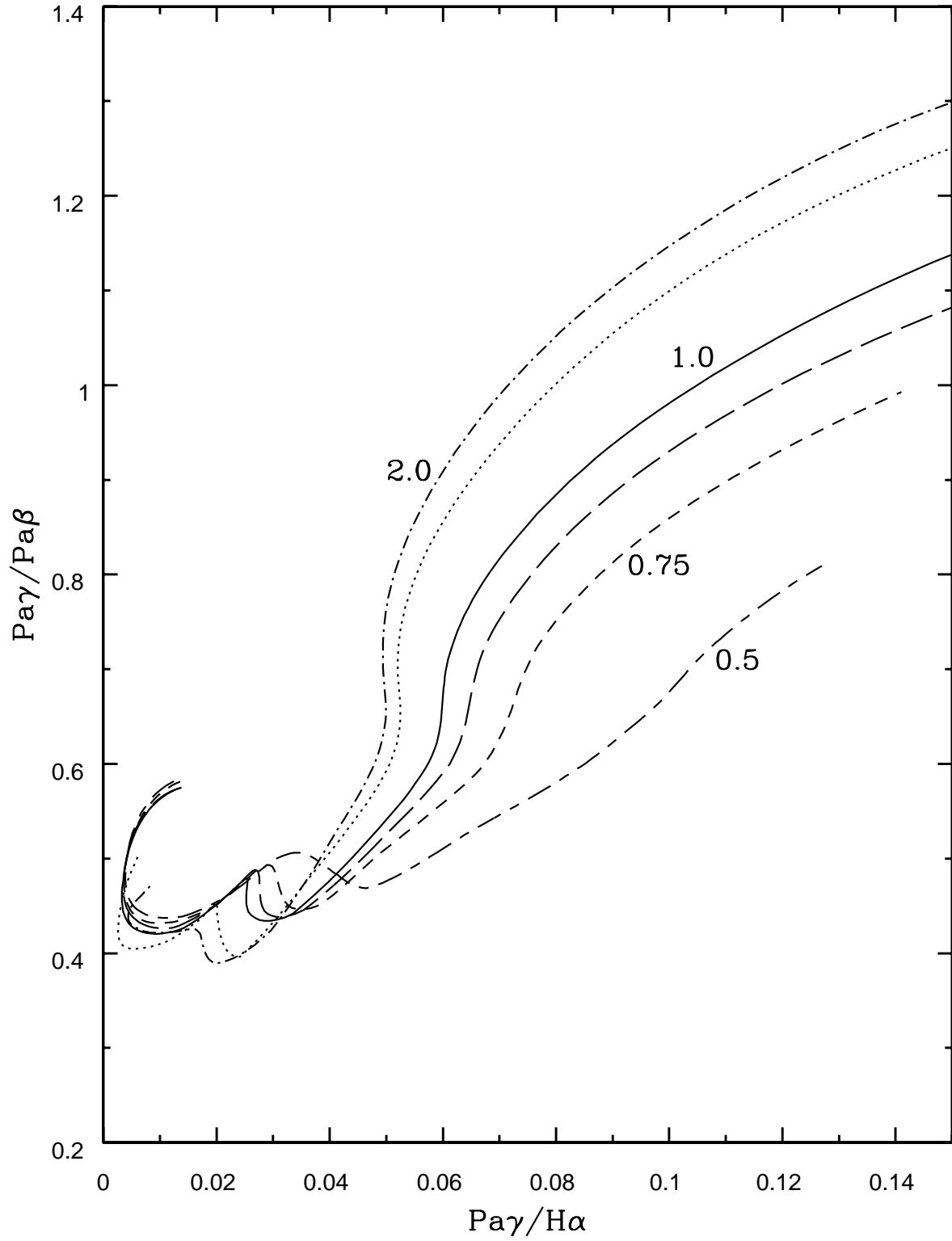
Fig. 12.— Plot of $Pa\gamma/Pa\beta$ versus $Pa\gamma/H\alpha$ for $r = 4R_*$, $\gamma_{HI} = 2 \times 10^{-4} \ s^{-1}$, and various temperatures(cf. Table 1).
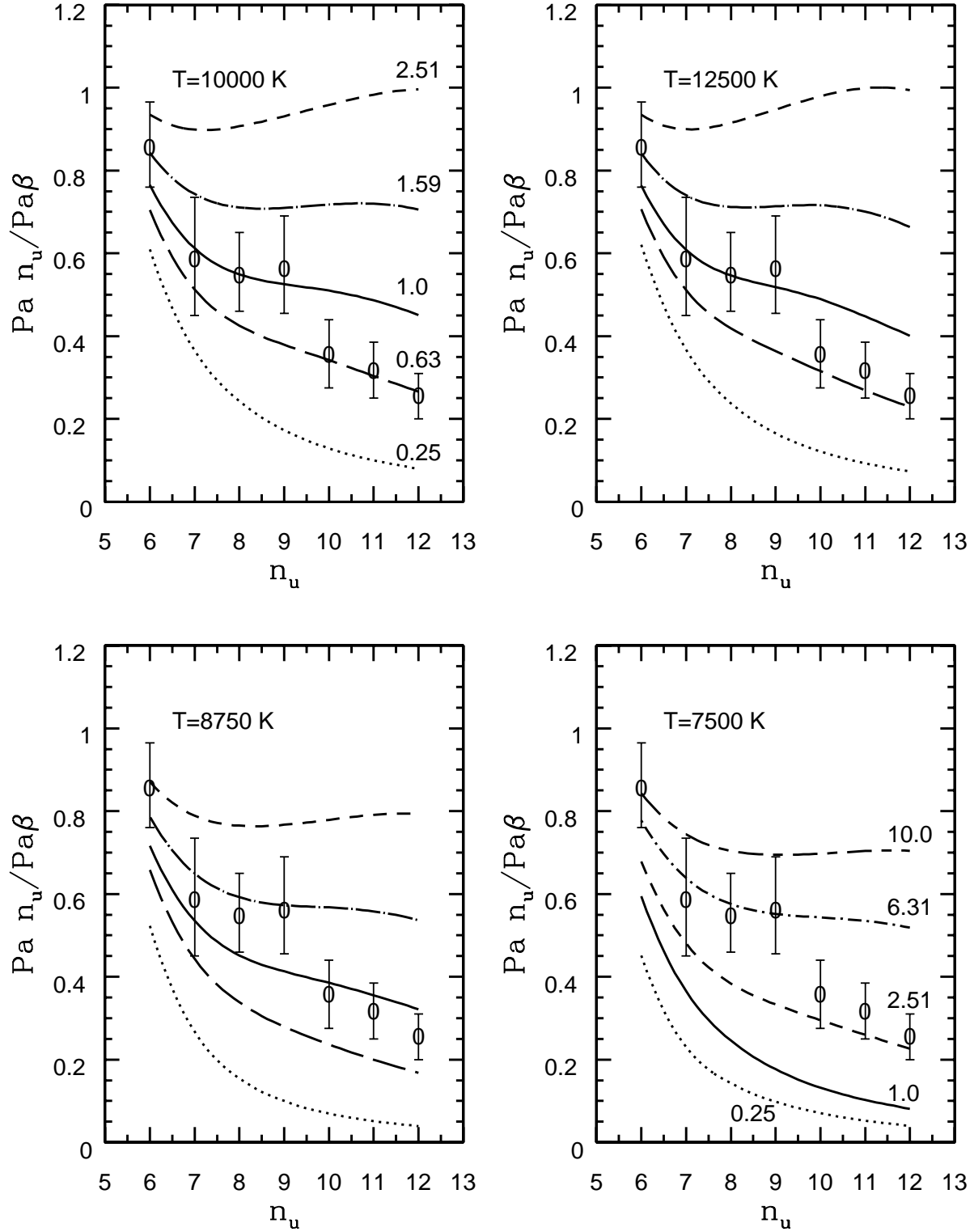
Fig. 13.— Plot of $Pa\,n_u/Pa\beta$ versus n_u for four temperatures, $r = 4R_*$, $\gamma_{HI} = 2 \times 10^{-4}\ s^{-1}$, and various values of N_H (in unit of $10^{11}\ cm^{-3}$). Data marked by open circles are from Bary et al. (2008).
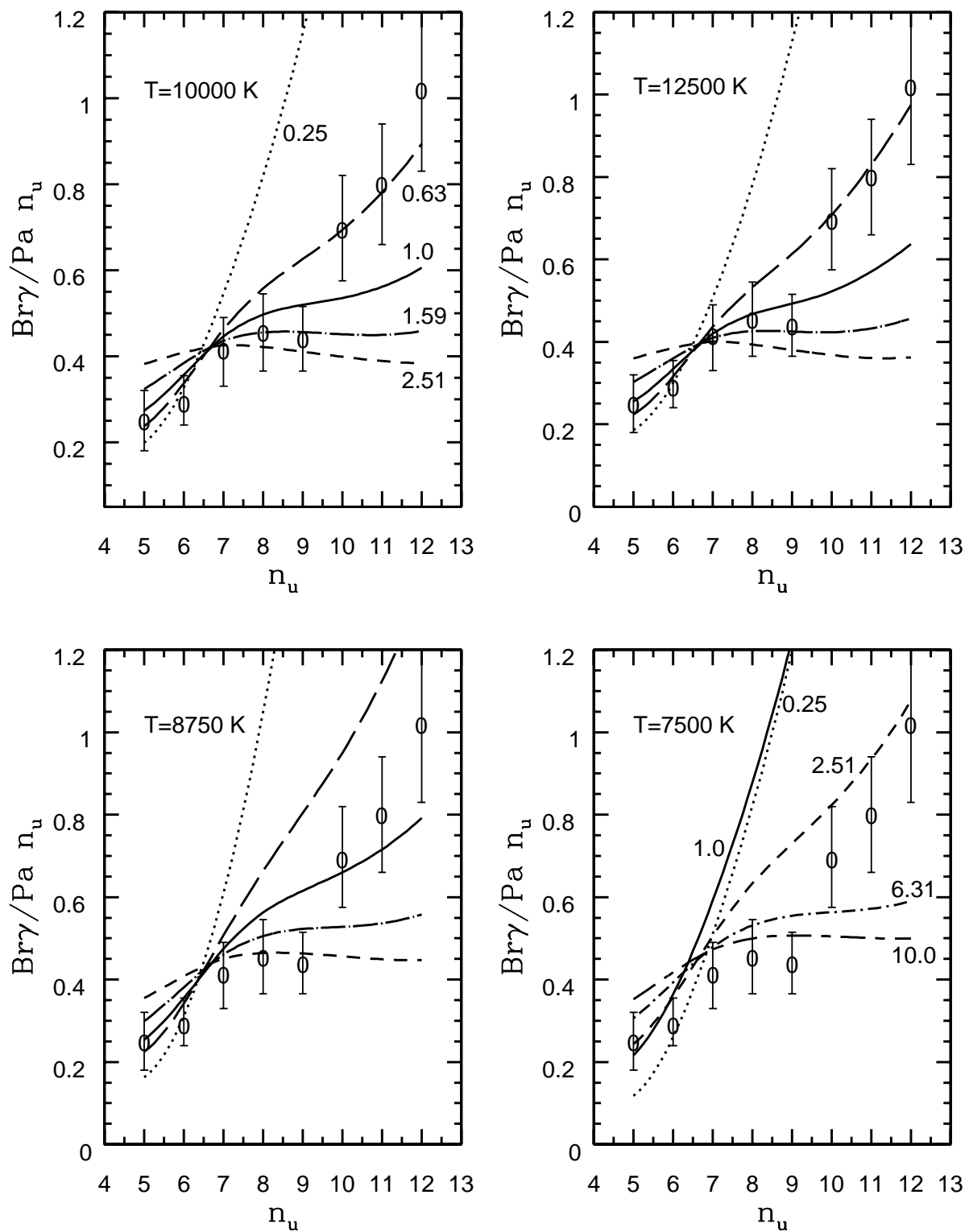
Fig. 14.— Same as Fig. 13 but for $Br\gamma/Pa\ n_u$.
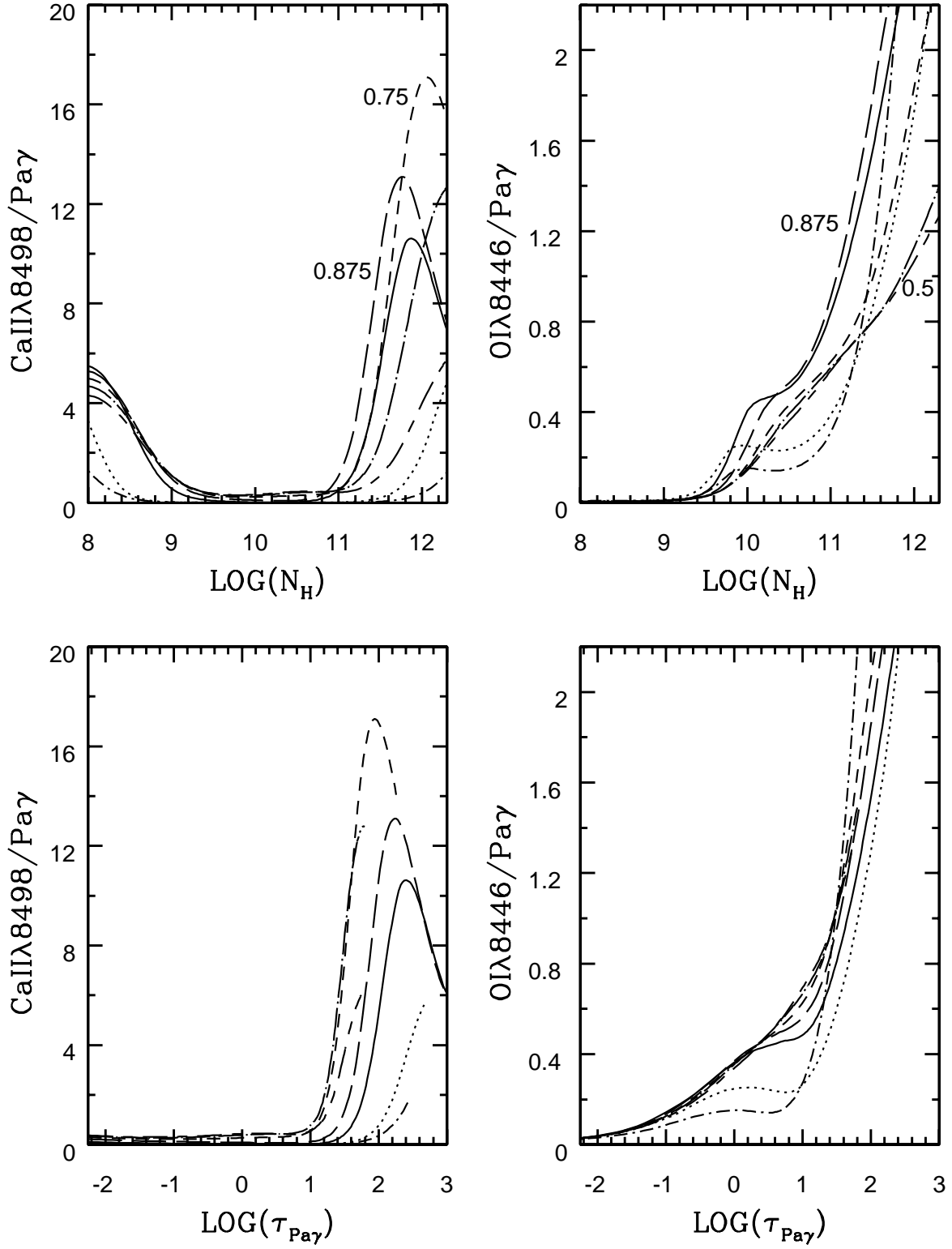
Fig. 15.— Dependences of $CaII\lambda8498/Pa\gamma$ and $OI\lambda8446/Pa\gamma$ on density and line optical depth for $r = 4R_*$, $\gamma_{HI} = 2 \times 10^{-4}$ s^{-1}, and various temperatures(cf. Table 1). The large $CaII\lambda8498/Pa\gamma$ values at $N_H < 10^9$ cm^{-3} are not significant because they occur at $\tau_{Pa\gamma} \ll 1$.
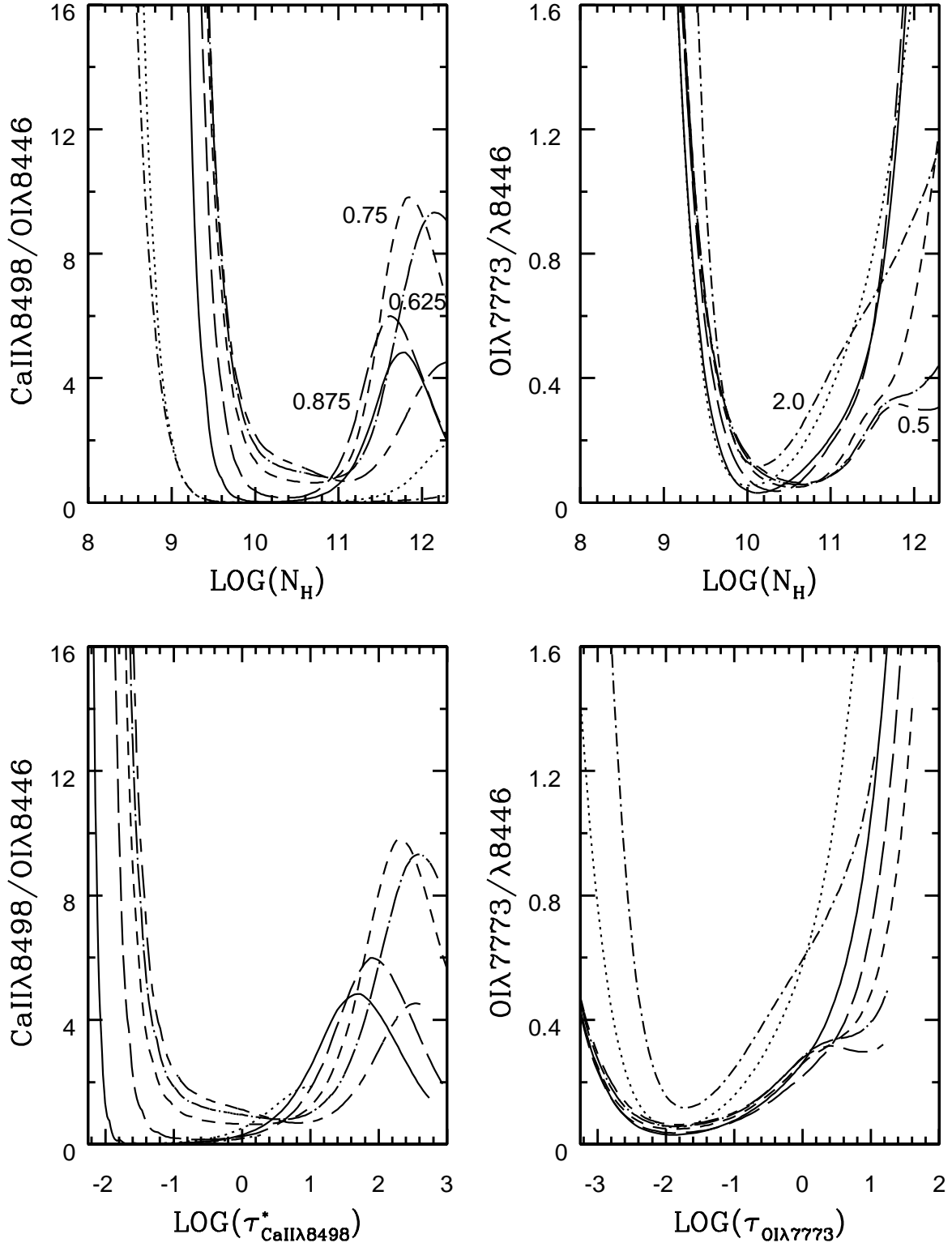
Fig. 16.— Dependences of $CaII\lambda8498/OI\lambda8446$ and $OI\lambda7773/\lambda8446$ on density and line optical depth for $r = 4R_*$, $\gamma_{HI} = 2 \times 10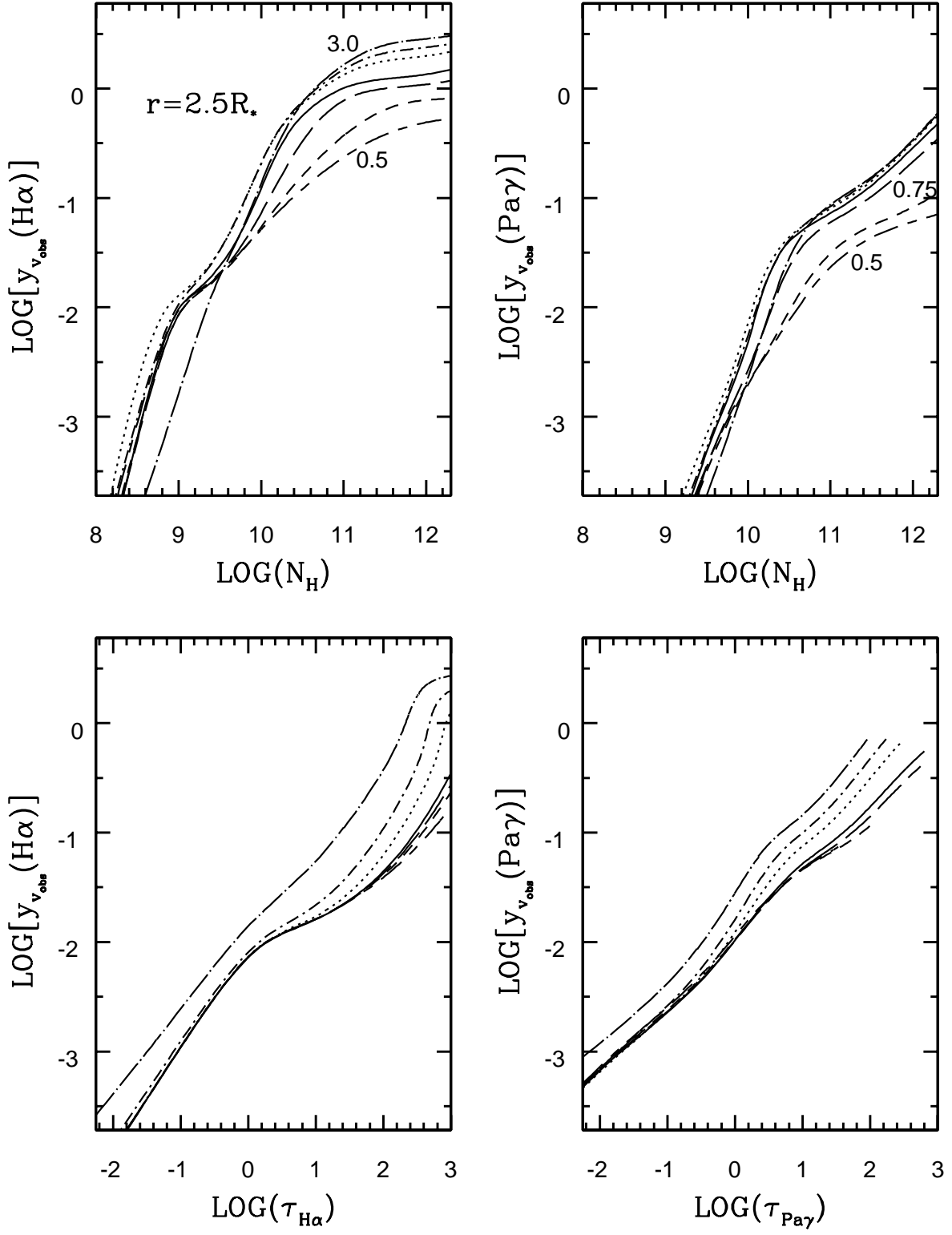^{-4}\ s^{-1}$, and various temperatures(cf. Table 1). The large $CaII\lambda8498/OI\lambda8446$ values at $N_H < 10^{10}\ cm^{-3}$ are not significant because they occur at $\tau^*_{CaII\lambda8498} \ll 1$.
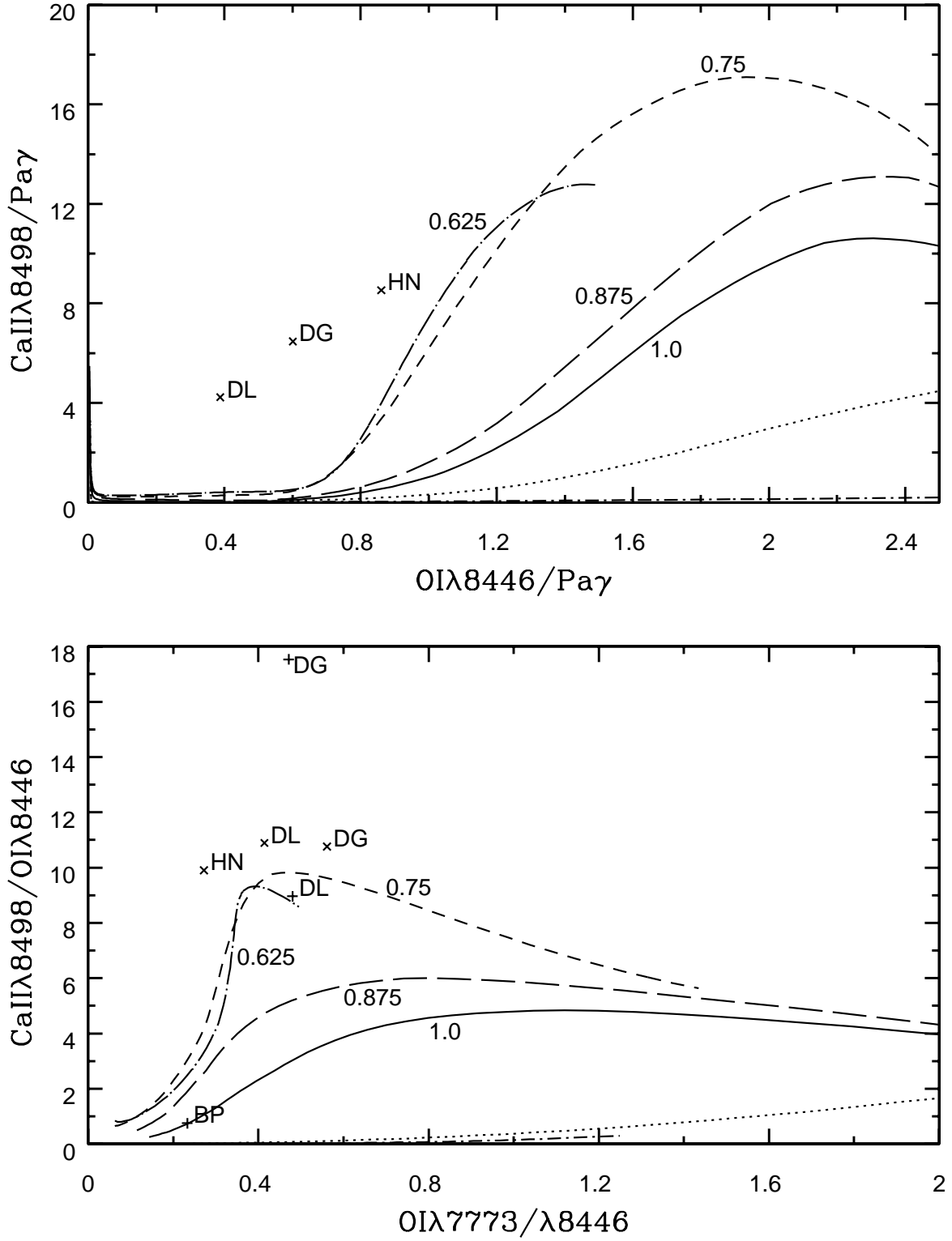
Fig. 17.— Plot of $CaII\lambda8498/Pa\gamma$ versus $OI\lambda8446/Pa\gamma$ (top panel) and $CaII\lambda8498/OI\lambda8446$ versus $OI\lambda7773/\lambda8446$ (bottom panel) for $r = 4R_*$, $\gamma_{HI} = 2\times10^{-4}\ s^{-1}$, and various temperatures(cf. Table 1). Data points marked by xs and +s are from Edwards et al. (2010) and Muzerolle et al. (1998) respectively.
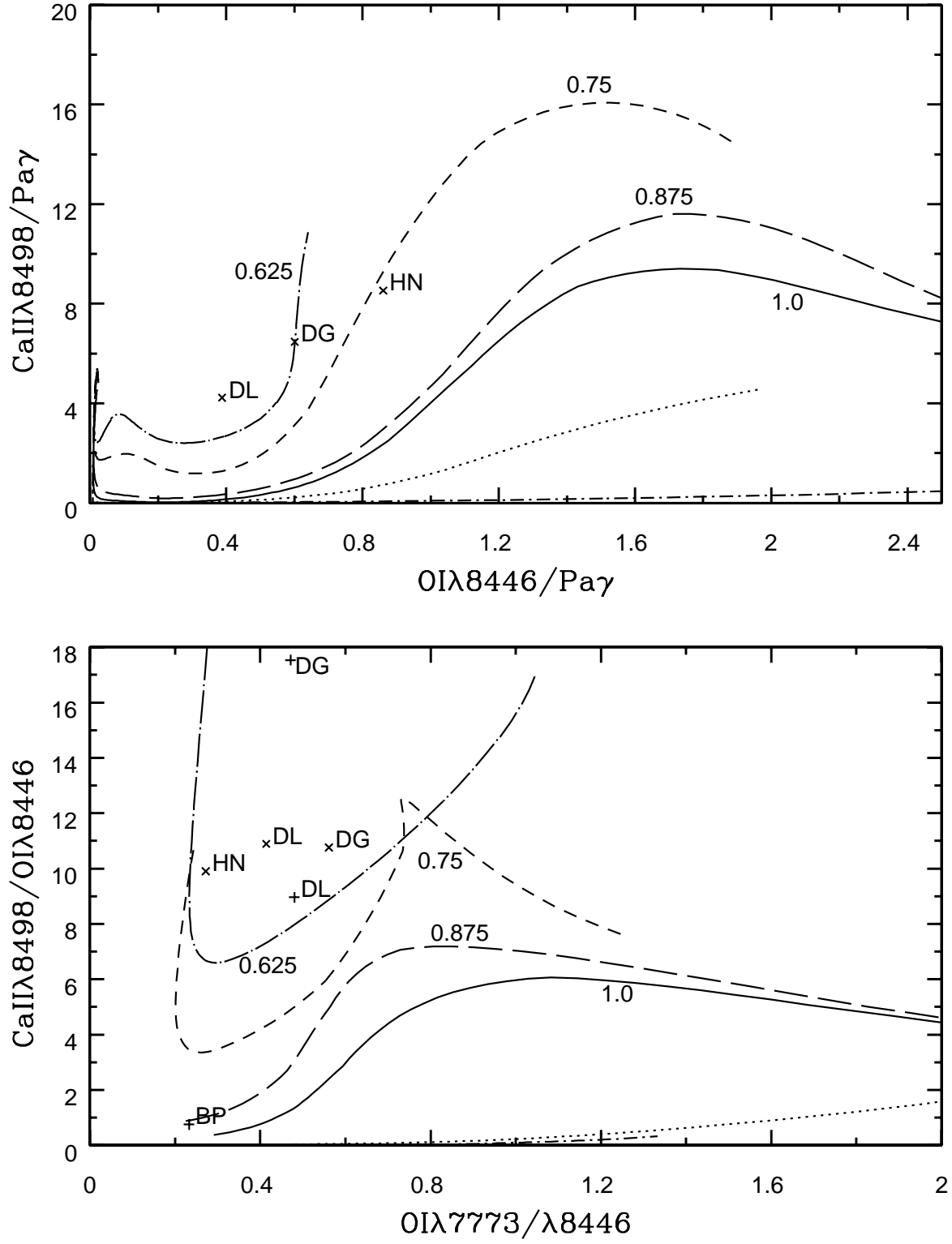
Fig. 18.— Same as Fig. 17 but for $r = 2.5R_*$, $\gamma_{HI} = 2 \times 10^{-5}\ s^{-1}$.
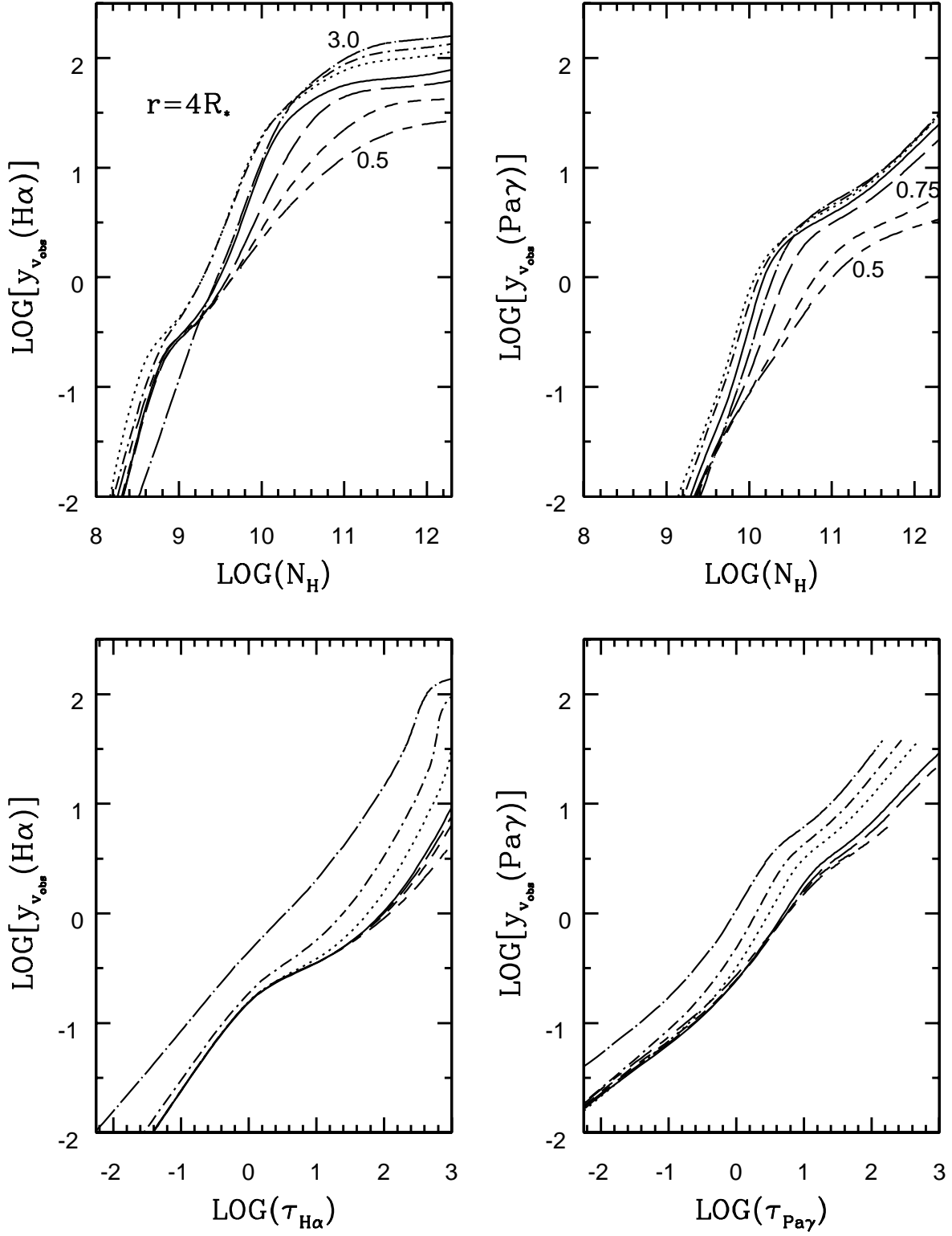
Fig. 19.— Dependences of $H\alpha$ and $Pa\gamma$ specific flux (measured relative to the local continuum), $y_{v_{obs}}$, on density and line optical depth for $\gamma_{HI} = 2 \times 10^{-4}\ s^{-1}$ and various temperatures (cf. Table 1) in the wind model.
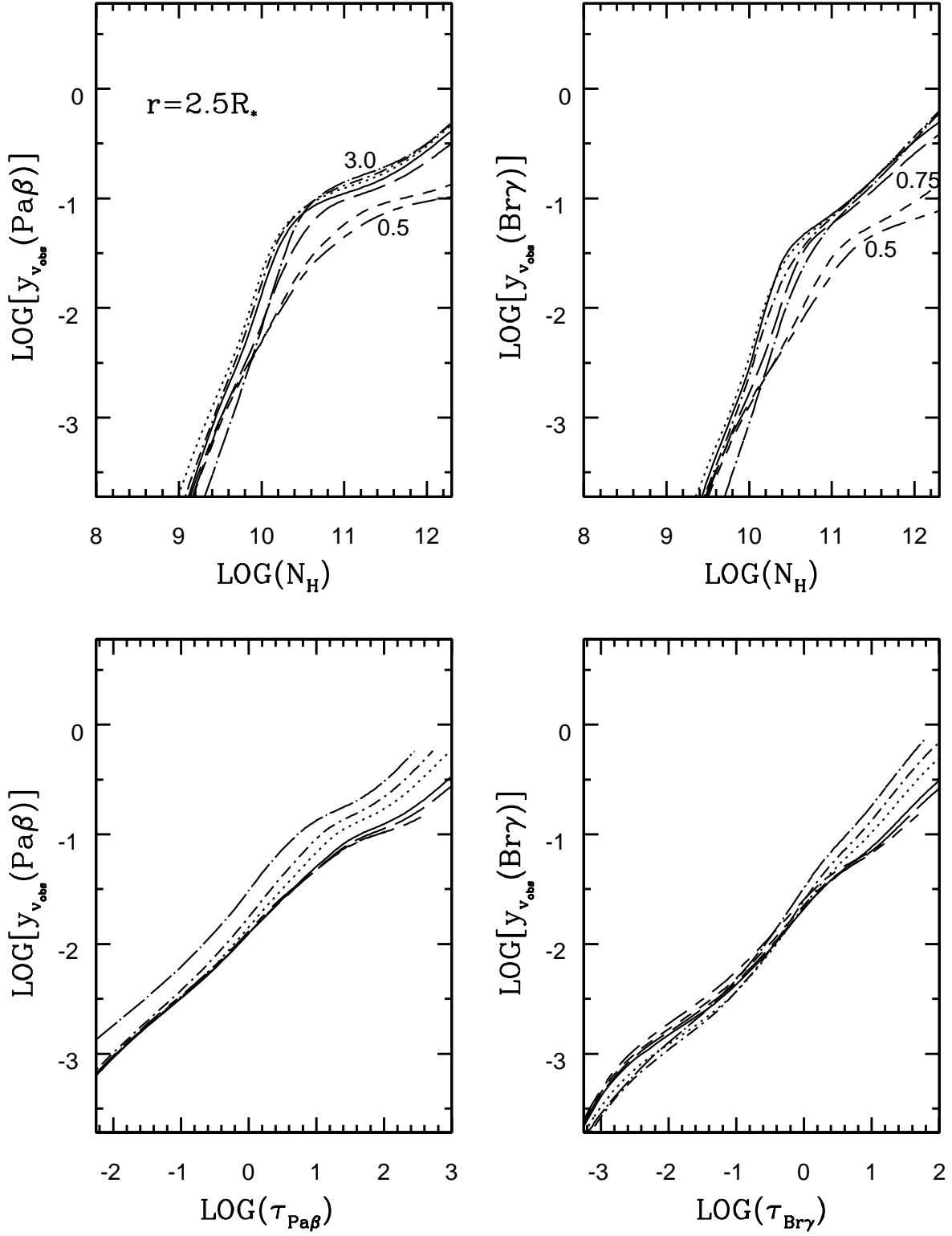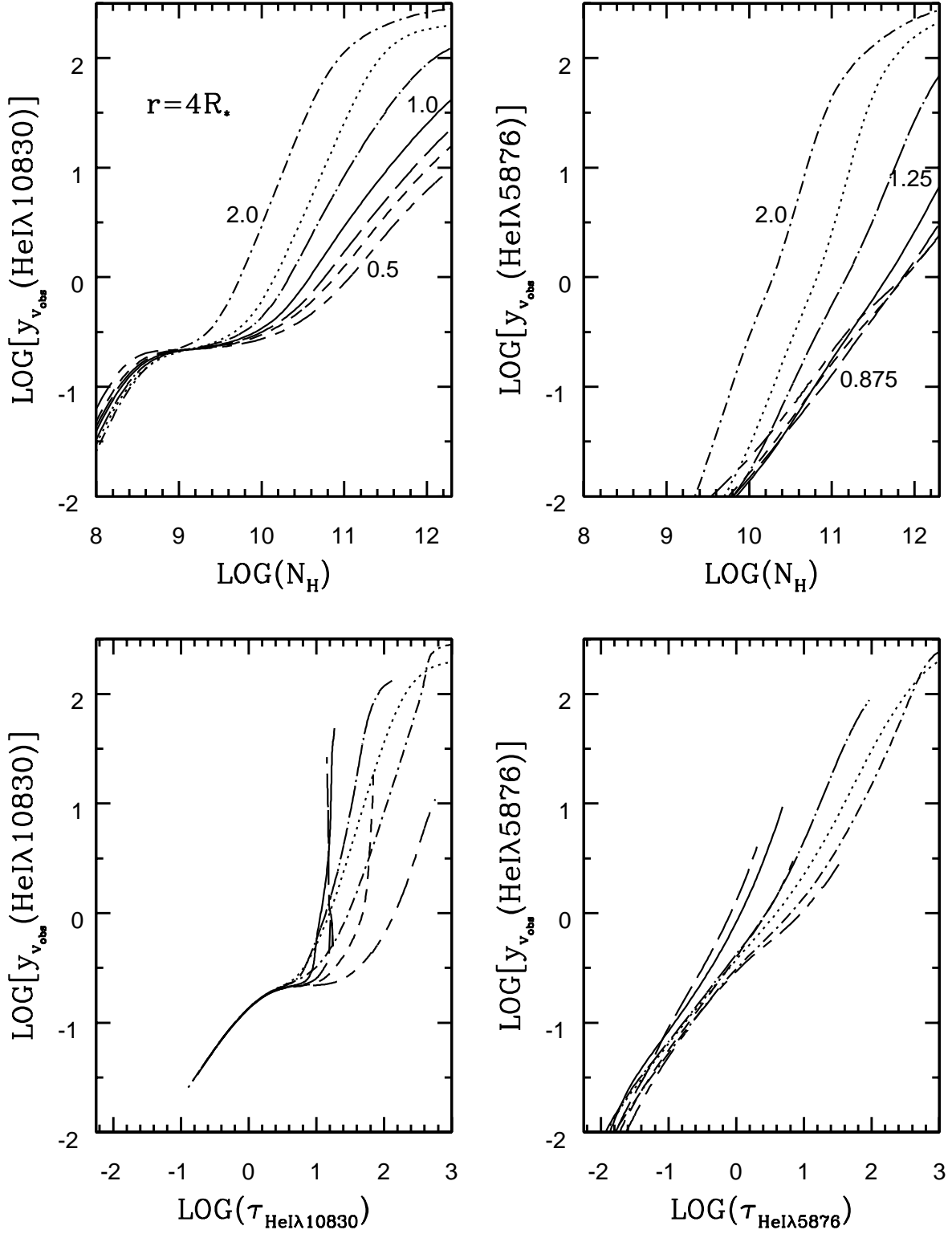
Fig. 20.— Same as Fig. 19 but for the infall model.

Fig. 21.— Dependences of $Pa\beta$ and $Br\gamma$ specific flux (measured relative to the local continuum), $y_{v_{obs}}$, on density and line optical depth for $\gamma_{HI} = 2 \times 10^{-4}\ s^{-1}$ and various temperatures (cf. Table 1) in the infall model.

Fig. 22.— Dependences of $HeI\lambda10830$ and $HeI\lambda5876$ specific flux (measured relative to the local continuum), $y_{v_{obs}}$, on density and line optical depth for $\gamma_{HeI} = 10^{-4}\ s^{-1}$ and various temperatures (cf. Table 1) in the wind model.
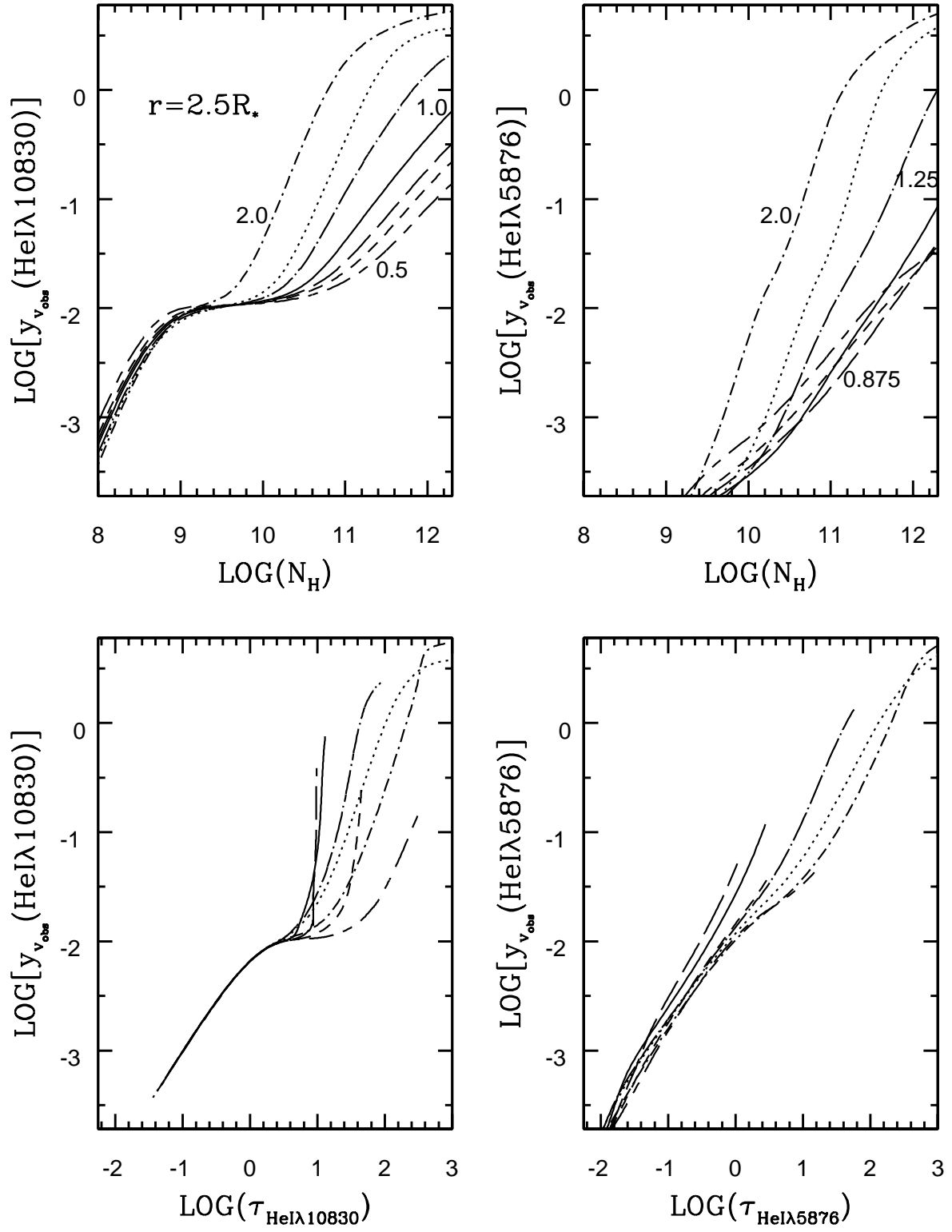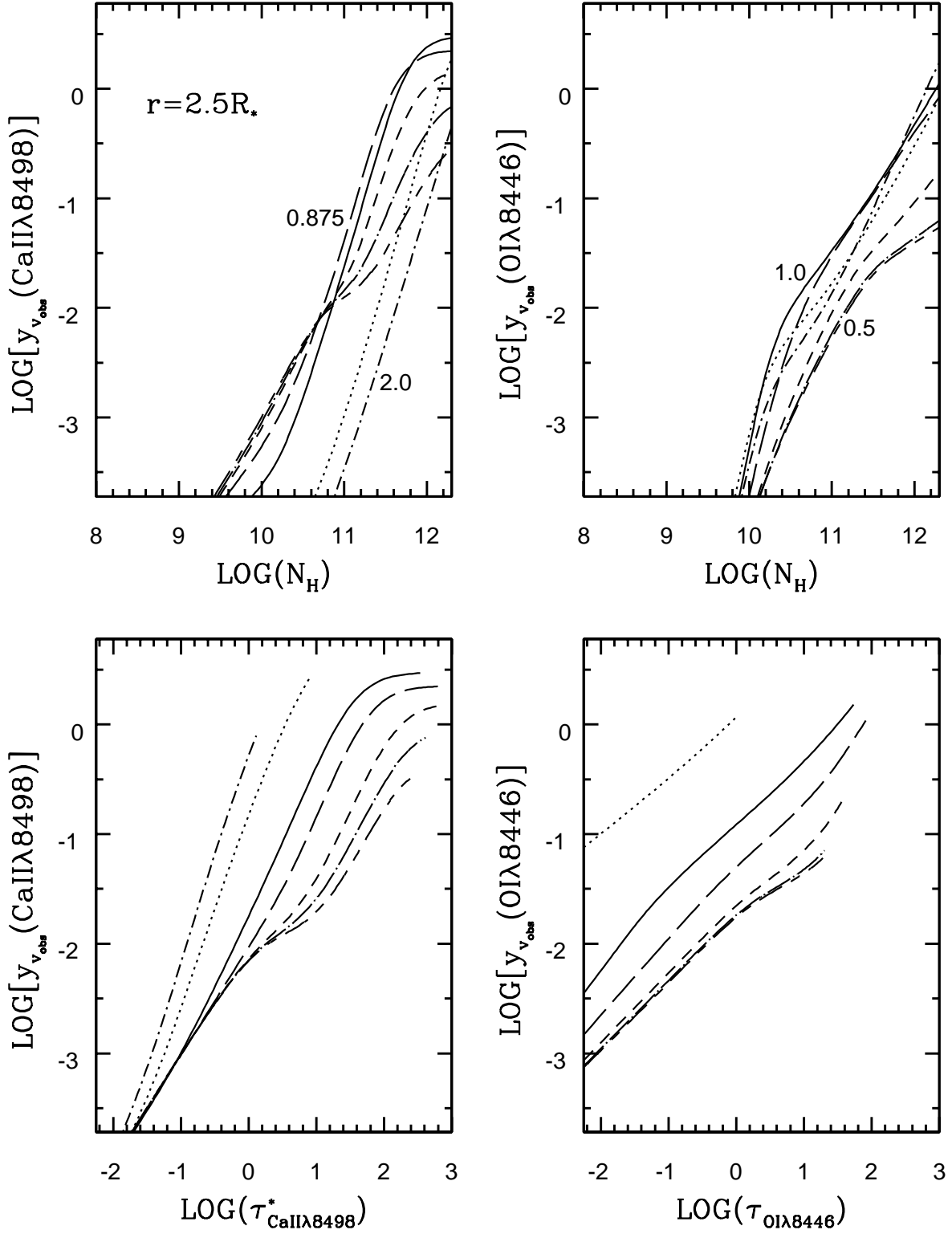
Fig. 23.— Same as Fig. 22 but for the infall model.

Fig. 24.— Dependences of $CaII\lambda8498$ and $OI\lambda8446$ specific flux (measured relative to the local continuum), $y_{v_{obs}}$, on density and line optical depth for $\gamma_{HI} = 2 \times 10^{-4}\ s^{-1}$ and various temperatures (cf. Table 1) in the infall model.